A Poroelastic Model of Transcapillary Flow

by

Sean Speziale

A thesis
presented to the University of Waterloo
in fulfillment of the
thesis requirement for the degree of
Doctor of Philosophy
in
Applied Mathematics

Waterloo, Ontario, Canada, 2010

I hereby declare that I am the sole author of this thesis. This is a true copy of the thesis, including any required final revisions, as accepted by my examiners.

I understand that my thesis may be made electronically available to the public.

Abstract

Transcapillary exchange is the movement of fluid and molecules through the porous capillary wall, and is important in maintaining homeostasis of bodily tissues. The classical view of this process is that of Starling's hypothesis, in which the forces driving filtration or absorption are the hydrostatic and osmotic pressure differences across the capillary wall. However, experimental evidence has emerged suggesting the importance of the capillary wall ultrastructure, and thus rather than the global differences between capillary and tissue, it is the local difference across a structure lining the capillary wall known as the endothelial glycocalyx that determines filtration. Hu and Weinbaum presented a detailed cellular level microstructural model of this phenomenon which was able to explain some experimental discrepancies.

In this Thesis, rather than describing the microstructural details, the capillary wall is treated as a poroelastic material. The assumptions of poroelasticity theory are such that the detailed pore structure is smeared out and replaced by an idealized homogeneous system in which the fluid and solid phases coexist at each point. The advantage of this approach is that the mathematical problem is greatly simplified such that analytical solutions of the governing equations may be obtained. This approach also allows calculation of the stress and strain distribution in the tissue. We depart from classical poroelasticity, however, due to the fact that since there are concentration gradients within the capillary wall, the filtration is driven by both hydrostatic and osmotic pressure gradients. The model predictions for the filtration flux as a function of capillary pressure compares favourably with both experimental observations and the predictions of the microstructural models.

An important factor implicated in transcapillary exchange is the endothelial glycocalyx, which was shown experimentally to protect against edema formation. Using our theory in combination with the experimental measurements of glycocalyx thickness and pericapillary space dimension (PSD), we make a quantitative comparison for the excess flow as a result of a deteriorated glycocalyx, which shows reasonably good agreement with the data. Since many of the parameters in the model are difficult to measure, a sensitivity analysis was performed on the most important of these. Finally, since there was variation in the measurements of glycocalyx thickness and PSD, we used probability distributions to represent the data, and performed further calculations to obtain ranges of likely values for the various parameters. This work could find applications in cardiovascular disease, where

the glycocalyx is degraded or absent, and in cancer research, where the abnormal vasculature is an impediment to the efficient delivery of anti-cancer drugs.

Acknowledgements

I would like to express my sincere gratitude to Prof. Giuseppe 'Pino' Tenti, first and foremost for instilling in me a passion for scientific research. His willingness to answer any question, his enthusiasm for teaching those around him, and his consistent encouragement fostered an environment which allowed me to grow into an independent researcher. Neither of my publications, nor this thesis, would have been possible without him. Any skills I have obtained in regards to reading, writing, and presenting scientific ideas, I owe to him.

I am deeply indebted to Prof. Siv Sivaloganathan, for his support and for being forthcoming with advice on any matter, and for somehow always doing this in good spirits. Despite his immense workload, whenever I went to Siv with a problem, he always made time and our discussions always had a calming effect on me. He is a superb editor, and has taught me how to become a better writer. His dedication to our research group, his committment to the idea that mathematics can be used to solve medical problems, and his ability to bring people together for multidisciplinary research are exceptional qualities which have helped shape my experience as a graduate student.

I would like to thank Prof. Matthew Scott, firstly for showing me what I should aspire to be as a graduate student, and secondly for serving on my Ph.D. Committee. His always impeccably delivered presentations had an enormous influence on me as a young graduate student, and his willingness to discuss matters related to his or my research was always appreciated. His many thoughtful suggestions for my thesis considerably strengthened this work, and for that I thank him.

I thank Prof. Sean McKee and Prof. Frederick McCourt for serving on my committee, asking thought-provoking questions, and making helpful comments about the content of this thesis.

I extend thanks to the current and former members of the Biomedical Research Group, especially colleagues Kathleen Wilkie, Rudy Gunawan, Gibin Powathil, Colin Phipps, and Colin Turner, as well as Prof. Mohammad Kohandel. These people have helped me get to where I am today, from aiding me with technical or computing issues to having philosophical discussions about matters academic and non-academic alike. I also thank the faculty and fellow graduate students in the Department of Applied Mathematics for making my experience rewarding, both intellectually and socially. A special thanks to Helen Warren, whose help made so

many things so much easier. It must take a great deal of patience and care to do what Helen does – every time I knocked on her door, she made me feel like I was her first priority.

I would like to thank NSERC, OGS, and the University of Waterloo for financial support.

My heartfelt gratitude to my mother and father for teaching me that education is most important, for their unwavering support and for their continued belief in me. Thanks to Lauren and Jenna for being there always, with enthusiasm and love. And thanks to my many wonderful friends, most of whom have only the slightest idea of the contents of this thesis, for keeping me grounded and making me laugh.

Finally, Kristene – who has stood by me in the best of times, but more importantly in the worst of times, who has patiently listened to my dreams and fears, encouraging and reassuring me during the many peaks and valleys that occur over the course of a Ph.D., and who now, upon becoming a parent, has made me admire her more than I thought possible – thank you. And Chloe — for the perspective you have given me, and for what I feel when I see your beautiful smile – thank you.

For Kristene and Chloe

Contents

List of Tables

List of Figures

Chapter 1

Introduction

In 1896, the physiologist E.H. Starling showed that fluid could be absorbed by the blood vessels directly from the tissue spaces and subsequently hypothesized that the forces that determine filtration or absorption of fluid across the capillary wall are the hydrostatic and osmotic pressure differences between the capillary and tissue (interstitial) space. The experimental studies of Landis (1927) as well as Pappenheimer and Soto-Rivera (1948) confirmed Starling's hypothesis by measuring the filtration flux as a function of capillary pressure, finding a linear relation with filtration of fluid from the capillaries at high capillary pressures and reabsorption of fluid into the capillaries at low capillary pressures. Additionally, the capillary pressure at which there was zero filtration was equal to the effective osmotic pressure difference between plasma and tissue. Starling's hypothesis thus became the paradigm in describing the mechanism of transcapillary exchange.

Eventually, mathematical theories were developed in an attempt to describe the process quantitatively, with the most successful of these envisioning the capillary wall as a semipermeable membrane. An equation for the filtration flux in terms of the hydrostatic and osmotic pressures in the capillary and interstitial space may be derived from this theory, and this became known as the Starling equation. However, more sophisticated experimental techniques identified the detailed cellular level ultrastructure of the capillary wall, and it became clear that the process was more complicated than simply flow across a membrane. In addition, the experimental study of Michel and Phillips (1987) challenged the classical view of Starling's hypothesis, as the relation for filtration flux as a function of capillary pressure, postulated to be linear in the Starling equation, was found to be nonlinear in the

steady-state. Moreover, the nonlinearity occurred in the region of low capillary pressures, in which reabsorption would be expected, such that for no values of capillary pressure would the filtration flux be negative. The implication was that there could be no reabsorption of fluid in the steady-state.

Investigation of the mechanism of this nonlinear behaviour gave rise to the ultrastructural models of transcapillary exchange, which attempted to describe the process at the cellular level. But not until the work of Michel (1997) and Weinbaum (1998) were the reasons for the nonlinearity elucidated. The Michel-Weinbaum hypothesis suggests that the endothelial glycocalyx, a mesh-like structure lining the inside of the capillary wall, was the molecular sieve to plasma proteins. Therefore, rather than applying the Starling equation between the capillary and interstitial space, it should be applied only across the endothelial glycocalyx. The result of this was that the local protein concentration just behind the glycocalyx could be much less than that in the tissue, and in this case the force for filtration would be reduced such that in the steady-state there could be no reabsorption. The mathematical details of this hypothesis were given in Hu and Weinbaum (1999), who developed a detailed three-dimensional ultrastructural model.

The thorough study of Adamson et al. (2004) confirmed the Michel-Weinbaum hypothesis in mammalian microvessels, and a theory with a few modifications from that of Hu and Weinbaum (1999) was used to supplement their experimental results. Following this, Zhang et al. (2006a) pointed out some drawbacks of the model of Hu and Weinbaum (1999), one being that it was too complicated for convenient use by other investigators, and thus formulated a simplified one-dimensional model of transcapillary exchange. This model permitted an analytical solution and was consistent with the predictions of the three-dimensional model.

Each of the three models of Hu and Weinbaum (1999), Adamson et al. (2004), and Zhang et al. (2006a) makes different assumptions regarding the transport of fluid and plasma proteins. All of the models take the viewpoint proposed by the Michel-Weinbaum hypothesis for flow across the glycocalyx, but the treatment of the endothelial cleft region (on which we will elaborate in Chapter 2) differs quite drastically. However, the theoretical predictions are similar in each model. Both Hu and Weinbaum (1999) and Adamson et al. (2004) require numerical methods to solve their respective problems, whereas Zhang et al. (2006a) obtain a large number of algebraic equations that can be solved with the use of a computer. Our motivating purpose for the model presented in this Thesis, published first in Speziale et al. (2008), is not all that different from Zhang et al. (2006a) in that it seeks to

simplify mathematically the phenomenon of transcapillary exchange while retaining the important predictive value of the above models. In order to accomplish this, we model the capillary wall as a poroelastic material, subject to the assumption that the porous medium is homogeneous and isotropic, and thus that the complex ultrastructural arrangement is replaced by an idealized fluid-solid mixture in which both phases coexist at each point. The use of poroelasticity theory permits an analytical solution of the governing equations, and we can express all quantities in closed form. We deviate from classical poroelasticity, however, in that the presence of gradients in concentration of plasma proteins induces an osmotic flow and thus the filtration velocity depends on both hydrostatic and osmotic pressure gradients, in contrast to the usual assumption of Darcy's law for fluid flow through a porous medium (which assumes proportionality of the filtration velocity and hydrostatic gradient only).

Since the endothelial glycocalyx clearly has an important role in transcapillary exchange, and because it was shown experimentally by van den Berg et al. (2003) to protect against edema formation, this Thesis also considers a deeper investigation into the glycocalyx effect on transcapillary flow, and a summary of the results has already appeared in the literature (Speziale and Sivaloganathan, 2009). We use expressions from our theory to calculate the magnitude of the increase in flow resulting from enzymatic deterioration of the glycocalyx, and we show how this can be related to the measurements of van den Berg et al. (2003). We then detail the effects of important parameters such as the glycocalyx permeability by carrying out a sensitivity analysis. Lastly, due to the large variation in the measurements of van den Berg et al. (2003), we use probability distributions to represent the data, and perform our calculations again to observe the effects. The organization of this Thesis is as follows.

In Chapter 2, we review the literature on the subject of transcapillary exchange. We begin with some background information on the cardiovascular system, discussing first the circulation in general, then the properties of the microcirculation. Included here is an explanation of the role of the capillary wall, the interstitial space, and the lymphatic system in tissue homeostasis. We then discuss Starling's experiments, and the origin of his hypothesis. The work of Landis (1927) and Pappenheimer and Soto-Rivera (1948) put Starling's hypothesis on solid experimental footing, and these experiments as well as their implications are described in detail.

Following this, we turn to the theoretical developments in the literature. Osmotic pressure is discussed, followed by a review of the concept of phenomenological

laws. We show how these ideas were used to formulate a theory of membrane transport from nonequilibrium thermodynamics, and when an analogy is made with the capillary wall acting as the semipermeable membrane, this gives rise to the Starling equation. Application of this theory to steady-state ultrafiltration gives the experimentally observed prediction that there can be no reabsorption in the steady state. We then explain the ideas behind Pore Theory and the Fiber Matrix Model, which attempt to describe the microscopic properties of the membrane.

The transient nature of transcapillary exchange is described in Section 2.5. The experiments of Michel and Phillips (1987), which showed no steady-state reabsorption, are described along with their implications. Following this, we explain how the terms in the Starling equation are actually time-dependent thus leading to the need for a new paradigm. We then elaborate on the formulation of the hypothesis of Michel (1997) and Weinbaum (1998) from which a new view of Starling's hypothesis emerges.

The mathematical model of Hu and Weinbaum (1999) is described in a comprehensive fashion, including a discussion of the assumptions underlying the governing equations as well as the boundary conditions. We outline the theoretical predictions of this model, and discuss how these relate to experimental observations. Experimental evidence confirming the Michel-Weinbaum hypothesis is then reported, including an in-depth discussion of the important study of Adamson et al. (2004), in which experimental confirmation of the new view was established in mammalian microvessels. We consider the assumptions of their mathematical model and the implications of their experiments. The one-dimensional simplified mathematical model of Zhang et al. (2006a) is then described in relation to both the earlier theories and experiments. We conclude the chapter with a detailed discussion of the key assumptions in each of the mathematical models of Hu and Weinbaum (1999), Adamson et al. (2004), and Zhang et al. (2006a) which motivates the need for a simpler theory – namely our poroelastic theory of transcapillary flow.

The idea of flow through porous media, the assumptions underlying the theory of poroelasticity, the applicability to biomechanical problems, and our deviation from the classical theory, are discussed in the Introduction to Chapter 3. We then develop the mathematical model, explaining how osmotic pressure enters into our poroelastic model, and derive a differential equation for the osmotic pressure field. In our simplified geometry, the transport and stress/strain problems are decoupled, and full details of the solutions are given in Sections 3.2.2 and 3.2.3. Our results are then presented, first with a discussion of the parameters, followed

by the predictions for transport, stress and strain. In the Discussion, we re-visit the major assumptions of our theory along with those of the microstructural models. An expression is derived from our theory for a parameter known as the hydraulic conductivity, which allows comparison with the microstructural models as well as with experimental observations. We also discuss the stress and strain, and given that these have not been measured, we postulate values based on a parametric study.

Chapter 4 begins with a general discussion of the properties of the endothelial glycocalyx and its many functions. The experiments of van den Berg et al. (2003) are then described and used as motivation for our work. We first estimate the change in fluid content in the pericapillary space due to enzymatic degradation of the glycocalyx. The role of the glycocalyx in our model is then recalled, and an important dimensionless parameter that characterises the relative resistance to transcapillary flow due to the glycocalyx is emphasized. We then postulate a relation between the amount of fluid in the pericapillary space and the excess flow due to a deteriorated glycocalyx, which is used to make a quantitative comparison with the experiments of van den Berg et al. (2003). An expression for the glycocalyx thickness given the relative change in the amount of pericapillary fluid is derived, followed by a discussion of this in relation to the resistance due to the glycocalyx. We then allow the permeability of both the glycocalyx and capillary wall to change upon enzymatic treatment, and discuss the predictions of our model in this case. Finally, results are shown in which the reflection coefficient of the glycocalyx changes with enzymatic treatment. A comparison is then made between our theoretical predictions and those of other models, as well as experimental data.

Section 4.3 begins with a procedure designed to find an optimal probability distribution to represent the histograms for pericapillary space dimension from van den Berg et al. (2003). We then perform our calculations again for the change in fluid content and predicted glycocalyx thickness given the relative change in fluid content, and derive probability distributions for both of these. Finally, we attempt to quantify the variability in our predictions for glycocalyx thickness.

In the last chapter, we assess the contribution of this work (by comparison to other models) and its place in the literature concerning transcapillary exchange. We also touch on some possible extensions to this model, before closing with a discussion of applications.

The appendix gives the general properties of the chi-square distribution, followed

by a discussion of our methods of calculating the optimal distributions to match the data.

Chapter 2

Literature Review

2.1 Circulation and microcirculation

The cardiovascular system (CVS), which includes the heart, blood, and blood vessels, evolved to transport nutrients, oxygen, waste products, hormones and heat around the body. The primary function of the CVS is the rapid transport of oxygen, glucose, amino acids, fatty acids, vitamins, drugs and water to the tissues, and the rapid clearance from the tissues of metabolic waste products such as carbon dioxide, urea, and creatinine. Also, the CVS is crucial for the regulation of body temperature, as it transports heat from the deep tissues to the skin surface. (Levick, 2003)

The circulation can be broken into two components: the pulmonary circulation, which transports blood between the heart and lungs, and the systemic circulation, which transports blood to the rest of the body. The right side of the heart governs the pulmonary circulation, as blood fills the right atrium, then during relaxation (diastole) moves into the right ventricle, before being pumped into the lung by a contraction (systole). Upon moving through the lung, the blood returns, fully oxygenated, into the left atrium. A similar process takes place simultaneously in the left side of the heart, where it moves from the atrium to ventricle during diastole and is then pumped through the aorta at a much higher pressure during systole. (Levick, 2003)

There is a well-defined hierarchy of blood vessels, with blood from the heart first passing through the largest artery in the body, the aorta, which has a diameter of

about 2.5 cm. The aorta divides into a set of large arteries (1-2 cm), which branch to form medium to small arteries of diameter 0.1-1.0 cm. These further branch into terminal arteries (0.1-0.5 mm) and high resistance vessels called arterioles (10-100 μm). The arterioles finally branch into tiny capillaries, the smallest of the body's blood vessels at only 4-7 μm. On the venous side of the circulation, the capillaries converge to form postcapillary venules (10-30 μm) and venules (50-200 μm), which further converge to form larger veins (0.5 cm), which finally bring blood to the superior vena cava and inferior vena cava (3 cm), the largest of the veins. Note that the definitions of the small vessels lack precision, as the properties may be different in different tissues (Levick, 2003; Caro et al., 1978; Fung, 1997).

Blood flow through the vessels is driven by pressure gradients, with the flow proportional to the pressure difference along a vessel. Opposition to flow is called resistance, so that a vessel with larger resistance requires a larger pressure difference to drive the flow. Poiseuille's law for laminar flow implies that the resistance is inversely proportional to the fourth power of tube radius. In arteries, the flow is pulsatile due to the periodic contractions of the heart, meaning that during systole the pressure is higher than in diastole (e.g. a blood pressure of 'one twenty over eighty' refers to a pressure of 120 mmHg during systole and 80 mmHg during diastole). The large arteries have very distensible walls, which therefore enable them to smooth, or make more continuous, the pulsatile flow from the heart to the smaller arteries. The medium or small arteries deliver blood to the organs, and may dilate or contract, depending on the needs of the particular organ. The terminal arteries and arterioles are the location of the major pressure drop, and thus they must have a large resistance. This is why they are often referred to as resistance vessels. They in essence regulate blood flow by contraction and relaxation of smooth muscle cells that are part of the vessel wall (called vasodilation or vasoconstriction, respectively), and since resistance changes with the fourth power of radius, the resistance can change quite dramatically for even small changes in radius. Finally, in the capillaries, the pressure has dropped to about 20 mmHg with the velocity being only about 0.5% of that in major arteries. The venules and veins are larger than the corresponding arterioles and arteries, with pressures and thus velocities that are smaller. They also contain about 60-70% of the circulating blood so in this sense they act as a reservoir of blood which can be actively controlled through nerve impulses. (Levick, 2003; Caro et al., 1978; Fung, 1997)

The capillary networks of different tissues may be vastly different in architecture from one another. The capillary density (number per area) varies over a large

range, with values of 300-1000 capillaries per square millimeter in skeletal muscle, and up to as high as 3000 per square millimeter in the brain. The capillary density determines the surface area available for the exchange of nutrients. The intercapillary spacing determines the maximum distance from blood to tissue cell, which is important since molecules arrive at the cells primarily by diffusion. Shown in Figure 2.1 is a representative capillary network from Smaje et al. (1970), with several important parameters, such as the arteriolar and venular pressures, capillary length and density, and average distance between capillaries. All of these parameters determine how efficient the network is in doing its job – delivering nutrients and removing waste.

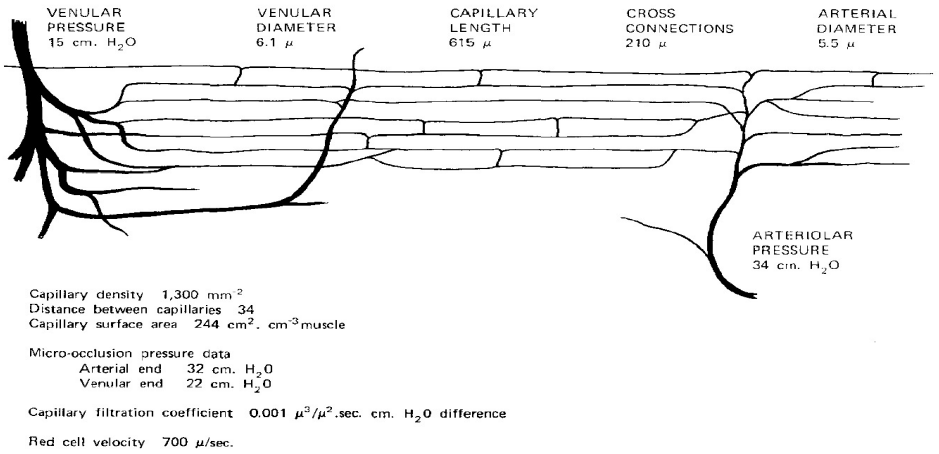

FIG. 5. Idealized diagram of the capillary bed in the cremaster muscle showing the type of arrangement of the vessels and mean values obtained in the experiments.

Figure 2.1: A representative capillary network with measured values of the parameters. Reprinted from Smaje et al. (1970) with permission from Elsevier.

There are three types of capillary in the body. They are known as continuous, fenestrated, or discontinuous. Continuous capillaries are found in muscle, skin, lung and the nervous system. The circumference is a continuous ring of between 1-3 endothelial cells with a continuous basement membrane. The capillary wall, or endothelium, will be discussed in more detail later. Fenestrated capillaries are about an order of magnitude more permeable than continuous capillaries. They are found in tissues specializing in fluid exchange, for example the kidneys. The endothelium has 50-60 nm 'windows', called fenestrae, which allow for rapid transfer of water and nutrients between the blood and tissue. Discontinuous capillaries contain large endothelial gaps, over 100 nm wide, and contain a discontinuity in the basement membrane, which makes them highly permeable to plasma proteins. This type of capillary is found where red and white blood cells are required to move between

plasma and tissue, such as in the liver and spleen (Levick, 2003).

The primary role of the endothelium is to form a semipermeable membrane that allows for exchange of nutrients between the blood and tissue. The endothelium 'senses' shear stress and secretes chemicals (e.g. nitric oxide) that adjust the local flow conditions (vasodilation/vasoconstriction). It also helps defend against pathogens by allowing the passage of white blood cells, and can initiate angiogenesis (the formation of new blood vessels). Endothelial dysfunction contributes to atherosclerosis, as cholesterol may form a plaque on the endothelium.

Endothelial cells (ECs) are polygonal and flattened, about 0.2-0.3 μm thick, 10-15 μm wide and 25-40 μm long (Simionescu and Simionescu, 1984). A schematic of the ECs which make up the capillary wall is shown in Figure 2.2. The spaces in between ECs are known as intercellular clefts, which are about 20 nm wide and occupy only 0.2-0.4% of the capillary surface. Rows of protein particles called junction strands seemingly block the pathway between the cells, but in fact there are periodic breaks of about 150 nm that allow for molecules to traverse a tortuous path across the capillary wall (Adamson and Michel, 1993). Lining the luminal (internal) surface of ECs is a negatively charged carbohydrate-rich layer known as the *endothelial glycocalyx*, which is made up of proteoglycans, glycoproteins, glycosaminoglycan (GAG) chains, and plasma proteins (Pries et al., 2000; Weinbaum et al., 2007). An electron microscope image of the glycocalyx is shown in Figure 2.2. The glycocalyx plays an important role in transcapillary flow, and this will be discussed in more detail in Section 2.6 as it pertains to the ultrastructural model of Hu and Weinbaum (1999), and in Chapter 4, where we discuss in depth the effect of the glycocalyx parameters on our model of transcapillary flow. For the moment it suffices to say that the glycocalyx contributes to the selectivity of the capillary wall in that it excludes molecules beyond a certain size from passing through, and also acts as a resistance barrier to flow. On the abluminal side the basal lamina, or basement membrane, is present. This layer of approximately 50-100 nm thick provides most of the mechanical strength of the capillary, protecting it against rupture. Also present in the capillary wall are caveolae and vesicles, which transport macromolecules first into the cell, then across it.

Once a molecule has passed through the capillary wall, it must traverse a porous matrix known as the *interstitial space* (or interstitium) before reaching the cells of the tissue. The interstitium occupies the space between the parenchymal cells (parenchyma refers to the functional part of a tissue) and has the primary function of being a mediator of exchange between the vasculature and cells of a given

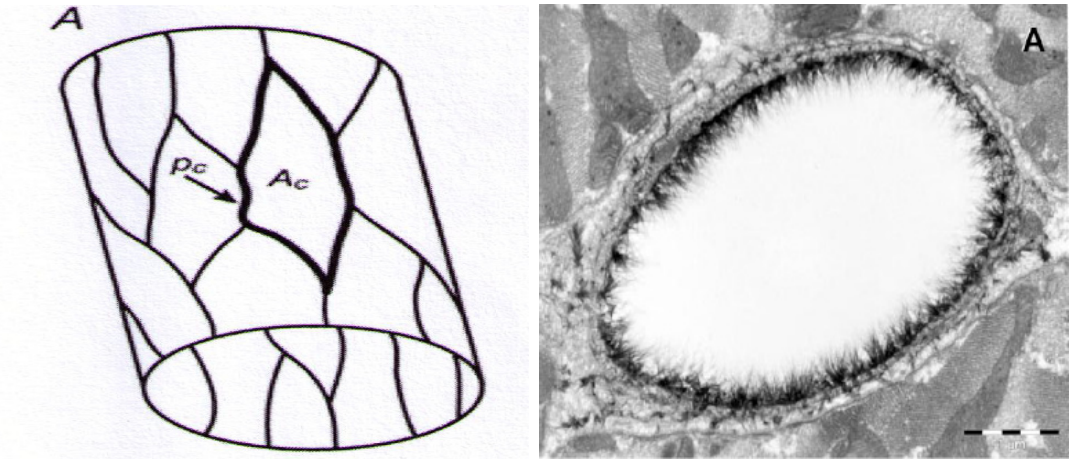

Figure 2.2: Left – The perimeter of an endothelial cell is traced out. This is the region known as the intercellular cleft. Reproduced from Adamson et al. (2004) with permission. Right – The hair-like protrusions on the luminal side of the capillary wall are the endothelial glycocalyx. Reproduced from van den Berg et al. (2003) with permission.

tissue. It is a gel-like material, composed of a complex three-dimensional network of biopolymers which make up the solid phase, and a solution of electrolytes and plasma proteins which make up the fluid phase. Collagen fibrils and microfibrils serve as tensile elements of the matrix, and GAG chains serve as the water-attracting expansion elements. The minute spaces of the GAG matrix (as small as 3 nm in cartilage) contain interstitial fluid, and the fact that their resistance is large (or equivalently that their conductivity is small) is what gives the interstitium its gel-like nature (Levick, 2003). The study of the interstitial fluid pressure (IFP) and its impact on the tissue microenvironment has long been an area of interest, ever since Guyton (1963) showed that IFP was subatmospheric in many tissues, usually between -1 and -3 mmHg. For tissue volume homeostasis, there must be a mechanism to clear the excess fluid and plasma proteins away from the interstitial space. This is the job of the *lymphatic system*.

The lymphatic system has three main functions. First, it preserves fluid balance in tissues by returning the capillary blood ultrafiltrate and escaped plasma proteins back to the bloodstream. Second, it has a nutritional function, as intestinal lymph vessels absorb and transport digested fat. Finally, it acts as a defense mechanism for the body. Fluid draining from the interstitium carries foreign materials (i.e. antigens, viruses, bacteria) to the lymph nodes, where particulate matter can be filtered out and phagocytosed, while bacterial and viral antigens activate lymphocytes (a type of white blood cell), thus stimulating their release into the

bloodstream. The lymphatic system has a hierarchy similar to that of the regular circulation. Lymphatic capillaries take up proteins, particles and fluid, then pass these on to collecting (or afferent) lymphatics, which pump the lymph through active contraction of smooth muscle cells. The material arrives in the lymph nodes, which as mentioned contains lymphocytes and phagocytic cells. Lymphocyte-rich efferent lymph then moves to the thoracic duct, which empties into the left subclavian vein at its junction with the jugular vein, where it re-enters the circulation. The rate of lymph formation is dependent on both the interstitial fluid pressure and volume. Since pressure and volume are directly related to capillary filtration, they provide a link necessary to match lymphatic drainage rate to capillary filtration rate, thus maintaining homeostasis (Levick, 2003).

In the late 19th century, the general belief was that once interstitial fluid was formed (by filtration of fluid through the capillary wall), the only mechanism by which it could return to the circulation was via the lymphatic system. However, there was some evidence that interstitial fluid could pass directly into the blood: if dyes were injected into the pleural or peritoneal cavity, they could sometimes be detected in the urine before the thoracic duct lymph. This suggested that solutes may diffuse *from the tissue directly into the blood*. The physiologist E.H. Starling wondered whether this was also the case for fluids (Michel, 1997), and in his now famous experiments, he showed that this was indeed the case.

2.2 Starling's work

Starling (1896) set up a series of experiments to test the hypothesis that fluids could be absorbed directly into the blood. It had been known for some time that upon haemorrhage (bleeding), the blood and plasma become diluted, which had earlier been believed to be due to increased lymph flow. The reasoning was that lymph was less concentrated than the blood, and so an increase in lymph flow would add the necessary amount of fluid to the circulation that was lost due to haemorrhage, resulting in dilution. Starling's first experiment involved inducing haemorrhage in a dog and diverting the lymph away from the circulation. If the dilution still took place, it could not be attributed to excess lymph flow, but rather would imply that some other mechanism was responsible. Since the interstitial fluid was also less concentrated than the plasma, there was the possibility that it was this fluid that was responsible for 'topping up' the circulation. Indeed the dilution occurred,

leading Starling to argue that fluid must be absorbed by the blood vessels directly from the tissue.

In the next experiment, the circulation in the hindlimb of a dog was isolated by cannulation of the femoral arteries and veins. One leg was to serve as control, while the other was injected with a 1% salt solution to make it oedematous (swollen due to excess fluid). Blood was then passed through each hindlimb at pressures of 65-85 mmHg and collected; this process was repeated 12-24 times. After the experiment, the blood composition was analysed. In the control, the blood was either unaltered or slightly concentrated, whereas in the oedematous leg, the blood and serum had undergone significant dilution. Since the limb was isolated, it followed that the only way dilution could occur would be if fluid moved from the interstitial compartment into the blood. This proved that absorption of fluid directly from tissue to vessel could occur, and Starling stated, "...we may affirm with certainty that isotonic salt solution can be taken up directly by the blood circulating in the blood vessels" (Starling, 1896).

In search of a mechanism, Starling suggested that the higher concentration of proteins in the plasma than in the interstitial fluid led to a small osmotic pressure difference across the capillary wall (we explain osmotic pressure in detail in Section 2.4.1). He conducted two osmosis experiments and found that the osmotic pressure of the plasma was between 30-40 mmHg, interestingly in the same range as the capillary hydrostatic pressure. The following became known as Starling's hypothesis:

> [t]he importance of these measurements lies in the fact that, although the osmotic pressure of the proteids [*sic*] of the plasma is so insignificant, it is of an order of magnitude comparable to that of the capillary pressures; and whereas capillary pressure determines transudation, the osmotic pressure of the proteids [*sic*] of the serum determines absorption...so at any given time, there must be a balance between the hydrostatic pressure of the blood in the capillaries and the osmotic attraction of the blood for the surrounding fluids. (Starling, 1896)

Starling's hypothesis led him to the idea that since capillary pressures at the arterial end of the capillary bed were greater than those at the venous end, there should be filtration of fluid from the capillaries at the arterial end, and reabsorption of fluid into the capillaries at the venous end (Michel, 1997). This became the standard picture for the next hundred years.

Starling's work did not immediately catch on as some were still skeptical of the role of osmotic pressure, or dismissed his views as too mechanical and simplistic. Direct experimental evidence did not arise for another 30 years, until the work of E.M. Landis.

2.3 Experimental evidence in support of Starling's hypothesis

Landis (1927) set out to determine whether the hypothesis of Starling was correct. He performed two sets of experiments: one in which the movement of fluid through the capillary wall could be seen qualitatively by injecting solutions of dyes, and another in which the rate of fluid passage through the endothelium was directly measured by the motion of red blood cells (RBCs) in the capillary.

Krogh (1922) had previously suggested that the passage of dyes was related to capillary diameter, which was contrary to Starling's hypothesis, where the passage should depend on capillary pressure. Landis measured capillary diameter and pressure in a number of capillaries and indeed found that "...the rate of passage...is dependent upon the level of capillary pressure" (Landis, 1927), whereas no correlation was found with vessel diameter.

The second set of experiments involved an ingenious technique, which in effect is still used today. A capillary is perfused with blood, where one end of the capillary is closed and the RBCs visible. If there is filtration of fluid from the capillary, the RBCs will move toward the closed end, whereas if reabsorption is occurring, the RBCs will move away from the closed end to make room for the added fluid. The pressure and diameter of the vessel, and position of an RBC at various times are measured, as shown in Figure 2.3 (left). By finding the tangent to the position vs. time curves at time equal to zero, the velocity of the RBC is found, which when multiplied by the capillary cross-sectional area, gives the rate at which fluid was being filtered or absorbed. If this quantity is then divided by the surface area of the vessel, the "unit rate of fluid movement in cubic micra per square micron of capillary wall per second" (Landis, 1927) is obtained.

When this rate of fluid passage is plotted against capillary pressure (Figure 2.3-right), a linear relationship is found, with filtration for pressures greater than

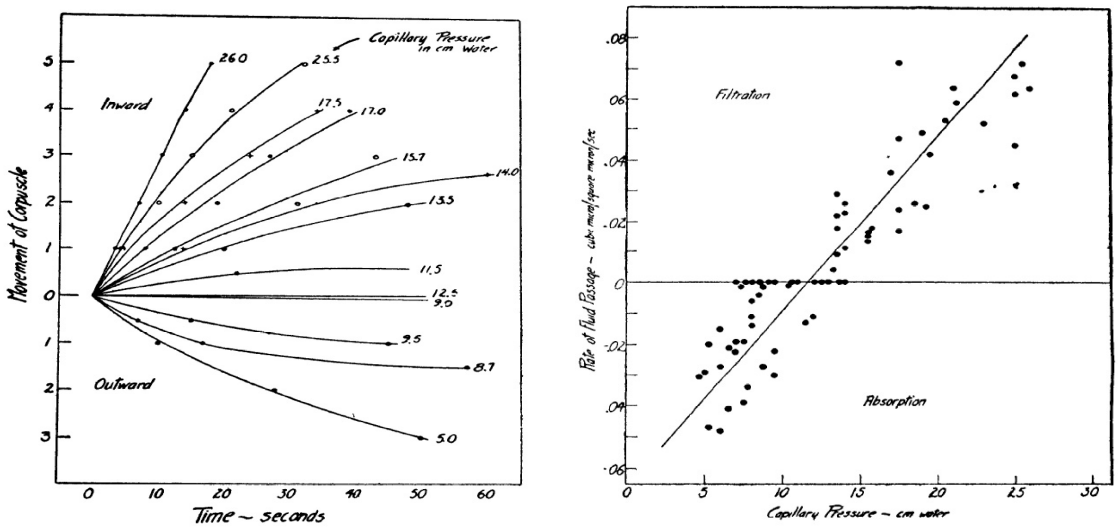

Figure 2.3: Left - Position of RBC as a function of time. Note the tangent to the curve at zero time gives the RBC velocity. Right - Rate of fluid movement as a function of capillary pressure. Taken from Landis (1927).

14 cmH_2O and reabsorption for pressures below 7 cmH_2O. Between these two pressures, which importantly was in the range of estimates for osmotic pressure of frog plasma, the fluid movement was near zero. Thus, the rate of fluid movement was directly proportional to the difference between capillary hydrostatic and osmotic pressures – exactly Starling's hypothesis. Landis also noticed that the slope of this line was an important quantity, now known as the hydraulic conductivity, and estimated its value as $6\times\ 10^{-7}$ cm s^{-1} cmH_2O^{-1}, which is amazingly very close to the estimates of today. These results also appeared to conform to the idea of arterial filtration and venous reabsorption. Landis went on to further investigate the effects of hypoxia on filtration (Landis, 1928) and measure the capillary pressure in human subjects (Landis, 1930).

The most definitive evidence of Starling's hypothesis in mammalian capillaries was the work of Pappenheimer and Soto-Rivera (1948), who made the first measurements of fluid movement and the Starling forces in mammalian capillaries. They perfused blood through the circulation of cat or dog hindlimbs such that they could control the arterial and venous pressures, as well as the protein osmotic pressure of the plasma. They also made use of a theoretical expression for the mean capillary pressure based on the arterial and venous pressures as well as the pre- and post-capillary resistances. By monitoring the weight of the limb, they could infer either filtration of fluid from blood to tissue (weight gain) or reabsorption of fluid from tissue to blood (weight loss). They called the state at which the perfused limb was

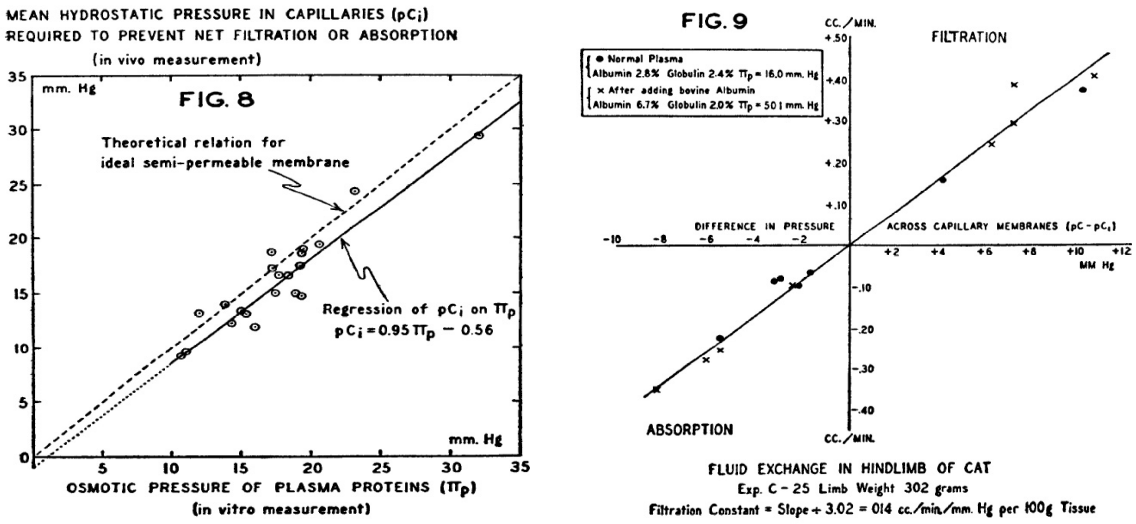

Figure 2.4: Left - Mean isogravimetric capillary pressure and plasma osmotic pressure. Right - Filtration or absorption of fluid as a function of the difference between the mean capillary pressure and its isogravimetric value. Taken from Pappenheimer and Soto-Rivera (1948).

constant the *isogravimetric state*, and the capillary pressure required to obtain this state the *isogravimetric capillary pressure*, denoted pC_i. In this state, clearly there is no transfer of fluid.

By perfusing vessels at varying protein concentrations (and hence osmotic pressures), they found that the isogravimetric capillary pressure varied directly with the plasma osmotic pressure (with a small discrepancy, attributable to the osmotic pressure of the tissue fluid), as shown in Figure 2.4 (left). Thus, pC_i is a measure of the sum of all forces opposing filtration, the dominant one being the plasma osmotic pressure, denoted π_p in the Figure. In addition, the filtration or absorption of fluid was found to be proportional to the difference between the mean capillary pressure, and its value in the isogravimetric state (Figure 2.4 - right). This directly showed for the first time in mammalian capillaries that fluid movements across vessel walls are determined by differences in hydrostatic and osmotic pressures, and thus that Starling's hypothesis was correct.

Both Landis (1928) and Pappenheimer and Soto-Rivera (1948) wrote down an equation to describe their observations. It looked as follows:

$$F = k(P - p) \tag{2.1}$$

where F was the amount of fluid filtered (F positive) or reabsorbed (F negative), P was the capillary pressure, p was called the effective osmotic pressure of the plasma

proteins by Landis and the isogravimetric capillary pressure by Pappenheimer and Soto-Rivera, and k was termed the filtration coefficient.

By looking at the thermodynamics of membrane transport, it is possible to obtain an equation similar to this, and this has become known as the Starling equation. In the following section, a mathematical framework for transcapillary exchange is developed using arguments from nonequilibrium thermodynamics.

2.4 Mathematical framework for transcapillary exchange

2.4.1 Osmotic pressure

Consider the situation in Figure 2.5, in which there is a two-compartment tank. In compartment A there is pure solvent (water), and in compartment B there is a solution of solvent and a single solute. The two compartments are separated by an ideal semipermeable membrane, which has the characteristic that solvent molecules may freely pass through, but solute molecules cannot. There will be a flux of solvent in both directions; however, due to the presence of the solute in compartment B and its inability to pass through the membrane, there is a force exerted on the membrane by the solute molecules such that there will be a pressure difference between the two compartments. The system will be in thermodynamic equilibrium only when the leftward and rightward fluxes are balanced, and so the *excess pressure required in compartment A to prevent bulk flow* is referred to as the osmotic pressure, denoted by π. It helps to think of osmotic pressure as an attractive force, in that the bulk flow will be driven to the compartment with the higher osmotic pressure. In this sense the solute molecules are responsible for an *osmotic attraction* of the bulk fluid, which is precisely what Starling described.

The van't Hoff Law gives us a relation between the osmotic pressure of the solution and the concentration of solute, which is

$$\pi = RTC \tag{2.2}$$

where R is the universal gas constant, T is the temperature, and C is the solute concentration. Note the analogy to the ideal gas law since $C = \frac{n}{V}$, where n is the

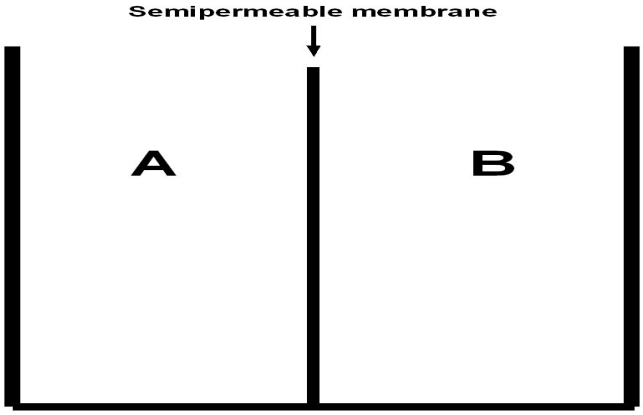

Figure 2.5: A system with two compartments separated by an ideal semipermeable membrane. Compartment A contains only solvent while compartment B contains a solution.

number of moles and V is the volume. In this case we refer to the assumption as that of an ideal solute. We also require that the solution be dilute – that is, that the number of solute molecules is much less than the number of solvent molecules in the solution.

In the presence of multiple solutes (say N), each will make a contribution to the osmotic pressure, and we can extend the van't Hoff Law as follows

$$\pi = RT \sum_{i}^{N} C_i$$

where i refers to the ith solute.

For solutions of macromolecules (which is important in physiological flows), the van't Hoff equation is a good approximation for low concentrations only. For higher concentrations, various polynomial functions of C have been used to fit experimental data (Michel, 1984; McDonald and Levick, 1993). Before describing the relations for flow across a membrane, we must first understand the idea of phenomenological equations.

2.4.2 Phenomenological equations

Phenomenological equations, sometimes called phenomenological laws, are often just experimental relations which are found to hold between certain variables. Fick's

Law, which states that the diffusional flow is proportional to the concentration gradient, and Fourier's Law, which states that the rate of heat transfer is proportional to the temperature gradient, are examples of phenomenological laws. As equations, these are written as:

$$J_1 = -D\nabla C \tag{2.3}$$

$$J_2 = -K\nabla T \tag{2.4}$$

where the J_i's are the fluxes of diffusing substance and heat, respectively, C is the concentration, T is the temperature, D is the diffusion coefficient and K is the thermal conductivity. These equations simply express the fluxes as functions of the thermodynamic forces acting, where the forces are ∇C and ∇T. Interestingly, if the system containing the diffusing particles is exposed to a temperature gradient, there will be an effect on the diffusional flow. To treat this problem, one must look at the *dissipation function*.

The dissipation function Φ is proportional to the rate of production of entropy due to heat flow across a volume element, so that $T\Phi$ is the rate of dissipation of free energy (Onsager, 1931). Thus, for Fick's Law, the dissipation function is $\Phi = J_1\nabla C$. In the presence of multiple flows and forces (as in the case of diffusion with temperature gradient), Onsager (1931) showed that all thermodynamic flows can be written as functions of the various thermodynamic forces. For a system in which n simultaneous flows take place, where each flow has an associated force, the phenomenological equations are

$$\begin{aligned} J_1 &= L_{11}X_1 + L_{12}X_2 + ... + L_{1n}X_n \\ J_2 &= L_{21}X_1 + L_{22}X_2 + ... + L_{2n}X_n \\ &\vdots \\ J_n &= L_{n1}X_1 + L_{n2}X_2 + ... + L_{nn}X_n \end{aligned}$$

where J_i refers to the flux of the ith species, X_i refers to the force due to the ith species, and the L_{ij}'s are coefficients. For the case of pure diffusion, the force is $X_i = \nabla C$, and the coefficient L_{ii} is just the diffusion coefficient D. In the case of multiple flows and forces, the cross-coefficients $L_{ij}, i \neq j$ are non-zero, which is what produces the coupling between, in this instance, diffusion and heat flux. Further, Onsager (1931) showed the equality of the cross-coefficients ($L_{ij} = L_{ji}$) and discussed the conditions under which this assumption would hold. Thus, not only will the temperature gradient affect the diffusional flux, but also the concentration gradient affects the heat flux.

The linearity of the phenomenological equations is only valid for systems close to equilibrium; however, the vast range of phenomena described accurately by such equations justifies their continued use. As long as we can write the dissipation function as a product of flows and forces, we may use the phenomenological equations. For the general system of n equations above, we write the dissipation function as

$$\Phi = \sum_{i}^{n} J_i X_i$$

We will now use these ideas, along with our knowledge of osmotic pressure, to describe transport across a membrane, which turns out to be extremely useful in the description of transcapillary flow.

2.4.3 Membrane transport

From the phenomenological equations of the previous subsection, we now attempt to describe flows across capillary walls, idealizing the capillary wall as a membrane. This discussion is taken for the most part from the excellent text of Katchalsky and Curran (1965). The assumptions are as follows: 1) there are two compartments, separated by a membrane of thickness Δx, 2) compartments may contain substances that may either permeate the membrane or not, 3) compartments may have a hydrostatic pressure difference but are taken as well-stirred so there are no pressure gradients within each compartment, 4) the flow passing through the membrane is perpendicular to its surface and one-dimensional.

For a system of n solutes, the dissipation function is

$$\Phi = \sum_{i}^{n} J_i \Delta\mu_i$$

where J_i is the flow, $\Delta\mu_i$ is the change in chemical potential across the membrane, and i refers to the ith solute. The chemical potential is defined as the change in Gibbs free energy for a given change in the number of moles in the system. If we simplify to a system of a single solute and solvent, then

$$\Phi = J_s \Delta\mu_s + J_w \Delta\mu_w \tag{2.5}$$

where s and w refer to the solute and solvent (water), respectively. We can write down the phenomenological equations at this point, but it is of interest to transform the chemical potentials into more useful quantities. From considerations of

statistical mechanics, we may write

$$\mu_w = \mu_w^0 + \overline{V}_w P + \mu_w^c$$

where μ_w^0 is a constant (reference chemical potential – plays no role as only changes in μ are important), $\overline{V}_w$ is the partial molar volume, P is pressure, and μ_w^c is the concentration-dependent part. Then

$$\Delta\mu_w = (\mu_w)_0 - (\mu_w)_{\Delta x} = \overline{V}_w(P_0 - P_{\Delta x}) + (\mu_w^c)_0 - (\mu_w^c)_{\Delta x}$$

which simplifies to

$$\Delta\mu_w = \overline{V}_w \Delta P + \Delta\mu_w^c \tag{2.6}$$

using the fact that Δ simply refers to the difference across the membrane. The concentration-dependent part can be written

$$\Delta\mu_w^c = -\overline{V}_w RT(c_s^0 - c_s^{\Delta x}) = -\overline{V}_w \Delta\pi$$

which gives

$$\Delta\mu_w = \overline{V}_w(\Delta P - \Delta\pi) \tag{2.7}$$

The chemical potential of the solute is

$$\Delta\mu_s = \overline{V}_s \Delta P + \Delta\mu_s^c$$

and defining an average concentration $\overline{c}_s = \dfrac{\Delta\pi}{\Delta\mu_s^c}$, gives

$$\Delta\mu_s = \overline{V}_s \Delta P + \frac{\Delta\pi}{\overline{c}_s} \tag{2.8}$$

For ideal solutions we have that $\Delta\mu_s^c = RT(\ln c_s^0 - \ln c_s^{\Delta x})$ and $\Delta\pi = RT(c_s^0 - c_s^{\Delta x})$, so substituting in the definition of $\overline{c}_s$ we obtain

$$\overline{c}_s = \frac{c_s^0 - c_s^{\Delta x}}{\ln \dfrac{c_s^0}{c_s^{\Delta x}}}$$

Assuming the ratio of the concentrations on either side of the membrane to be close to one, we can expand the logarithmic terms in a Taylor series to find that $\overline{c}_s = \frac{c_s^0 + c_s^{\Delta x}}{2}$ is simply the average of the concentration on each side. If we now substitute equations (2.7) and (2.8) into the initial form of the dissipation function (2.5), we obtain

$$\Phi = (J_s\overline{V}_s + J_w\overline{V}_w)\Delta P + \left(\frac{J_s}{\overline{c}_s} - J_w\overline{V}_w\right)\Delta\pi \tag{2.9}$$

where the term multiplying ΔP is the total volume flow, J_v, and the term multiplying $\Delta\pi$ can be simplified in the dilute assumption (that is $\overline{V}_w = \frac{1}{\bar{c}_w}$) to the velocity of solute relative to that of the solvent, denoted by J_D. Thus in the final form, we can express the dissipation function as

$$\Phi = J_v \Delta P + J_D \Delta\pi \tag{2.10}$$

For a dissipation function of this form, we may write down the following phenomenological equations

$$J_v = L_P \Delta P + L_{PD} \Delta\pi \tag{2.11}$$

$$J_D = L_{DP} \Delta P + L_D \Delta\pi \tag{2.12}$$

Note the important limiting behaviours, as follows. In the absence of a concentration difference ($\Delta\pi = 0$) there is not only the expected volume flow $J_v = L_p \Delta P$ due to the hydrostatic pressure difference, but also a flux of solute relative to solvent, namely $J_D = L_{DP}\Delta P$. This phenomenon is called *ultrafiltration*. The sign of J_D would be opposite to J_v, since it is a relative flux, but solute molecules would still travel in the same direction as the bulk flow. In the other limit, that is in the absence of a pressure difference ($\Delta P = 0$), there is diffusional flow ($J_D = L_D \Delta\pi$), and as well a bulk flow $J_v = L_{PD}\Delta\pi$, termed *osmotic flow*. The solute will obviously diffuse from high to low concentration, whereas the osmotic flow, as mentioned above, will move in the direction toward the high concentration compartment. The Onsager relations regarding equality of the cross-coefficients gives

$$\left(\frac{J_v}{\Delta\pi}\right)_{\Delta P=0} = L_{PD} = L_{DP} = \left(\frac{J_D}{\Delta P}\right)_{\Delta\pi=0}$$

which allows determination of the constants in an experimental setting.

Rather than looking at the term J_D, it is often more useful to look at the total solute flow. In going from Eq. (2.9) to Eq. (2.10), we had

$$\begin{aligned} J_D + J_v &= \left(\frac{J_s}{\bar{c}_s} - \overline{V}_w J_w\right) + (\overline{V}_w J_w + \overline{V}_s J_s) \\ &= \frac{J_s}{\bar{c}_s}(1 + \overline{V}_s \bar{c}_s) \\ &= \frac{J_s}{\bar{c}_s} \end{aligned}$$

which is true since $\overline{V}_s \bar{c}_s \ll 1$ in the dilute case. Then the total solute flux may be expressed as the following

$$\frac{J_s}{\bar{c}_s} = J_D + J_v = (L_P + L_{DP})\Delta P + (L_{DP} + L_D)\Delta\pi$$

When there is no flux of solute (i.e. $J_s = 0$), we have the condition that $-L_{PD} = L_P = L_D$, which is the requirement of an ideal semipermeable membrane. Osmotic equilibrium is then satisfied when $(\Delta P)_{J_v=0} = \Delta\pi$, which conforms to the definition of osmotic pressure above. However, to describe membranes which are not ideal, that is when the solute molecules may also pass through, a new coefficient must be introduced.

The reflection coefficient, σ, is a measure of the selectivity of the membrane to a particular solute, and thus depends on both the properties of the membrane and solute. The ideal semipermeable membrane corresponds to $\sigma = 1$; that is, all of the solute is 'reflected', and the entire osmotic pressure $\Delta\pi$ is exerted across the membrane. For $\sigma < 1$, solute may penetrate the membrane, and thus the full osmotic pressure is not felt, but only the fraction $\sigma\Delta\pi$. For $\sigma = 0$, the solute molecules will freely traverse the membrane and so there is no osmotic pressure effect. Staverman (1951) first realized the importance of this parameter, defined as

$$\sigma = -\frac{L_{PD}}{L_P}, \quad 0 \leq \sigma \leq 1 \tag{2.13}$$

Substitution for L_{PD} in the phenomenological equation (2.11) gives

$$J_v = L_P(\Delta P - \sigma\Delta\pi) \tag{2.14}$$

which can be expressed as a volume flux per unit area, albeit with a reinterpretation of the dimensions of the constant L_P, as

$$\frac{J_v}{A} = L_P(\Delta P - \sigma\Delta\pi) \tag{2.15}$$

where A is the area available for exchange.

Let us now return to what Starling proposed, namely that the hydrostatic pressure of the capillary determines filtration of fluid and that the osmotic pressure determines absorption. If we now think of the inside of the capillary as one side of a semipermeable membrane, and the outside of the capillary, or interstitial space, as the other side, with the capillary wall playing the role of the semipermeable membrane, then Eq. (2.15) is exactly Starling's hypothesis. We may write $\Delta P = p_c - p_i$ and $\Delta\pi = \pi_c - \pi_i$, where subscript c refers to the capillary, and i refers to the interstitial space, such that Eq. (2.15) now reads

$$\frac{J_v}{A} = L_P(p_c - p_i - \sigma(\pi_c - \pi_i)) \tag{2.16}$$

Starling may not have fully appreciated the p_i, π_i terms, as values for these were not known until much later on, but his hypothesis of the forces involved proved to be correct. This is why we may refer to his hypothesis as Starling's principle. And although Starling himself never wrote down Equation (2.16), it is often and will herein be referred to as the Starling equation.

Compare the Starling equation to that written by Landis (1927) and Pappenheimer and Soto-Rivera (1948), namely Eq. (2.1). The role of F is now played by $\frac{J_v}{A}$, such that when $\frac{J_v}{A}$ is positive, this signifies filtration, and when $\frac{J_v}{A}$ is negative, there is reabsorption. The capillary pressure still occurs, now denoted by p_c rather than P, and the coefficient k is now written as L_P. The p term, called the *effective osmotic pressure of the plasma proteins* by Landis (1927), and the *isogravimetric capillary pressure* by Pappenheimer and Soto-Rivera (1948), contains p_i, the interstitial hydrostatic pressure, as well as $\sigma(\pi_c - \pi_i)$, which is the effective osmotic pressure – the difference between that in the capillary and that in the interstitial space multiplied by the reflection coefficient.

We may generalize this system to one which contains n solutes, which accounts for the fact that many different molecules flow through capillary walls. Each solute in the plasma makes a contribution to the osmotic pressure, and we may thus write a more correct form of the Starling equation as

$$\frac{J_v}{A} = L_P(\Delta P - \sum_j \sigma_j \Delta\pi_j)$$

where j refers to the jth solute. However, albumin has a dominant effect, since for small molecules the reflection coefficient will be close to zero, negating the osmotic effect, whereas for $\sigma_{albumin} \approx 0.9$. So the Starling equation is often written in the first form (2.16), with the understanding that albumin is the solute responsible for the osmotic effect.

The field of transcapillary exchange is one which has truly developed due to the work in concert of experimentalists and theoreticians. Theoretical developments stimulated experimental work, and experiments drove the development of more adequate theories. By perfusing a capillary at a known protein concentration (and hence π_c) at different hydrostatic pressures (p_c) and measuring the filtration $\frac{J_v}{A}$, one obtains an estimate of L_P, the hydraulic conductivity, by measuring the slope of the line. This is precisely what Landis (1927) did, well before any of this theoretical background was developed. In addition, at the capillary pressure for which there is no filtration (i.e. $\frac{J_v}{A} = 0$), we see that $\Delta P = \sigma\Delta\pi$, and thus with knowledge of p_i

and π_i one can estimate the value of σ. Much of the work through the 1950s to 1980s was performed to measure the reflection coefficients and hydraulic conductivities in various capillary networks, in different animals, etc. (Smaje et al., 1970; Curry et al., 1976; Mason et al., 1977; Michel, 1978, 1980).

The theoretical work also made predictions about phenomena that had yet to be observed, but which were seen experimentally later. The rest of this section is devoted to a theoretical development which predicted that, in the steady-state, there could be no reabsorption of fluid. This would contradict Starling's hypothesis, and take many years of theory and experiment to resolve.

We had an expression for the solute flow J_s in terms of J_v and J_D, namely

$$\frac{J_s}{\overline{c}_s} = J_D + J_v$$

Eliminating ΔP from the phenomenological equations and inserting the solute flux J_s gives

$$J_s = \overline{c}_s(1-\sigma)J_v + \overline{c}_s(L_D - \sigma^2 L_P)\Delta\pi \tag{2.17}$$

where we have used the definition of the reflection coefficient σ. As stated by Curry (1984), this equation has useful approximations, but is actually only a linearised version of a more general relation. Following Patlak et al. (1963) we assume that since the phenomenological equations apply to a thin, homogenous membrane, then "we may convert them to a differential form which will apply to any infinitesimal lamina of a thick homogeneous membrane" (Patlak et al., 1963). This essentially allows us to write the differences in pressure and osmotic pressure across the membrane as gradients. We take the positive flux in the direction of increasing x, and let the membrane thickness be δ. The differential forms are then

$$J_v = -L'_P\left(\frac{dp}{dx} - \sigma RT\frac{dc}{dx}\right) \tag{2.18}$$

$$J_s = (1-\sigma)cJ_v + \omega' RT\frac{dc}{dx} \tag{2.19}$$

where we can compare with Eq. (2.14) and Eq. (2.17). First, notice that c is now used instead of π, and also that there is a negative in front of the coefficient in the first equation due to the fact that the flux is in the direction of the negative pressure gradient. In the second equation, the constant $\omega' = \overline{c}_s(L_D - \sigma^2 L_P)$. Also, the average concentration $\overline{c}_s$ has been replaced with the actual concentration, c. However, although c appears in the term multiplying J_v, ω' is still assumed to be a constant – thus $\overline{c}_s$ is still used in its definition. We remove this assumption when deriving the equations for our model in Chapter 3.

By assuming that the parameters L'_P, ω', σ are concentration independent, and that the steady state is obtained so that J_v, J_s will be constant, we may integrate the first equation to obtain

$$J_v = -L_P(\Delta p - \sigma RT\Delta c)$$

where the only difference with the Starling equation is the sign convention, and $L'_P = \delta L_P$. The second equation is a linear, first order differential equation for $c(x)$ which can be integrated to give

$$c_2 = c_1 \exp\left[\frac{(1-\sigma)J_v}{P}\right] + \frac{J_s}{(1-\sigma)J_v}\left(1 - \exp\left[\frac{(1-\sigma)J_v}{P}\right]\right) \tag{2.20}$$

where $P = \dfrac{\omega' RT}{\delta}$ is the solute permeability, c_2 is the concentration corresponding to $x = \delta$ and c_1 is the concentration at $x = 0$. We introduce the Peclet number, which is a measure of the ratio between convective and diffusive fluxes, defined as $Pe = \dfrac{(1-\sigma)J_v}{P}$, and rearrange (2.20) to obtain

$$J_s = J_v(1-\sigma)\left[\frac{c_1 - c_2 e^{-Pe}}{1 - e^{-Pe}}\right] \tag{2.21}$$

Application to steady state ultrafiltration

We let $c_1 \to C_c$, the capillary protein concentration, and $c_2 \to C_i$, the interstitial protein concentration, in Equation (2.21). In the steady state, the concentration of protein in the tissue must be a ratio of the solute flux to the total volume flux, therefore $C_i = \frac{J_s}{J_v}$. Then we use the expression for J_s to obtain

$$C_i = \left(\frac{1-\sigma}{1-\sigma e^{-Pe}}\right) C_c$$

Now, we replace the osmotic pressure term in the Starling equation by the concentration, using the van't Hoff Law, to obtain

$$\frac{J_v}{A} = L_P(\Delta P - \sigma RT\Delta C)$$

where $\Delta C = C_c - C_i$. We note that we are now switching notation and using $\frac{J_v}{A}$ instead of J_v, as in (2.21), and hence $\frac{J_v}{A}$ replaces J_v in the definition of the Peclet number. This is fine to do so long as we remember that we now are working with a velocity rather than a volume flow, and therefore that the dimensions of L_P must

change accordingly. Now we will substitute for C_i, but since in the expression for C_i the Peclet number occurs in the exponential, we will not be able to isolate the equation for $\frac{J_v}{A}$. Thus, we instead rearrange for ΔP

$$\Delta P = \frac{J_v/A}{L_P} + \sigma^2 \pi_c \left(\frac{1 - e^{-Pe}}{1 - \sigma e^{-Pe}} \right) \tag{2.22}$$

where we have also inserted π_c for C_c using the van't Hoff relation.

The result is a nonlinear $\frac{J_v}{A}$ vs. p_c curve, where the nonlinearity occurs for low p_c (or ΔP) such that negative values of $\frac{J_v}{A}$ do not occur – this implies that there can be no reabsorption of fluid from tissue to the blood in the steady state, which would contradict Starling's hypothesis and previous experimental evidence. This prediction was later confirmed experimentally by Michel and Phillips (1987), in an experiment which will be discussed shortly. Another consequence of this theoretical development is that in the limit of high filtration, the Peclet number is large, so the exponential terms in Equation (2.22) vanish, and we can rearrange this to obtain

$$\frac{J_v}{A} = L_P(\Delta P - \sigma^2 \pi_c) \tag{2.23}$$

which suggests that the osmotic pressure opposing filtration is $\sigma^2 \pi_c$ in the high filtration limit, rather than $\sigma \pi_c$. This was also confirmed experimentally by Michel and Phillips (1987).

2.4.4 Pore Theory and the Fiber Matrix Model

The similarities between permeability characteristics of capillaries and artificial porous membranes led to the *Pore Theory* of capillary exchange (Pappenheimer et al., 1951). This theory assumes that the capillary wall has numerous microscopic openings that allow the movement of water and small solutes, but restrict the transport of plasma proteins. Using the assumption that Poiseuille's law is valid in these microscopic pores, one can find expressions for the volume flux in terms of the pressure difference across a pore, the length, radius and number of pores, and fluid viscosity. These quantities can be then used to calculate the hydraulic conductivity, L_P. Alternatively, since L_P is experimentally measurable, then using its measured value, one can find a relation for an equivalent pore radius characteristic of the resistance to water flow through the channels of the porous membrane (Curry, 1984). A key idea in pore theory is that of restricted diffusion, in which the effective diffusion coefficient depends on the ratio of solute radius to pore radius. In this

way, solute permeability and therefore flux may be quantified in terms of the pore dimensions. Much of the experimental work was directed at finding better estimates for the reflection coefficients of various molecules.

An analysis of experimental data on ultrafiltration of macromolecules, restricted diffusion, and osmotic reflection coefficients of small solutes showed that the resistance to transport could not be described in terms of a uniform population of porous channels. Rather, the data suggested at least three pathways: 1) a small pore pathway permeable to water but that excludes hydrophilic solutes, 2) a pathway permeable to water and solutes up to the size of albumin, and 3) a large pore pathway permeable to larger solutes (Curry, 1984).

In addition, data on reflection coefficients showed similar values over large ranges of hydraulic conductivity, suggesting the idea that it was changes in pore frequency, not pore size, that accounted for variation in hydraulic conductivity. As well, in both frog mesentery and mammalian hindlimb, the predicted pore size that would account for the selectivity of the wall to albumin could not account for the measured flows of water and small solutes (Curry, 1984). Thus, pore theory is found to be inconsistent. This led to the idea that the selectivity of the capillary wall is not determined by pores with regular geometry.

Michel (1978) put forward the hypothesis that rather than pores, the molecular sieving properties of the capillary wall may be due to a three-dimensional network of fibrous molecules. To quantify this, Curry and Michel (1980) developed the *Fiber Matrix Model*, in which "[t]he porous regions of the capillary wall are considered as a series of channels through or between the endothelial cells containing a random array of cylindrical fibers" (Curry and Michel, 1980). Therefore, although it was known that there were several pathways for transport, the fiber matrix model assumes a uniform selectivity of the network, and the transport coefficients thus did not depend on geometric configuration.

In this model only two parameters must be specified: the fiber radius and fractional fiber volume. For this analysis, the partition coefficient, which is the space available in the matrix to a solute of radius a relative to the space available for water, and the effective diffusion coefficient, which arises as a result of restricted diffusion in the network, must be found. Once these are found, the permeability, hydraulic conductivity, reflection coefficient, and hence the solute and volume fluxes can be calculated in terms of the fiber radius and fiber volume fraction (Curry, 1984).

The model was tested by comparison with experimental data from single capillary and whole organ studies. It was found that the fiber matrix model could account for the hydraulic conductivity, permeability to sucrose, and osmotic reflection coefficient of albumin. Also, the dimensions of the matrix are predicted to be similar in frog mesenteric capillaries and mammalian hindlimb capillaries. In the former, a fit of the data predicts fiber radius of 0.6 nm with volume fraction 5%, whereas in the latter, a radius of 0.5 nm with volume fraction 4.5% fits the data. This interestingly leads to the idea that differences in hydraulic conductivity or permeability are not caused by differences in structure of the size-limiting barriers. Differences in magnitude of these parameters instead depend on the area and thickness of the fiber filled pathway for exchange.

2.4.5 Summary

In this section we have introduced the idea of osmotic pressure, and set out the phenomenological equations for the transport of fluid and solutes across a membrane. The forces driving the flow are the hydrostatic and osmotic differences between the two compartments. Making an analogy, the transcapillary flux of fluid and proteins can be described using these transport equations, with the capillary wall acting as the semipermeable membrane. An expression was derived that coincided with Starling's hypothesis regarding the forces driving transcapillary exchange, and this became known as the Starling equation.

What pore theory and the fiber matrix model attempted to do was characterise the microscopic details of this membrane. Since pore theory was shown to be inconsistent, yet the fiber matrix model agreed well with experimental data, the 'membrane' from transcapillary exchange was likely to be a network of random fibers. However, as touched on above, there are multiple pathways for transcapillary exchange, as shown schematically in Figure 2.6, which we take from Renkin (1977). Small molecules may move directly through the endothelial cells (1), while lipid-soluble molecules move within the cell membranes by lateral diffusion (2). Water and other hydrophilic molecules may move through the intercellular junctions (3,4,5), and vesicular transport helps the larger macromolecules traverse the capillary wall (6). In fenestrated capillaries the fenestrae provide an additional pathway. Also, the endothelial glycocalyx on the luminal side and basement membrane on the abluminal side both may provide a barrier to transport.

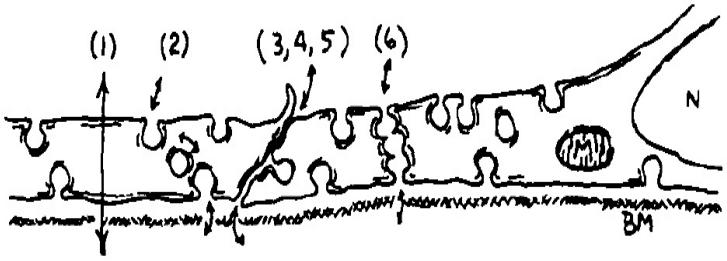

Figure 2.6: Multiple pathways for exchange. Reprinted from Renkin (1977) with permission.

So the problem is reconciling the fact that a random fiber matrix with fairly consistent structure is the barrier to transcapillary exchange, yet the multiple pathways above are observed experimentally and must be taken into account to provide a full description of the process. This led to the development of microstructural models of transcapillary exchange, in which the microscopic properties observed in experiment were taken into account in the mathematical models. We discuss the most important of these models in detail in Section 2.6.

First, however, we must re-visit the development of the theory in Section 2.4.3, which predicted that there could be no reabsorption of fluid in the steady state. This stimulated experimental work to test the hypothesis, and in the following section we discuss these experiments and their implications. It turns out that combination of the ideas from the fiber matrix model, the ultrastructural pathways, the microstructural mathematical models, and the steady state experiments lead to a new picture of transcapillary exchange, one with important consequences for fluid balance in tissues.

2.5 Steady state and transient fluid exchange

In the previous section, we obtained an expression for the Starling equation, namely

$$\frac{J_v}{A} = L_P[p_c - p_i - \sigma(\pi_c - \pi_i)]$$

Experiments on transcapillary exchange, as first performed by Landis, measured $\frac{J_v}{A}$ for different values of p_c, of course with knowledge of the protein concentration in the capillary, and hence π_c. Then, by plotting $\frac{J_v}{A}$ vs. p_c, known as a Landis-Starling diagram, the hydraulic conductivity L_P could be estimated by taking the slope of

the regression line on the data. In addition, the intercept on the p_c axis was the pressure at zero filtration, P_0, and could be found by setting $\frac{J_v}{A} = 0$, such that

$$P_0 = p_i + \sigma(\pi_c - \pi_i)$$

Another way to think of this quantity is as the *pressure opposing filtration*. In fact, this is the pressure that Pappenheimer and Soto-Rivera (1948) termed the isogravimetric capillary pressure. When $p_c > P_0$, there was filtration of fluid from the capillaries, and when $p_c < P_0$ there would be reabsorption of fluid from the tissue to capillary. Since p_c was higher at the arterial end of the capillary bed than the venous end, the classical view was that fluid was filtered at the arterial end, and reabsorbed the venous end.

Starling himself did not directly mention the interstitial hydrostatic pressure and osmotic pressure as being determinants of fluid exchange. The importance of p_i was not ascertained until much later, when Guyton (1963) found that the values were subatmospheric, in the range -1 to -3 mmHg (see also Guyton et al., 1971). Of course it was known to Starling that there were proteins in the interstitial space, so that there must be a non-zero π_i, but he described an "osmotic attraction of the blood for the surrounding fluids" (Starling, 1896), which holds true as long as $\pi_c > \pi_i$, which is indeed the case. Measurements of π_i found that it was in the range of 0.3-0.6π_c in a wide variety of tissues (Levick, 1991, and references therein). Combined with estimates for P_0 from the intercept of the Landis-Starling diagram, investigators could estimate σ.

Something Starling did appreciate, however, which was not unraveled for many years, is that the nature of transcapillary exchange is dynamic, that is to say the process is time-dependent. He explained that:

> [w]ith increased capillary pressure there must be increased transudation, until equilibrium is established at a somewhat higher point, when there is a more dilute fluid in the tissue-spaces and therefore a higher absorbing force to balance the increased capillary pressure. With diminished capillary pressure, there will be an osmotic absorption of salt solution from the extravascular fluid, until this becomes richer in proteids [*sic*]; and the difference between its (proteid) [*sic*] osmotic pressure and that of the intravascular plasma is equal to the diminished capillary pressure. (Starling, 1896)

One may comprehend this dynamic nature by close examination of each of the terms in the Starling equation. An increase in p_c causes an increase in $\frac{J_v}{A}$, but

the result of extra fluid moving into the tissue space is dilution of the interstitial fluid, so that π_i decreases. This will then act to lower $\frac{J_v}{A}$ until a new equilibrium is reached. On the other hand, decreasing p_c sufficiently produces negative values of $\frac{J_v}{A}$, hence reabsorption occurs. This causes the tissue to become concentrated, so π_i is increased and hence produces a force favouring filtration, until once again the difference in osmotic pressure across the wall equals the new capillary pressure. We explain this in more detail in 2.5.2.

These phenomena cannot be inferred directly from the Starling equation, but the idea that there could be a nonlinearity in the Landis-Starling diagram was proposed by the theory in Section 2.4.3. Let us now look at the consequences of that.

2.5.1 Michel and Phillips' experiments

Michel and Phillips (1987) set out to investigate whether the theory developed in Michel (1984), which predicted a nonlinear relation between $\frac{J_v}{A}$ and p_c in the steady state, was in agreement with experimental observations. Recall that Equation (2.22) predicted that there could be no steady state reabsorption, and Equation (2.23) predicted that in the high filtration limit, the effective osmotic pressure opposing filtration was $\sigma^2\pi_c$.

Experiments were performed to measure $\frac{J_v}{A}$ at different values of the capillary pressure, using the Landis micro-occlusion technique as in Michel et al. (1974). There were two experimental conditions – the transient experiments in which there was brief perfusion of a vessel at a certain p_c, and the steady state experiments in which p_c was changed, followed by the system being allowed to equilibrate for two minutes before the measurement. The results are shown in Figure 2.7. In the transient case, a linear relationship was found, in which there was filtration for values of p_c greater than the plasma osmotic pressure and reabsorption for values of p_c less than π_c. They found that $\Delta\pi$ approached $\sigma\pi_c$, and was approximately constant for all values of $\frac{J_v}{A}$. This is what was to be expected from the Starling equation.

The steady state case, however, showed a nonlinear relation between $\frac{J_v}{A}$ and p_c. For high values of p_c, the curve was close to that in the transient case, but when p_c was less than π_c (actually $\sigma\pi_c$), there was a sharp inflection of the curve, and $\frac{J_v}{A}$ was close to zero for all lower values of p_c. Observing the curve in Figure 2.7, it is clearly

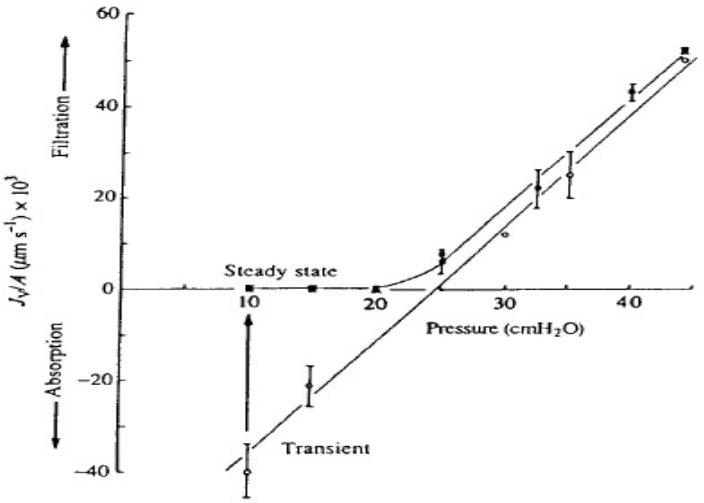

Figure 2.7: Filtration flux at various capillary pressures, in the steady state and transient state. Reprinted with permission from Michel and Phillips (1987).

seen that at no value of p_c are values of $\frac{J_v}{A}$ less than zero - this leads to the unlikely conclusion that *there can be no steady state reabsorption* in most tissues. This conflicts dramatically with the classical view of filtration at the arterial end of the capillary bed and reabsorption at the venous end. In fact, Levick (1991) showed that if the measured values were inserted into the expression for P_0, capillaries would filter fluid even at the venous end. In addition, the osmotic pressure opposing filtration was found to be $\sigma^2\pi_c$, in accordance with the theoretical development above. Reasons for these surprising results are discussed next.

2.5.2 The dynamic Starling forces

Thus, Michel and Phillips (1987) showed that reabsorption can only be a transient phenomenon, the reason for which has been described above. Specifically, the interstitial hydrostatic and osmotic pressures p_i and π_i are not only determinants of the flow, but they are also *dependent on the flow.*

Imagine a situation in which there is an elevated filtration flux (say by increasing p_c). Recall that the interstitial fluid is embedded in a tight matrix, in which there is a large resistance to flow, and the means by which this fluid is drained is via the lymphatic system. Upon an abrupt increase in filtration, fluid moves into the interstitial space, which swells due to the fact that lymphatic drainage does not occur immediately. This swelling causes a corresponding increase in IFP, quantified

by the compliance of the tissue ($C = \frac{\Delta V}{\Delta P}$ where ΔV is the volume change and ΔP is the pressure change). Now, upon examinination of the Starling equation, one observes that an increase in p_i leads to a decrease in filtration force, which pushes the system toward an equilibrium. This acts in parallel to the dilution in the tissue as explained above, which also decreases the force for filtration and pushes the system toward equilibrium. The latter is sometimes referred to as an 'osmotic buffer.'

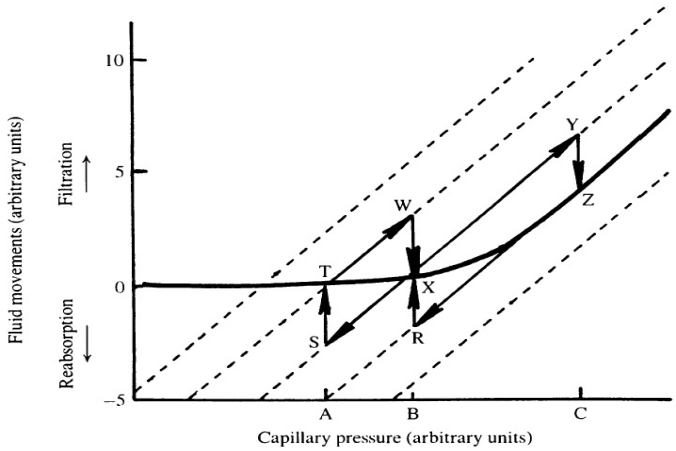

Figure 2.8: The dynamic nature of the Starling forces. Reprinted with permission from Michel (1997).

The picture is more easily understood when we examine Figure 2.8, taken from Michel's review article. Starting out at $p_c = A$, that is point T in the figure, observe that as the capillary pressure is raised from A to B, the filtration increases to the value at point W, which is that expected based on the L_P of the vessel. As the forces equilibrate, however, the filtration decreases to steady state value at $p_c = B$, point X. A similar behaviour is observed when the pressure is raised from B to C, except that the steady state at $p_c = C$ is a state of high filtration. Alternatively, when the pressure is lowered from C to B, reabsorption occurs transiently (point R) but as the forces equilibrate, point X is reached where there is a small but positive filtration; similarly for a decrease from B to A, where the steady state is reached at point T. "Transcapillary fluid absorption is thus a *self-cancelling* process, except under certain circumstances" (author's italics) Levick (1991).

2.5.3 Toward a new view

Over a sufficiently long period of time, in order for tissue volume to remain constant, there must be equilibration between the filtration through the capillaries and the lymph flow. Thus the mean p_c must exceed P_0 by an amount consistent with total lymph flow. However, the measured lymph flows were lower than would be predicted by the Starling pressures (Bates et al., 1994). This is known as the *low lymph flow paradox*.

Michel, in his brilliant review article (1997), set out to resolve this question. As mentioned above, experimental evidence pointed to two pathways across microvascular walls: a 'small-pore' pathway for water and small solutes, and a 'large-pore' pathway for macromolecules. The assumption was that the differences in hydrostatic and osmotic pressure were the same across both systems, due to rapid mixing on the tissue side of the capillary wall. However, if the mixing between the small and large pore systems happened deeper in the tissue rather than immediately outside the capillary wall, there could be large osmotic pressure differences across the small pores, as the large pores would filter a concentrated solution of proteins. In this case, the global values of π_i would overestimate the driving force (which instead of π_i would be the local osmotic pressure just outside the small pores), provided that even low filtration is sufficient to prevent diffusion of proteins toward their openings.

So the problem was to find the mechanism for a cut-off size that allowed passage of water but not macromolecules – or in other words, to find the small pores. As touched on previously, the principal pathways for fluid in continuous capillaries are the intercellular clefts. Adamson and Michel (1993) showed that there are periodic breaks in the junction strand, which makes up a continuous (albeit tortuous) pathway from lumen to tissue. These breaks are about 150 nm wide by 20 nm high, which is much larger than the size of an albumin molecule (7 nm diameter) and thus too large to be a molecular sieve – hence these could not be the small pores.

Despite the lack of knowledge of glycocalyx ultrastructure at the time, Michel (1997) proposed that the glycocalyx was the sieving matrix for albumin, and its interstices were the small pores, while the large pores were pathways through the endothelial cells, for example vesicles. Thus, the glycocalyx would play the role of the fiber matrix from the model of Michel (1980). In this case, the difference $(\pi_c - \pi_i)$ across the small pores depends on the ease of which proteins can diffuse from tissue

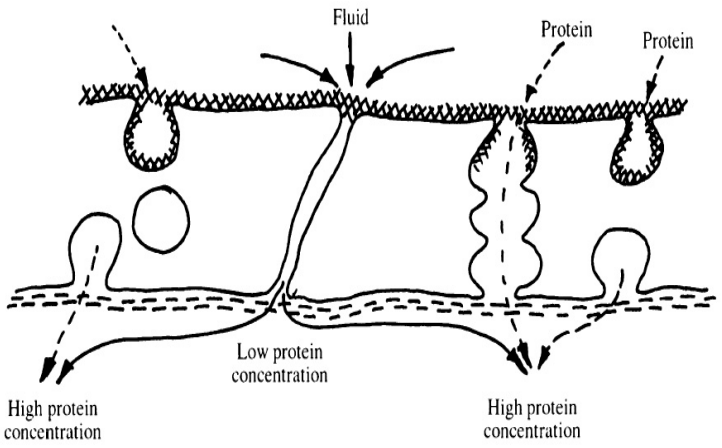

Figure 2.9: Schematic of Michel-Weinbaum hypothesis which says that the local osmotic pressure at the cleft entrance, rather than the interstitial osmotic pressure, determines the flux of fluid. Reprinted with permission from Michel (1997).

through the cleft and up to the glycocalyx. This is depicted in Figure 2.9. A comparison of the relative magnitudes of convection and diffusion (Peclet number) is thus required. If convective transport dominates, then the protein concentration at the cleft entrance may be much lower than the equilibrium interstitial concentration. Hence the force for filtration is reduced, which may explain the lower than expected lymph flows. In this sense, it is the *local* osmotic pressure at the cleft entrance, rather than the global osmotic pressure in the tissue, that will determine fluid flow. To explain this quantitatively, Weinbaum (1998) proposed an ultrastructural mathematical model; this new view of the phenomenon was therefore termed the *Michel-Weinbaum hypothesis*. The full mathematical model was given in Hu and Weinbaum (1999), and we describe the details of this model now.

2.6 New view of Starling's hypothesis

2.6.1 The mathematical model of Hu and Weinbaum

Weinbaum (1998) proposed a detailed cellular level microstructural model in which the osmotic barrier acting across capillary endothelium is the endothelial surface glycocalyx. Thus, the local Starling forces that determine flux across the endothelium are due to the hydrostatic and osmotic pressure differences across the endothelial glycocalyx, rather than the global differences between plasma and tissue. This

is a departure from the classical view of the Starling equation, and has important implications for the understanding of capillary flow. Hu and Weinbaum (1999) describe this model in detail. We first give some background that will be useful for understanding their model development.

Recall Michel and Phillips (1987) used a 1-D model that was able to explain both the transient fluid reabsorption at low capillary pressures, as well as the lack of reabsorption at steady-state. They also assumed $C_i = \frac{J_s}{J_v}$ would be the equilibrium value of the interstitial protein concentration, which assumes that the tissue outside the vessel wall behaves as a well-stirred reservoir. However, from knowledge of the junction ultrastructure (Adamson and Michel, 1993), the water flux along the length of the cleft must be spatially heterogeneous. Levick (1994) modeled water flow through fenestra in synovial capillaries and found that the local flow dilutes the solution outside the fenestra and thus reduces the local Starling forces for filtration. The model of Hu and Weinbaum seeks to explain how this occurs in continuous capillaries, using the analogy that the water flux through breaks in the junction strand will be similar to that through fenestrae. The essential element of their model is the coupling of these fluxes to cellular level structure, including the glycocalyx, interendothelial cleft with junction strand, and the mixing region at the cleft exit.

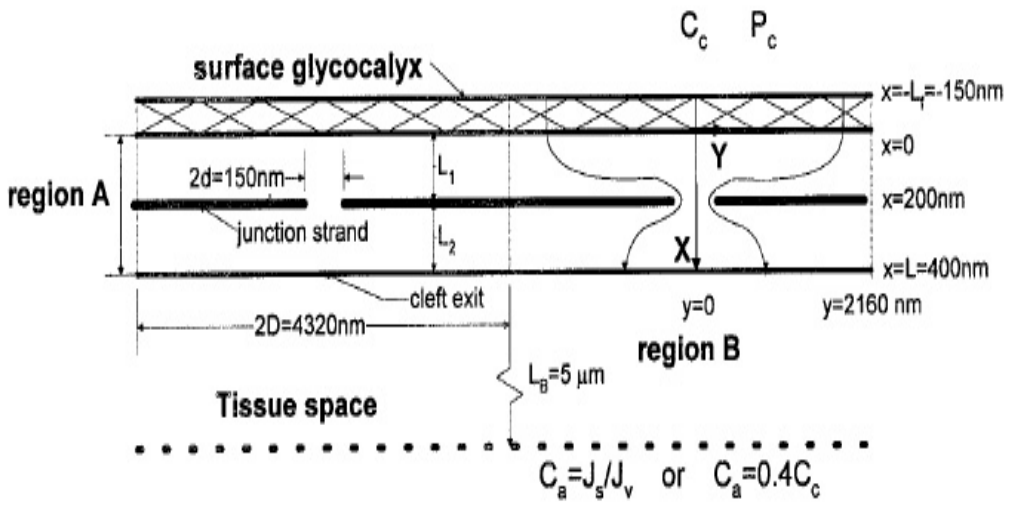

Figure 2.10: The microstructural model of Hu and Weinbaum (1999). Reprinted with permission.

The model follows earlier ultrastructural models of Fu et al. (1994, 1997) and Weinbaum et al. (1992), which seek to predict the transport coefficients such as L_P

and P in terms of the structural properties. We show a schematic of the model in Figure 2.10. There are four regions. First, a surface glycocalyx of thickness L_f which covers the entire endothelial surface. The second is region A, the cleft, which extends from $x = 0$ to $x = L$, where the cleft depth is taken as 400 nm. The cleft contains a junction strand at its mid-depth, with breaks or pores on average 150 nm long with spacing between 2 and 5 μm. The cleft height $2h$ is not shown here, but extends out of the page; the schematic is a cross-section only. The pericapillary space is broken into two separate regions. Region B is a semi-circular region of 5 μm radius which surrounds the cleft exit, and this is the region where mixing of the wakes from the junction strand breaks takes place. Region C is the far-field, where the flows from individual breaks and adjacent clefts merge to form a uniform flux.

We first describe the pressure and velocity fields, before moving onto the concentration field. In the fiber matrix (glycocalyx), the new version of Starling's hypothesis is applied, i.e. the local velocity is proportional to the hydraulic pressure and oncotic pressure across the glycocalyx (note *oncotic* simply refers to osmotic pressure of proteins),

$$\overline{V}(y) = \frac{K_p}{\mu L_f}[P_c - P(0,y) - \sigma_f(\pi_c - \pi(0,y))] \tag{2.24}$$

where $\overline{V}(y)$ is the local average velocity at location y, P_c and π_c are the capillary hydrostatic and osmotic pressures, σ_f is the reflection coefficient of the fiber matrix, K_p is the Darcy permeability of the glycocalyx, L_f is the glycocalyx thickness, and μ is the fluid viscosity. Note $x = 0$ corresponds to the region just below the glycocalyx at the entrance to the cleft, and hence $P(0,y)$ and $\pi(0,y)$ refer to the hydrostatic and osmotic pressures at this $x-$value. The fact that these quantities vary along the cleft entrance (in the $y-$direction) is precisely the spatial heterogeneity that differentiates this from the classical Starling equation.

In the cleft, there are two regions, up and downstream of the junction strand, which is approximated as a zero thickness barrier. Since the height of the cleft $2h$ is small compared to both the distance between breaks in the junction strand $2D$, as well as the depths L_1, L_2 of the cleft, the authors claim that water flow in the cleft can be approximated by a Hele-Shaw flow, and was first used in this context by Tsay et al. (1989). The Hele-Shaw flow approximation is for narrow (in the $z-$direction), viscous channel flow in which the flow behaves as an inviscid 2-D flow in the $xy-$plane and nonlinear inertial terms are neglected. Starting from the full Navier-Stokes equations, these assumptions predict that the velocity component in the $z-$direction can be neglected, and also that velocity gradients in the x and y

directions in the viscous terms will be small compared with those in the $z-$direction (Batchelor, 1967). Under the above stated assumptions, the velocity vector is

$$\vec{V} = (u(x, y, z), v(x, y, z), 0)$$

so that the continuity equation can be written as:

$$\frac{\partial u}{\partial x} + \frac{\partial v}{\partial y} = 0 \tag{2.25}$$

The momentum equations reduce to

$$\nabla P = \mu \frac{\partial^2 \vec{V}}{\partial z^2} \tag{2.26}$$

The boundary conditions enforce no slip ($u = v = 0$) at the cleft height $z = \pm h$. Then if $\vec{V_0}(x, y) = (u_0(x, y), v_0(x, y), 0)$ is the velocity at $z = 0$, we have

$$\vec{V} = \vec{V_0}\left(1 - \frac{z^2}{h^2}\right) \tag{2.27}$$

$$\vec{V_0} = -\frac{h^2}{2\mu}\nabla P \tag{2.28}$$

Taking the divergence of (2.28) and substituting for $\nabla \cdot \vec{V_0}$ gives:

$$\frac{\partial^2 P}{\partial x^2} + \frac{\partial^2 P}{\partial y^2} = 0 \tag{2.29}$$

Also, from the components of Eq. (2.28) we obtain the relation

$$\frac{\partial u_0}{\partial y} - \frac{\partial v_0}{\partial x} = 0 \tag{2.30}$$

Now, Equation (2.30) implies that the flow is irrotational in the $xy-$plane, thus the velocity components satisfy a potential flow equation. Equation (2.29) shows that the pressure satisfies a Laplace equation in the $xy-$plane. Therefore, viscous resistance in the Hele-Shaw flow arises from shear stress at the cleft boundaries $z = \pm h$, rather than at vertical boundaries or obstacles in the $xy-$plane. If one were to include additional resistance as a result of cross-bridging molecules or fibers in the wide portion of the cleft, the no slip conditions could not be satisfied on these fibers unless the momentum equation is generalized to include shear stress terms involving second derivatives of u, v with respect to x, y.

At $x = 0$ the pressure and $u-$component of the velocity behind the glycocalyx must equal the pressure and average u value at the cleft entrance. If the velocity

field is integrated over the cleft height, it can be substituted into the modified Starling equation (2.24) to obtain a matching condition

$$P_c - P(0,y) - \sigma_f(\pi_c - \pi(0,y)) = -\frac{h^2 L_f}{3K_p}\frac{\partial P^{(1)}}{\partial x}\bigg|_{x=0^+}$$

where $P^{(1)}$ refers to the pressure in the region of the cleft between the glycocalyx and junction strand. Note that $P(0,y), \pi(0,y), \frac{\partial P^{(1)}}{\partial x}|_{x=0^+}$ are all unknown, and must be found by solving the entire boundary value problem. The other boundary and matching conditions ensure that: (i) the junction strand is impermeable except at its breaks; (ii) pressure and velocity are continuous across the breaks; (iii) the pressure at the cleft exit $x = L_2$ is equal to that in the tissue (P_i); (iv) there is periodicity in the $y-$direction. A point to note regarding (iii) is that the interstitial hydraulic resistance is assumed to be much less than that of the capillary wall, so that the pressure drop across regions B & C is negligible, and the tissue pressure is reached at the cleft exit.

The concentration field is described using different assumptions in each of the four regions. In all cases the steady-state is assumed. In the glycocalyx, or fiber matrix, 1-D convection-diffusion is assumed (in the $x-$direction), where the convection velocity is the average solute velocity. Boundary and matching conditions ensure: (i) concentration at the luminal side of the glycocalyx is the plasma protein concentration C_c; (ii) concentration is continuous at the cleft entrance; (iii) solute flux is continuous at the cleft entrance. Solving the convection-diffusion equation, one obtains another nonlinear coupling condition between $u_0(0,y)$ and $C(0,y)$, which is related to $\pi(0,y)$ using a polynomial relation for concentration and osmotic pressure.

In the cleft, a 2-D convection-diffusion equation averaged over the cleft height must be used, since the gradients in the $x-$ and $y-$directions are of comparable magnitude in the vicinity of the junction strand breaks. Boundary and matching conditions require: (i) the junction strand is impermeable except at its breaks, where the concentration must be continuous; (ii) local solute flux entering the tissue is a prescribed quantity; (iii) periodicity/symmetry in the $y-$direction.

In region B, the cleft exit near field, the following information about the ultrastructure is used in making further assumptions. The average distance of neighbouring clefts is 10 μm, which is much larger than the cleft height, 20 nm, so the solute flux at the cleft exit is treated as a line source of variable strength in the $y-$direction. The governing equation then is a convection-diffusion equation

with radial symmetry, so that $C = C(r, y)$. Boundary and matching conditions require that: (i) the concentration is continuous at the cleft exit; (ii) flux at cleft exit matches that leaving region A; (iii) concentration at the edge of region B may either a) account for vesicular transport or b) match the concentration with region C.

Finally, in the tissue space far field, the fluxes from the breaks in the junction strand as well as from adjacent clefts merge to form a uniform flux. Therefore, a 1-D convection-diffusion equation averaged over the height of the tissue, is used. The boundary conditions are: (i) a prescribed flux at the entrance to the region; (ii) prescribed concentration at the exit (i.e. in the tissue). Regions B and C admit analytic solutions, so only region A must be computed numerically. The authors solve the time-dependent versions of the governing equations, and find the steady-state solutions as the time derivatives approach zero.

To test whether the model was in agreement with the experimental results of Michel and Phillips (1987), Hu and Weinbaum solved the model equations under three conditions: 1) high capillary pressure, 2) low capillary pressure in the steady-state, and 3) low capillary pressure in the transient state. We briefly summarize the results of the three cases.

For a high capillary pressure of 43 cmH_2O, there was filtration as expected. The flow of fluid was zero everywhere except near the breaks in the junction strand. The protein concentration was uniform outside the cleft and varied little within the cleft. For a low capillary pressure of 15 cmH_2O, in the steady-state, the hydrostatic pressure drop from vessel to tissue occurs almost completely across the glycocalyx. However, almost the entire concentration gradient is also experienced across the glycocalyx, with the implication that there is virtually no flow across the glycocalyx along the entire cleft length. This is because the oncotic force is everywhere sufficient to balance the filtration force. The concentration at the cleft exit is much higher than in the previous case, but the gradient within the cleft remains small. At the same capillary pressure in the transient case, we see reabsorption of fluid, as the hydrostatic pressure in the cleft drops to about -7 cmH_2O, creating a negative pressure gradient which sucks fluid from the tissue through the cleft. Recalling the experimental results of Michel and Phillips (1987), this model is able to reproduce the key elements, namely filtration of fluid at high capillary pressure, reabsorption at low capillary pressure in the transient state, and a small but positive filtration at low capillary pressure in the steady-state.

Hu and Weinbaum also investigated the possibility of a parallel, large-pore pathway (e.g. vesicular transport), in which the concentration of proteins in the tissue could be elevated to 40% of that in the capillary. In this case, the pressure and velocity profiles near the entrance to the cleft were almost identical to the case when the entire flux is through the cleft. Also, the protein concentration behind the glycocalyx was virtually unchanged, and in the luminal side of the cleft, the concentration is close to that predicted by the convective limit. However, there were concentration gradients present on the downstream side of the cleft and in the tissue. The concentration behind the glycocalyx is far lower than in the tissue space, and a comparison of the model predictions with the classical Starling equation shows the predicted decrease in filtration as a result. This is precisely the hypothesis of Michel (1997) and Weinbaum (1998), that the local concentration at the 'small-pore' exit (behind the glycocalyx) is lower than the value in the tissue, which reduces the force for filtration. We will come back to this point. In addition, by requiring a fit of their model predictions to the experimental data of Michel and Phillips, the authors are able to make an estimate of the diffusion coefficient in the fiber matrix, D_f, and estimate it to be 3-4 orders of magnitude less than the free diffusion coefficient.

Michel and Phillips, in their 1-D model, assumed that in the steady-state, $C_i = \frac{J_s}{J_v}$, which is appropriate if the solution is well-mixed. Hu and Weinbaum do not require this condition to apply at the cleft exit, but rather require the concentration to first achieve a uniform value at the edge of region B, then allow for further mixing in region C to obtain the condition. In the absence of a large-pore parallel pathway, the tissue space does act like a well-stirred reservoir, and the assumption of Michel and Phillips appears to be valid. However, if the parallel pathway is present, in the convective limit the solute flux through the large-pore pathway is six times greater than that through the cleft, resulting in nonuniformity of region B. The model thus predicts the somewhat surprising result that the concentration in the tissue space may be changed without altering the concentration on the lumen side of the junction strand. Hu and Weinbaum explain this as follows.

At high capillary pressure, the elevation of concentration in the tissue, and on the tissue side of the junction strand, is not communicated upstream through the junction strand breaks. This leaves the region between the glycocalyx and junction strand effectively *insulated from the conditions in the tissue*. Convection dominates over diffusion at the orifice opening, so that the orifice acts "like a throat that prevents the back diffusion of solute into the shielded region in front of the

junction strand" (Hu and Weinbaum, 1999). The result is that the oncotic pressure behind the glycocalyx is uncoupled from that in the tissue. Only at low filtration will the tissue concentration influence that behind the glycocalyx.

The new hypothesis that the glycocalyx acts as the molecular sieve and diffusive barrier to plasma proteins and thus that the Starling forces should be applied locally across the glycocalyx leads to fundamental changes in the classical understanding of the Starling equation. First, the local Starling forces are spatially heterogeneous on the length scale of the spacing between junction strand breaks. Second, the protein concentration and hence osmotic pressure behind the glycocalyx may differ greatly from that in the tissue. The second point emphasizes the new model prediction that filtration is much lower than previously believed in the steady-state. There thus may not be a need for venous reabsorption, and the low lymph flow paradox may be resolved.

2.6.2 Experimental evidence in support of the new view

Hu et al. (2000) tested the hypothesis of Michel and Weinbaum that the effective oncotic force that opposes fluid filtration across the microvessel wall is the local oncotic pressure difference across the glycocalyx. This was a combined experimental and theoretical work, with the experiments performed in frog mesenteric capillaries. In these experiments, filtration and effective oncotic pressure were measured when a) there was no albumin present in the tissue, and b) with the albumin concentration in the tissue maintained at the level of that in the plasma. The latter would ensure diffusion of albumin from tissue toward the vessel. Two sets of experiments were performed: the transient experiments, in which there was a rapid reduction of vessel pressure and measurements taken; and the steady-state experiments, in which the system was allowed to equilibrate after a reduction in pressure. The filtration rates could then be compared to those expected if no oncotic forces opposed filtration (which should be the case in the classical Starling interpretation since the concentration in the vessel and tissue were equal). The theoretical methods were similar to Hu and Weinbaum, except to accomodate albumin in the tissue, the boundary condition was changed to $C_i = C_c$.

In the transient case, filtration fluxes and effective oncotic pressures at both low (10 cmH_2O) and high (43 cmH_2O) capillary pressures did not change whether albumin was present in the tissue or not. Absorption occurred at low p_c when albumin was in the tissue, which one would not expect if diffusion of albumin from the

tissue to the lumen side of the cleft raised the concentration behind the glycocalyx. This led to the conclusion that even though there was no global concentration difference between plasma and tissue, there must be an effective oncotic force being exerted, and it must be exerted by a structure within the capillary wall (namely the glycocalyx).

In the steady-state, with albumin in the tissue, the filtration for high capillary pressures was the same as the transient case. At low p_c there was a small filtration of fluid, however it was only 20% of that expected if there were no oncotic force (i.e. if the classical Starling forces were acting). Therefore, an oncotic force must be acting due to an albumin concentration difference, suggesting a protective mechanism from back diffusion for the downstream side of the filtration barrier. This mechanism is the throat effect of the breaks in the junction strand, which increase fluid velocity sufficiently to prevent (or at least reduce) albumin diffusion toward the glycocalyx. Thus, we have the experimental evidence that fluid balance is indeed determined by concentration differences across the glycocalyx, and maintained by a protected region between the glycocalyx and junction strand.

The study of Adamson et al.

The most definitive evidence in support of the Michel-Weinbaum hypothesis was the study of Adamson et al. (2004), where the hypothesis was first tested in mammalian vessels. In this pioneering study, the effective oncotic pressure difference across rat microvessels perfused with albumin was measured, both with and without the presence of the same albumin concentration in the tissue. The authors carried out detailed reconstructions of the junction strand, determining size and frequency of junction strand breaks, as well as the depth of the strand and mean cleft dimension. Finally, gradients of albumin in the tissue were measured at both high and low filtration rates.

These experiments were combined with a mathematical model, a schematic of which is shown in Figure 2.11. The authors claim that the model differs from that of Hu and Weinbaum in three important respects. First, the work of Squire et al. (2001) found that the glycocalyx is comprised of quasi-periodic bush-like structures of core proteins, with 10-12 nm diameter and 20 nm spacing. These structures are also part of an underlying ordered hexagonal array with central foci spaced at 100 nm intervals. The thickness of the glycocalyx was also measured and found

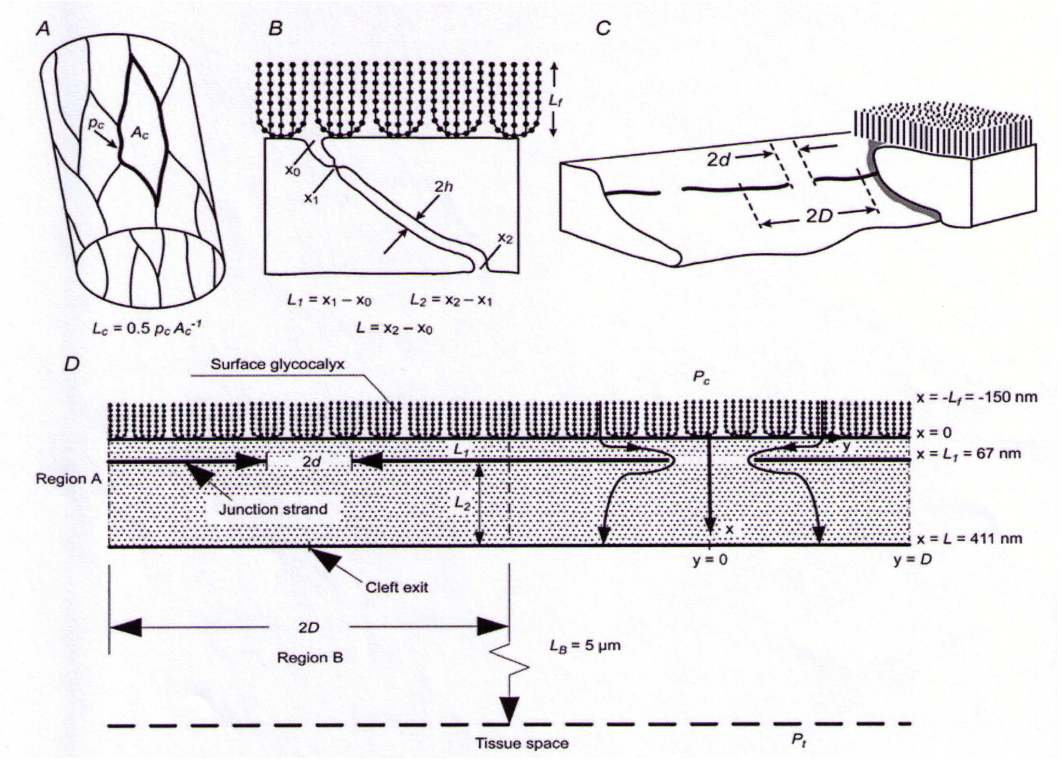

Figure 2.11: The model of Adamson et al. (2004). In (A), the outlined portion is the intercellular cleft between adjacent endothelial cells. (B) and (C) show the three-dimensional geometry of the intercellular clefts along with their breaks and the glycocalyx. (D) is a schematic of their model. Reprinted with permission.

to be approximately 150 nm. Thus, the model of the glycocalyx was modified to fit these observations. A model for the Darcy permeability of the glycocalyx was developed, based on an equal weighting of flow parallel and perpendicular to the core protein fibers, which are modelled as circular cylinders of diameter 12 nm. Second, the morphological observations in their study, as well as those in Schulze and Firth (1992), indicate a periodic array of cleft-spanning structures, possibly cadherins. It is assumed these are spaced in a hexagonal array with 2.5 nm diameter and 15 nm spacing. Thus, flow in the cleft is described using a Brinkman equation (1947). Since the spacing of the cleft-spanning structures is similar to that of the cleft height, the authors suggest that "fiber interaction layers near the cell membrane boundaries must be considered in determining the effective Darcy permeability K_p of the cleft" (Adamson et al., 2004). Then the authors claim that the flow may be treated as a 2-D Darcy flow in which the pressure satisfies a potential equation. We discuss in detail these assumptions and how they relate to models of fluid flow in the cleft in Section 2.7. Third, the location of the tight junction has been moved,

such that it is located closer to the glycocalyx, at only about 15% of the depth of the cleft, in accordance with experimental observations.

The experimental results were as follows. When the tissue was backloaded with albumin, it was found that the albumin concentration near the vessel wall was not significantly changed under conditions of either high or low filtration, meaning that there was no dilution of tissue albumin. The measurements on the morphology of the endothelial cleft gave estimates of many parameters used in the mathematical model, namely the gap length, mean gap spacing, perimeter per unit area of endothelial cells, mean depth of the strand breaks, and mean depth of the cleft path from lumen to interstitium.

With no albumin in the tissue, the intercept on the $\frac{J_v}{A}$ vs. p_c curve was 24 $\mathrm{cmH_2O}$, which was the effective oncotic pressure. With albumin present in the tissue at the same concentration as in the vessel, such that according to the classical Starling view there would be no oncotic force and the intercept of the curve should be the origin, the effective oncotic pressure was found to be 17 $\mathrm{cmH_2O}$. Due to the observation above that tissue gradients were not present, the authors conclude that "the colloid osmotic force opposing filtration must have been exerted across a structure within the microvessel wall, which we propose to be the glycocalyx" (Adamson et al., 2004).

The mathematical model was used to quantify some observations. When L_P was plotted as a function of glycocalyx thickness with and without cleft-spanning structures, it was found that the presence of the structures decreased the value of L_P by approximately one half. They conclude based on the predicted values that the cleft-spanning structures are likely present, and for a glycocalyx thickness of 150 nm, they find $L_P = 1.24 \times 10^{-7}$ cm $\mathrm{s^{-1}}$ $\mathrm{cmH_2O^{-1}}$. When tissue albumin was present, at high capillary pressures the predicted concentration on the lumen side of the junction strand was only 35% of that in the lumen and tissue. At medium p_c, the concentration outside the cleft is reduced by only 10% from that in the tissue, but in the protected region behind the glycocalyx, the concentration is reduced by about 40%. Thus in both cases, the effective oncotic pressure difference across the glycocalyx is much greater than between lumen and tissue. The predicted $\frac{J_v}{A}$ vs. p_c curves lie between the classical Starling prediction and the case if there were no albumin in the tissue, as in Michel and Phillips' experiments. They provide good agreement with experimental data where the measured L_P was close to that predicted by the mathematical model, over a significant variation of the reflection coefficient and cleft diffusion coefficient.

Their results conform to the hypothesis that the hydrostatic and osmotic pressure differences across the glycocalyx determine fluid filtration. Therefore, tissue protein concentration contributes less to the balance of forces, as is seen by the fact that even when the luminal and tissue concentrations were equal, large osmotic forces were still present across the wall. The most important observation was that under high or low filtration conditions, there was no measurable difference in albumin concentration near the vessel wall, in other words filtration does not dilute the tissue albumin concentration and hence does not affect the osmotic pressure. The reason for this is that as fluid spreads into the tissue, the velocity falls off markedly, and thus diffusive mechanisms dominate. The presence of the small breaks in the junction strand causes water to be funneled through the breaks such that diffusion of albumin from tissue to the cleft cannot overcome the convective flow in this region. Thus, a low albumin concentration is maintained in the protected region between the glycocalyx and junction strand.

The new view of Starling's hypothesis is thus summarized as follows. In the classical Starling equation, it is the term $\sigma(\pi_c - \pi_i)$ that determines fluid flux, whereas in the current model π_i is replaced by π_g. Since π_g is kept lower than π_i by the mechanisms described above, the term $\sigma(\pi_c - \pi_g)$ is always greater than $\sigma(\pi_c - \pi_i)$, thus the force for filtration, and hence $\frac{J_v}{A}$, is reduced. A larger flux will further reduce π_g, due to a larger convective flow opposing diffusion from tissue into the protected region. The authors estimate π_g in the range 0.7-0.9π_i under normal physiological conditions.

An additional consequence of this new view is that if the protein concentration difference across the glycocalyx, rather than between lumen and tissue, is the determinant of fluid exchange, then the low lymph flow paradox is resolved.

2.6.3 A simplified one-dimensional model

Zhang et al. (2006a) pointed out that the three-dimensional model of Hu and Weinbaum (1999) has drawbacks, namely that it is too complicated for convenient use, there is a considerable computational cost, and a lack of numerical convergence when there are small concentration gradients in the tissue. To overcome these difficulties, they formulated a simpler 1-D model in which each of five regions is described by a convection-diffusion equation, which reduces the system to a set of algebraic equations that can be solved analytically. A schematic is shown in Figure 2.12.

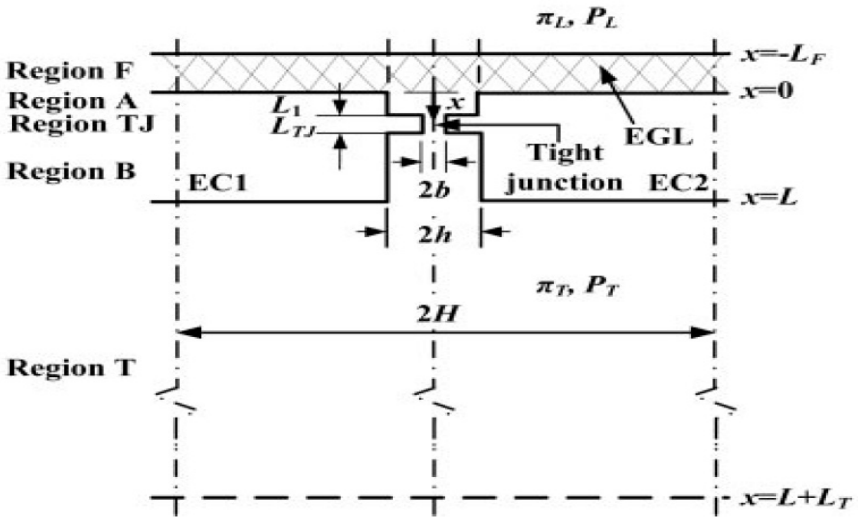

Figure 2.12: The model of Zhang et al. (2006a).

The major differences with the Hu and Weinbaum and Adamson et al. models are as follows: first, "[t]he key simplification is the conversion of the TJ strand with its periodic orifices to a single, continuous slit, which provides the same transport area for solutes as the orifice-like breaks and whose resistance to both water and solute is adjusted to provide the same L_P and P_d as in the 3-D model" (Zhang et al., 2006a). Note that P_d represents the solute permeability and TJ refers to tight junction. Instead of a zero thickness barrier as treated in the 3-D model, the TJ now has a finite depth, and the average velocity in the slit is taken to be the same as in the breaks of the 3-D model. The second difference in the model is that the tissue space is now treated as a single region, rather than allowing for a mixing region and far-field.

To satisfy the condition that the area for albumin diffusion is preserved, it is found that $2b$, the height of the slit, is 1.58 nm, and L_{TJ}, the tight junction depth, is 1.49 nm. It is noted that such a small channel would not permit passage of an albumin molecule (diameter 7 nm), but the actual break in the junction strand is 18 nm high by 315 nm wide, and the "...narrow continuous TJ slit is an artificial construct that preserves the TJ area for albumin diffusion" (Zhang et al., 2006a).

In going from a 3-D model to a 1-D model, the hydraulic resistance of the glycocalyx must be examined in detail. The glycocalyx resistance actually has two components: an intrinsic resistance due to water flow through the matrix, and the ability to change the fluid streamline patterns in the cleft. With the glycocalyx present, water is shunted to the side and passes through the channel between the

back of the glycocalyx and TJ strand. The streamlines will thus have a more broad, orifice-like distribution converging on the TJ strand breaks, and this streamline shift is responsible for most of the glycocalyx resistance to flow. The authors take this into account by adding an additional resistance at the back of the glycocalyx. Also, diffusional resistance must be accounted for, and thus it is required that in the pure diffusion limit, this quantity must be equal in the 3-D and 1-D models.

As mentioned, each region was treated by a 1-D convection-diffusion equation, with boundary and matching conditions such that the albumin concentration and flux per unit cleft length are continuous. The authors model three experimental conditions: 1) Michel and Phillips' model where $C_i = \frac{J_s}{J_v}$, 2) Adamson et al. model, where either $C_i = C_c$ or $C_i = 0.4C_c$, and 3) transcellular vesicular fluxes of solute are added in parallel to examine the tissue concentration and effect of back diffusion. Note that in the first two conditions, all water and solute pass through the cleft.

With $C_i = \frac{J_s}{J_v}$ (as in Michel and Phillips) and all fluxes passing through the cleft, the $\frac{J_v}{A}$ vs. p_c curves predicted by the 1-D model are in very good agreement with both the Michel and Phillips model and the 3-D model prediction. When the tissue concentration is elevated to that of the lumen, as in Adamson et al., the 1-D model is very close to the 3-D model and agrees reasonably well with the experimental data of Adamson et al. (2004). When the interstitial albumin concentration is clamped at 20 mg/ml (to represent $C_i = 0.4C_c$, which is the case in many tissues) at a distance of 100 μm from the vessel, it is found that there is steady-state reabsorption for lumen pressures of approximately 17 cmH_2O or lower. This occurs when diffusional gradients of albumin in the cleft behind the glycocalyx are stronger than the tendency of albumin to be carried to the back of the glycocalyx by convective flow during reabsorption. This is a surprising prediction of the model, but has yet to be verified experimentally.

2.7 Overview

The field of transcapillary exchange began with Starling's seminal work in which he showed that fluid could be absorbed directly from the tissue into the blood, and hypothesized that the forces determining fluid balance were the hydrostatic and osmotic pressures. The experimental work of Landis, as well as Pappenheimer and Soto-Rivera, measured the filtration flux through the capillary wall as a function of capillary pressure, and found a linear relationship with intercept on the p_c-axis close

to the osmotic pressure difference between the capillary and tissue, thus confirming Starling's hypothesis. They each wrote down a simple relation for the filtration flux in terms of capillary pressure and effective osmotic pressure (or isogravimetric pressure), which would come to be known as the Starling equation.

Using nonequilibrium thermodynamic arguments to describe transport of fluid and solutes across semipermeable membranes, one may write down phenomenological equations which, by envisioning the capillary wall as a semipermeable membrane, gives exactly the Starling equation. To describe the nature of this 'membrane', Pore Theory and the Fiber Matrix Model were developed. The former could not explain experimental results, however the latter was completely consistent with the hydraulic conductivity, permeability, and reflection coefficient data. Thus, the prevailing view was that there was a matrix with a random array of cylindrical fibers that acted as the semipermeable membrane that was the capillary wall.

However, the theoretically predicted result that there could be no steady state reabsorption, first observed experimentally in Michel and Phillips (1987), seemed to contradict the Starling equation, and thus investigators searched for a mechanism to explain this. Michel (1997) and Weinbaum (1998) hypothesized that the endothelial glycocalyx was the molecular sieve to plasma proteins, and thus that the Starling equation should be applied locally across the glycocalyx rather than globally between capillary and interstitial space. In this new view, the details of which are given in the model of Hu and Weinbaum (1999), the glycocalyx is the fiber matrix from the theory of Curry and Michel (1980). They found that the local protein concentration at the cleft exit may be much less than that in the tissue, thus reducing the forces for filtration. Not only does their theory predict that there can be no reabsorption in the steady state, but it also resolves the low lymph paradox.

Experimental confirmation of the Michel-Weinbaum hypothesis in mammalian vessels was made by Adamson et al. (2004). In this important study, the investigators performed experiments in which the effective osmotic pressure was determined with and without albumin in the tissue, tissue gradients of albumin were measured at both high and low flow rates, and the parameters describing the cleft and junction strand were measured. The experimental results were used in combination with a modification of the theory of Hu and Weinbaum (1999). Later, Zhang et al. (2006a) formulated a one-dimensional model, which was simpler and permitted an analytical solution, to overcome the shortcomings of the other models. We close this chapter with a discussion of the key assumptions made in each of the mathematical models of Hu and Weinbaum (1999), Adamson et al. (2004), and Zhang

et al. (2006a).

The formulation of a mathematical model requires selection of governing equations, which usually are derived from mass and momentum balance, and the prescription of appropriate boundary conditions. Unfortunately, in the complex problem of transcapillary exchange, neither the equations of motion nor the boundary conditions are straightforward. Each of the three models assumes the new view of Starling's hypothesis, namely that the glycocalyx acts as a fiber matrix on the luminal side of the capillary wall. Thus, the average velocity of the fluid just behind the glycocalyx is proportional to the difference between the hydrostatic and osmotic pressures across the glycocalyx. In the model of Zhang et al., it is pointed out that part of the resistance of the glycocalyx is due to its ability to bend the streamlines of the flow. This cannot be described by a 1-D model, so the authors add a resistance to obtain agreement with Hu and Weinbaum. Adamson et al. state that they develop a model for the Darcy permeability of the glycocalyx based on equal weighting of flow parallel and perpendicular to the core protein fibers. Unfortunately, the model equations are not given in their paper, making it difficult to understand whether they are assuming a 2-D flow, or simply that the presence of perpendicular flow changes the apparent permeability of the glycocalyx. We will assume the latter. For the concentration field, both Hu and Weinbaum and Zhang et al. use a 1-D convection-diffusion equation for the albumin concentration in the glycocalyx, where the convection velocity is the average solute velocity. In Adamson et al., this depends on the above; if they assume 1-D flow, then it is the same, but if it is a 2-D flow, then the convection velocity would have to be a vector, and hence the proper model would be convection-diffusion in 2-D. Although there may be slight discrepancies, the three models generally agree on how to describe transport in the glycocalyx.

The flow of fluid and solutes through the endothelial cleft, however, is treated differently, and this is the distinguishing feature of each model. Hu and Weinbaum assume a Hele-Shaw flow, which as described earlier represents flow between two parallel plates, usually around an obstacle where the length scale of the obstacle is much greater than that of the separation of the plates. The authors use this assumption based on the rigorous hydrodynamic theory of Zeng and Weinbaum (1994) which looked at the flow through a thin planar barrier with periodically spaced orifices. An analysis is performed which identifies the dimensionless quantities relating three parameters, namely the cleft height, orifice width, and distance between orifices. For the experimentally measured values as in Adamson and Michel

(1993), the full 3-D Stokes flow is well approximated by Hele-Shaw flow. The result of this assumption is that the flow is essentially a 2-D potential flow in each cross-section parallel to the plates (which are the cleft boundaries), with a no-slip condition on the plates, such that the velocity is a maximum at the plane of half-width, and drops off in a parabolic profile. The viscous resistance of this model then arises as a result of the shear stress at the cleft boundaries, rather than the obstacles in the xy-plane.

Adamson et al. point out that there is a hexagonal array of cleft-spanning structures which will add to the resistance of the cleft, and thus describe the flow using a Brinkman equation, in accordance with Tsay and Weinbaum (1991). The Brinkman (1947) equation was postulated to describe flow through a porous medium where instead of the pressure gradient being proportional to the velocity, as in Darcy's law, the equation also contains a term with the Laplacian of velocity. The result is that in the limit of low permeability, the Brinkman equation reduces to Darcy's law, and in the limit of high permeability (or negligible resistance due to the porous medium), it is approximated by Stokes flow.

An explanation of the study of Tsay and Weinbaum (1991), in which the viscous flow past a square array of circular cylindrical fibers confined between parallel walls was studied using the 3-D Stokes equations, is helpful. A key dimensionless parameter is the aspect ratio, $B = \frac{B'}{a}$, where B' is the half-spacing between the walls and a is the cylinder radius. When $B \ll 1$, Hele-Shaw flow is a good approximation, whereas the Brinkman approximation works well for $B > 5$. We can think of the $B \ll 1$ limit as short, wide cylinders, and the $B \gg 1$ limit as long, slender cylinders. Recall that for Hele-Shaw flow, we were concerned with flow around an obstacle, whereas now we are looking at an array of cylinders. It was found in this study that the important parameter that characterises flow is $\frac{\Delta}{B}$, where Δ is the spacing between fibers. Thus, it is the relative magnitudes of the spacing and the aspect ratio that determines the flow regime. This is due to the fact that the viscous boundary layer on a particular cylinder is of the order of B. Therefore, in the limit of $\frac{\Delta}{B} \gg 1$, the flow can be approximated by a Hele-Shaw flow, noting that the requirement that $B \ll 1$ from above is no longer required. The viscous boundary layers from adjacent cylinders will not come close to meeting in this case, and thus we are essentially in the potential flow regime. When $\frac{\Delta}{B} \ll 1$, the viscous boundary layers overlap one another, thus increasing the drag force by a large amount for decreasing values of $\frac{\Delta}{B} \leq O(1)$. Then the equations can be approximated by the 2-D version, due to the fact that the effect of the viscous overlapping regions in

each plane will be much greater than the effect of the parallel plates. Adamson et al. measured the spacing of the cleft-spanning structures and found they are of the same order as the cleft height, and so neither of the limits of $\frac{\Delta}{B}$ is applicable, but rather the boundary layers near the cell membrane must be taken into account.

In reality, the flow through the cleft is a flow between parallel plates with periodic orifices, in which the flow can be treated as Hele-Shaw, in combination with flow around thin obstacles with spacing of the same order as the spacing, which is treated by a 3-D Brinkman equation. So, the manner in which these flows are combined, and the simplifying assumptions that can be made, are not obvious. The authors claim that once they have determined the *effective Darcy permeability*, then "the governing equation for the flow in the cleft can be treated as a two-dimensional Darcy flow satisfying a potential equation for the pressure field" (Adamson et al., 2004). Again, the failure to explicitly write down the equations and boundary conditions of their model is a cause of confusion for the reader.

Since the model of Zhang et al. is one-dimensional, the only possibility for fluid flow through the cleft is a flow with constant velocity, in accordance with the continuity equation. However, to mimic the effect of the orifices in the junction strand, instead of treating the junction strand as a zero-thickness barrier as above, they convert it to a tiny channel with finite depth. This channel is an "artificial construct" (Zhang et al., 2006a) in which the resistance of the channel is adjusted so that the hydraulic conductivity and permeability match the 3-D model of Hu and Weinbaum. However, at the cost of introducing an artificial construct, the authors were able to solve the equations of their model analytically.

We briefly mention the manner in which the tissue space is treated in the different models, although the effects are much less than those of different assumptions for the flow in the cleft. In Hu and Weinbaum, there is a mixing region outside the cleft, which is treated as a line source of solute, and a far-field, where the flux of solute is required to become uniform. Adamson et al. instead solve 3-D convection-diffusion equations with boundary conditions of continuity of concentration and flux at the cleft exit and tissue far-field. Zhang et al. treat the tissue space as only one region, since there are no discrete orifices through which fluid flows, and thus no need for a mixing region.

Therefore, the models have points of agreement and disagreement. The motivating purpose for the theoretical model developed in this Thesis, as already published in Speziale et al. (2008), is similar to that of Zhang et al. (2006a), namely to formu-

late a theory that is simpler from a mathematical perspective, yet which does not lose too much of the predictive power of the more complicated ultrastructural models. Since the Michel-Weinbaum hypothesis for flow across the glycocalyx seems to have a solid experimental basis and has become the generally accepted view, we use this assumption in our formulation.

Where we depart from the above models, however, is in the treatment of flow through the cleft. We generally will refer to the capillary wall as meaning the endothelial cells and the intercellular clefts with junction strands and their periodic orifices. Due to the lack of agreement in treating the flow mentioned above, we take a different approach, namely homogenization of the capillary wall, such that the theory of poroelasticity may be used. In this case, only one paramter is required to describe the resistance to flow through the wall, and this is equivalent to the *effective Darcy permeability* in Adamson et al. (2004). Although the effect of homogenization is to 'wipe out' the microstructure, clearly a large simplification, the trade-off for obtaining an analytically solvable model is reasonable under some circumstances, and we discuss the validity of our assumptions in the next chapter. We now present our poroelastic model of transcapillary flow.

Chapter 3

A poroelastic model of transcapillary flow

3.1 Introduction

For the reasons outlined at the end of the previous chapter, it is essential to develop a more accessible model of transcapillary exchange that does not lose the predictive capabilities of the more complicated ultrastructural models. To accomplish this, we take advantage of the fact that flow through the capillary wall with its detailed ultrastructure, including endothelial clefts, tight junctions, and orifices, may be thought of as a flow through a porous medium. The study of porous media flows arose initially in the study of soil mechanics, and Biot (1941) developed the theory of consolidation to describe the settlement of soils under an applied load. The grains composing the elastic soil skeleton are imagined to be held together by certain forces, such that the behaviour of the soil is similar to that of squeezing a sponge saturated with water. Under the assumptions of the theory, the porous medium is an isotropic, homogeneous material, with both the fluid and solid phases coexisting at each point. In this sense, the ultrastructure of the porous medium, for instance the pore size, spacing and geometry, is 'smeared' out and the individual effects of single pores are averaged to obtain macroscopic equations (Burridge and Keller, 1981).

The fact that biological tissues are porous and elastic led to the application of consolidation theory, or poroelasticity, to problems in various areas of physiology, for example flow through articular cartilage (Mow et al., 1980), flow through aortic

tissue (Kenyon, 1979), and biomechanics of the brain (Nagashima et al., 1987; Tenti et al., 1999, 2000). These successful applications of the theory lead us to believe that the problem herein, namely flow through the capillary wall, may be treated using this same approach. We therefore model the capillary wall as a poroelastic material, consisting of a fluid and a solid phase, both of which are intrinsically incompressible. In our application, this amounts to replacing the ultrastructure of the capillary wall (the cleft, its tight junctions and orifices) by an idealized homogeneous system. The result is that we will not be able to describe for instance the fluid streamlines through the breaks in the junction strand, as done in Hu and Weinbaum (1999). The advantage though is that there is no need to account for the extremely complicated geometrical configuration of the capillary wall structures, and we thus obtain a relatively simple mathematical model, as well as simple geometry. Additionally, we are able to solve the model equations analytically and write closed form solutions for all variables.

Our model, however, must deviate from classical poroelastic models, due to the following. An assumption of poroelasticity is that the fluid flux through the porous matrix is proportional to the pressure gradient, which is known as Darcy's law. In the presence of solutes, however, it is well-known that low-permeable clay sediments may exhibit membrane behaviour, and over the last several decades mounting evidence has shown that clay can restrict solute transport relative to the flow of water (Bader and Kooi, 2005, and references therein). Consequently, the presence of clay gives rise to both ultrafiltration and chemical osmosis (Section 2.4.3) with the result that Darcy's law is no longer valid.

Here, we make an analogy between flow through clays and the capillary wall, since the capillary wall is also known to restrict the transport of albumin relative to water (for example, Hu and Weinbaum (1999) assume a non-zero reflection coefficient due to crossbridging structures in the wide part of the cleft). Thus, we envisage the capillary wall as a homogeneous and isotropic material at each point of which both the fluid and solid phases coexist (Biot's assumption), but with the addition of a variable concentration of plasma proteins responsible for the osmotic pressure gradient. On the lumen side of the wall we assume the Michel-Weinbaum hypothesis applies, that is that the endothelial surface glycocalyx is the primary molecular sieve for plasma proteins (namely albumin), and hence the Starling forces act across the glycocalyx rather than between the lumen and tissue. The varying concentration of albumin across the wall, which we assume to vary continuously, sets up the colloid osmotic pressure gradient. We assume that in the pericapillary

interstitium just outside the wall, the concentration of albumin equals that in the tissue.

The contents of this chapter have for the most part already appeared in the literature (Speziale et al., 2008). Note, however, that some of the ideas from that manuscript are elaborated upon, especially in the Discussion.

3.2 Mathematical model

We idealize a typical capillary in a normal tissue as a uniform circular cylinder with a diameter of 10 μm and a porous wall of 0.5 μm thickness. As explained in the Introduction, we assume that the wall consists of a homogenized medium such that at each point the solid and fluid phases coexist, and within the fluid phase there is a solute which is representative of plasma proteins (e.g. albumin). We also make the assumption that the capillary hydrostatic pressure p_c and the plasma protein osmotic pressure π_c are constant throughout the cylindrical section of the capillary of interest here, so that the strain in the tube wall can be taken to be planar. This allows us to examine a cross-section of capillary, and work in two dimensions. In addition, we limit this analysis to the steady state case.

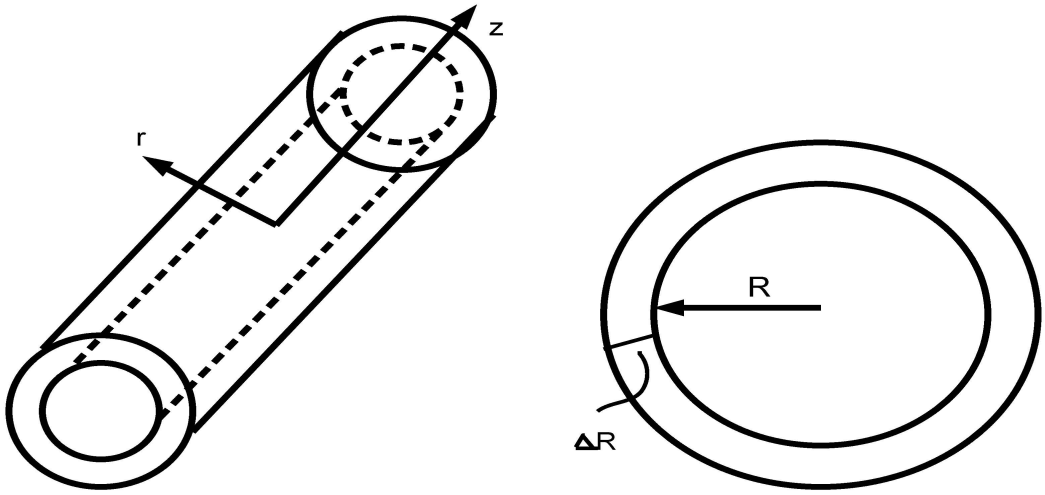

Figure 3.1: Model geometry. On the left side is the coordinate system. On the right side is our domain – the annulus $R \leq r \leq R + \Delta R$.

It is convenient to write Biot's consolidation equations in the notation introduced by Kenyon (1976a). Due to the extreme smallness of the Reynolds number, we can neglect the inertia terms in the equation of motion which therefore reduces to the equilibrium condition

$$\frac{\partial}{\partial x_j} T_{ij} = 0, \quad (i, j = 1, 2, 3) \tag{3.1}$$

Here and in the rest of this work the summation convention over repeated indices is used. The triplet (x_1, x_2, x_3) stands for a standard Cartesian coordinate system with origin on the axis of the capillary, which also plays the role of the z-axis. T_{ij} is the total stress tensor, so that the equilibrium condition implies that the total stress is divergenceless. Now, in the classical consolidation theory the total stress is written as

$$T_{ij} = -p\delta_{ij} + \tau_{ij} \tag{3.2}$$

where p is interpreted as the pore fluid pressure, which acts only on the diagonal elements of T_{ij} due to δ_{ij}, the Kronecker delta, while τ_{ij} depends on the bulk deformation of the solid matrix only and is interpreted as a contact stress (Kenyon, 1976b). In our case, however, there is also a contribution to the normal stresses coming from the presence of osmotic pressure, with the consequence that Eq. (3.2) has to be modified.

3.2.1 Osmotic pressure in consolidation theory

As outlined in the Introduction, our hypothesis is that the structure of the capillary wall can restrict solute transport relative to the bulk fluid flow, thus exhibiting membrane behaviour. Assuming for simplicity that there is only one solute - namely albumin - and that the solvent is water, it follows that throughout the capillary wall there will be a smoothly varying concentration of solute $c_s(x_1, x_2, x_3)$ and hence a smoothly varying osmotic pressure $\pi(x_1, x_2, x_3)$. Following the discussion in Section 2.4.3, nonequilibrium thermodynamic arguments allow us to express the volume and diffusional fluxes in terms of the corresponding thermodynamic forces, which in the case of a semipermeable membrane are the differences in hydrostatic and osmotic pressures. Patlak et al. (1963) extended this formulation to differential forms in one dimension, and we assume that this holds in higher dimensions as well, so that we can express the fluxes in terms of ∇p and $\nabla \pi$. The result is the pair of

coupled phenomenological equations

$$\vec{J_v} = L_P \nabla(-p) + L_{PD} \nabla(-\pi) \tag{3.3a}$$

$$\vec{J_D} = L_{DP} \nabla(-p) + L_D \nabla(-\pi) \tag{3.3b}$$

where, as mentioned above, the cross coefficients, L_{PD} and L_{DP}, are equal by Onsager's principle and provide the coupling between osmosis and ultrafiltration. We also mention that the coefficients refer to the capillary wall region only, not the entire flow across the glycocalyx and through the capillary wall. Later in this chapter and in the next one, we discuss in detail the hydraulic conductivity, which will also be denoted L_P. This quantity is something entirely different, namely the slope of the line relating the filtration flux to the capillary pressure. It is hoped that this does not cause the reader too much confusion, but we wish to be consistent with the notation in the literature. Now, if we recall the reflection coefficient $\sigma = -\dfrac{L_{PD}}{L_P}$, we may rewrite Eq. (3.3a) as

$$\vec{J_v} = -L_P(\nabla p - \sigma \nabla \pi) \tag{3.4}$$

The physical meaning of this equation is obvious, namely that the velocity $\vec{J_v}$ is the result of the net balance between the hydraulic and the osmotic gradients which act in opposite directions. Furthermore, for $\sigma = 1$ the osmotic contribution is largest and corresponds to the effect of an ideal semipermeable membrane function, in that all of the solute is 'reflected'. At the other extreme – that is, when $\sigma = 0$ – both the solvent and the solute can flow freely in response to the hydraulic pressure gradient alone. This latter case should coincide with Darcy's law of classical consolidation theory, and this conclusion is reinforced by the fact that the transport coefficient L_P in Eq. (3.4) has the same physical dimensions, namely L^3TM^{-1}, as the Darcy coefficient $\frac{k}{\mu}$, where k is the permeability of the medium and μ the dynamical viscosity. It follows that under the assumption that L_P is a constant property of the homogenized system we can regard the phenomenological equation (3.4) as a kind of generalized Darcy law, and rewrite it as

$$\vec{W} = -\frac{k}{\mu}(\nabla p - \sigma \nabla \pi) \tag{3.5}$$

where we call $\vec{W}$ the filtration velocity. The latter is usually called the specific discharge in the theory of water and solute transport in clayey soils where the same equation is used (Bader and Kooi, 2005). Introduction of a new quantity called the effective pressure, P, defined as

$$P = p - \sigma \pi \tag{3.6}$$

allows us to rewrite Eq. (3.5) as

$$\vec{W} = -\frac{k}{\mu}\nabla P \tag{3.7}$$

It is of note here that p, π and P are functions of space, whereas the reflection coefficient σ is regarded as a constant. If an osmotic force drives the flow, then similar to hydrostatic forces, it also affects the total stress. Thus, the constitutive equations (3.2) must read

$$T_{ij} = -P\delta_{ij} + \tau_{ij} \tag{3.8}$$

where the contact stress tensor has a form similar to that of linear elasticity theory, namely

$$\tau_{ij} = \lambda e_{kk}\delta_{ij} + 2Ge_{ij} \tag{3.9}$$

except that the constants λ and G are the Lamé-like parameters for the mixture. The strain tensor e_{ij} is defined in terms of the displacement vector $\vec{u}$ by the linear approximation

$$e_{ij} = \frac{1}{2}\left(\frac{\partial u_i}{\partial x_j} + \frac{\partial u_j}{\partial x_i}\right) \tag{3.10}$$

and hence we have $e_{kk} = \dfrac{\partial u_k}{\partial x_k}$. We will denote this quantity e, the cubic dilatation, or local change in volume, and summation over repeated indices gives

$$e = \nabla \cdot \vec{u} \tag{3.11}$$

Since in the steady state the velocity $\dfrac{\partial \vec{u}}{\partial t}$ of the solid component vanishes, the continuity equation for the mixture reduces to the incompressibility condition for the bulk liquid, namely

$$\nabla \cdot \vec{W} = 0 \tag{3.12}$$

For $\sigma = 0$ these are the standard equations of linear poroelasticity. For $\sigma > 0$, however, the system is not closed because the osmotic pressure π is a further unknown. Hence our next task is to derive the missing equation.

Spatial evolution of osmotic pressure

The relationship between the solute concentration c_s and the corresponding osmotic pressure is linear only for ideal, dilute solutions (van't Hoff law), while for higher

concentrations higher-degree polynomials in c_s have been derived by fitting experimental data (Michel, 1984). For instance, Hu and Weinbaum (1999) have used the formula (π in cmH_2O and c_s in grams per litre)

$$\pi = 0.345c_s + 2.657 \times 10^{-3}{c_s}^2 + 2.26 \times 10^{-5}{c_s}^3 \tag{3.13}$$

which was determined by a curve fit of experimental data given by McDonald and Levick (1993). Then, of course, one needs to add to the theory a convection-diffusion equation for c_s, which in turn requires knowledge of the convection velocity from hydrodynamics. Each of these steps involves approximating assumptions in order to make the complexity of the mathematical equations manageable.

In this work, however, we take a different approach. We first note that at the physiological concentration of 22.5 gl^{-1} of albumin (McDonald and Levick, 1993) the linear term is only 17% off the full value. Secondly, we show below that if only the linear term is kept then we can derive a single differential equation for the osmotic pressure, thus bypassing the problem of calculating c_s with its attendant uncertainties. Consequently, we hypothesize this trade-off to be reasonable in our case and proceed to the derivation of such an equation from nonequilibrium thermodynamics. Eliminating ∇p from the fundamental equations (3.3a)-(3.3b) and using the Onsager relation $L_{PD} = L_{DP}$ gives

$$-\vec{J_D} = \sigma\vec{J_v} + (L_{PD}\sigma + L_D)\nabla\pi \tag{3.14}$$

Following the argument in Section 2.4.3, it is convenient to rewrite this equation in terms of the total solute flux $\vec{J_s}$, which is given by $\vec{J_s} = c_s(\vec{J_v} + \vec{J_d})$ in the dilute case where the solute volume fraction is much less than one. Thanks to this relation, the relative velocity $\vec{J_D}$ can be eliminated from (3.14) which then reads

$$\vec{J_s} = c_s(1-\sigma)\vec{J_v} + c_s(L_P\sigma^2 - L_D)\nabla\pi \tag{3.15}$$

and use of the van't Hoff law allows us to eliminate the solute concentration c_s in favour of $\pi = c_sRT$, where R is the perfect gas constant and T is the absolute temperature (also constant). Then Eq. (3.15) becomes

$$RT\vec{J_s} = (1-\sigma)\pi\vec{J_v} + (L_P\sigma^2 - L_D)\pi\nabla\pi \tag{3.16}$$

and since $\vec{J_s}$ is a divergenceless vector field - as it follows from the continuity equation and the steady-state assumption - the condition $\nabla \cdot \vec{J_s} = 0$ leads to the following differential equation for π,

$$\pi\nabla^2\pi + \left(\frac{1-\sigma}{L_P\sigma^2 - L_D}\right)\vec{W}\cdot\nabla\pi + |\nabla\pi|^2 = 0 \tag{3.17}$$

where we have used the information that $\vec{J}_v$ is just the filtration velocity $\vec{W}$ of poroelastic theory.

3.2.2 Solution of the transport problem

The assumption of a cylindrical capillary allows us to simplify considerably the mathematical model by taking advantage of this symmetry and rephrasing all equations in cylindrical coordinates (r, θ, z), where z coincides with the capillary axis, θ is the longitudinal angle, and r is the radial distance from the axis. The further assumption of plane strain implies that all fields are independent of z, which amounts to saying that the dynamics are the same in every cross-section of the cylinder. Then, taking into account the fact that the thermodynamic forces act perpendicularly to the capillary wall, we can conclude that all fields are functions of the radial coordinate alone in the steady state case. Our domain then is the annulus $R \leq r \leq R + \Delta R$, where R is the radius of the capillary, and ΔR is the thickness of the capillary wall.

In this coordinate system the transport problem consists of Eqs. (3.6),(3.7),(3.12) and (3.17). The first three now read

$$W(r) = -\frac{k}{\mu}\frac{dP}{dr} \tag{3.18}$$

$$P(r) = p(r) - \sigma\pi(r) \tag{3.19}$$

$$\frac{1}{r}\frac{d}{dr}\left(rW(r)\right) = 0 \tag{3.20}$$

along with the boundary conditions

$$W(R) = \frac{k_g}{\mu\ell_g}[p_c - p_g - \sigma_g(\pi_c - \pi_g)] \tag{3.21}$$

$$\begin{aligned} P(R + \Delta R) &= p(R + \Delta R) - \sigma\pi(R + \Delta R) \\ &= p_i - \sigma\pi_i \end{aligned} \tag{3.22}$$

The subscript c refers to the lumen side (capillary) and g to the cleft side of the endothelial surface glycocalyx, whose 'bush' structure has thickness ℓ_g and permeability k_g (Hu and Weinbaum, 1999; Adamson et al., 2004). The first boundary condition enforces the Michel-Weinbaum hypothesis regarding the revised Starling principle. It is noted here that p_g and π_g are simply the hydrostatic and osmotic

pressures just behind the glycocalyx at the inner wall, and therefore $p_g = p(R)$ and $\pi_g = \pi(R)$. This equation therefore provides a coupling between the filtration velocity, hydrostatic pressure and osmotic pressure at the inner wall. The second condition simply requires the effective pressure to match the value at the pericapillary part of the interstitium (denoted by the subscript i). The equation for the osmotic pressure becomes

$$\frac{\pi}{r}\frac{d}{dr}\left(r\frac{d\pi}{dr}\right) - \left(\frac{1-\sigma}{L_D - \sigma^2 L_p}\right)\frac{d\pi}{dr}W(r) + \left(\frac{d\pi}{dr}\right)^2 = 0 \tag{3.23}$$

with the boundary conditions

$$\pi(R) = \pi_g \tag{3.24a}$$

$$\pi(R + \Delta R) = \pi_i \tag{3.24b}$$

which simply impose continuity at the interval's endpoints.

The solution of (3.20) is easily found to be

$$W(r) = \frac{c_1}{r} \tag{3.25}$$

where using the boundary condition (3.21) we can evaluate the constant c_1 as

$$c_1 = \frac{k_g R}{\mu \ell_g}[(p_c - p_g) - \sigma_g(\pi_c - \pi_g)] \tag{3.26}$$

Integrating (3.18) gives

$$P(r) = p_i - \sigma\pi_i + \frac{\mu}{k}c_1 \ln\left(\frac{R + \Delta R}{r}\right) \tag{3.27}$$

If we substitute in $r = R$ into this expression, and also realize that by the definition of P, $P(R) = p_g - \sigma\pi_g$, we obtain a matching condition

$$p_g - \sigma\pi_g = p_i - \sigma\pi_i + \frac{\mu}{k}c_1 \ln(1 + h) \tag{3.28}$$

where $h = \frac{\Delta R}{R}$ and which, noting that the expression for c_1 contains p_g, can be solved for p_g in terms of the other parameters

$$p_g = \frac{\Delta p_{ig} + \frac{\gamma}{\ell_g}\Delta p_{cg}}{1 + \frac{\gamma}{\ell_g}} \tag{3.29}$$

where $\gamma = \dfrac{k_g}{k}R\ln(1 + h)$, $\Delta p_{cg} = p_c - \sigma_g(\pi_c - \pi_g)$ and $\Delta p_{ig} = p_i - \sigma(\pi_i - \pi_g)$. Substituting (3.29) into (3.26) gives the following form of c_1

$$c_1 = \frac{k_g R}{\mu}\left(\frac{\Delta p_{cg} - \Delta p_{ig}}{\ell_g + \gamma}\right) \tag{3.30}$$

The differential equation obeyed by the osmotic pressure (3.23) poses a far greater challenge due to its nonlinearity, for which no standard solution methods exist. Of course, the problem can be solved numerically; however, we are able to find an approximate closed-form solution of the boundary value problem (3.23)-(3.24) which gives us an idea of the behaviour of $\pi(r)$ across the capillary wall. Using the solution for $W(r)$ in (3.23) and introducing

$$\alpha = \frac{(1-\sigma)c_1}{L_D - \sigma^2 L_P} \tag{3.31}$$

the differential equation becomes

$$\pi \frac{d^2\pi}{dr^2} + (\pi - \alpha)\frac{1}{r}\frac{d\pi}{dr} + \left(\frac{d\pi}{dr}\right)^2 = 0 \tag{3.32}$$

We are able to find an approximate closed-form solution of this equation by the following method. Introducing the dimensionless pressure $\bar{\pi} = \frac{\pi}{\alpha}$ and multiplying by r^2 gives

$$r^2\bar{\pi}\bar{\pi}'' + (\bar{\pi} - 1)r\bar{\pi}' + (r\bar{\pi}')^2 = 0 \tag{3.33}$$

where the dashes denote derivatives. Next, we change variables according to

$$\bar{\pi}(r) = u(z), \quad z = \ln r \tag{3.34}$$

and reduce the differential equation to the form

$$uu'' + (u-1)u' + (u')^2 = 0 \tag{3.35}$$

This, in turn, can be reduced to a homogeneous Riccati equation by setting

$$p(z) = u'(z) \tag{3.36}$$

with the result

$$up' + (u-1)p + p^2 = 0 \tag{3.37}$$

Since now the independent variable is missing we can make this equation linear by regarding p as a function of u and making the further change of variable

$$p(u) = \frac{1}{v(u)} \tag{3.38}$$

The resulting differential equation

$$v' - \left(1 - \frac{1}{u}\right)v = \frac{1}{u} \tag{3.39}$$

is linear in v and can easily be solved to give

$$v(u) = c_0 \left(\frac{e^u - 1}{u} \right) \tag{3.40}$$

where c_0 is an arbitrary constant of integration. Now we go backwards to recover the initial variables. Using (3.36) and (3.38) gives

$$\frac{du}{dz} = c_0 \frac{u}{e^u - 1} \tag{3.41}$$

which can be easily be solved by separation of variables

$$I(u) - \ln u = c_0 z + c_{00} \tag{3.42}$$

where c_{00} is another arbitrary constant of integration and the function $I(u)$ is given by

$$I(u) = \int e^u u^{-1} du \tag{3.43}$$

which is the well known modified exponential integral $E_{i_1}(u)$ (Lebedev, 1972, p.32). The latter can be represented in the form

$$E_{i_1}(u) = \gamma + \ln u + \sum_{n=1}^{\infty} \frac{u^n}{nn!} \tag{3.44}$$

where $\gamma = 0.5772157...$ is the Euler-Mascheroni constant; and when this representation is introduced into (3.42) it gives

$$\sum_{n=1}^{\infty} \frac{u^n}{nn!} = c_0 z + c_{00} \tag{3.45}$$

where we have incorporated the constant γ into the still arbitrary constant c_{00}. Finally, we go back to the original variables by using (3.34) and recalling that $\bar{\pi} = \frac{\pi}{\alpha}$,

$$\sum_{n=1}^{\infty} \frac{1}{nn!} \left(\frac{\pi(r)}{\alpha} \right)^n = c_0 \ln r + c_{00} \tag{3.46}$$

Although the solution is given in terms of an infinite series, we can get an idea of the behaviour of the osmotic pressure by noticing that the series can be written as

$$\sum_{n=1}^{\infty} \frac{1}{nn!} \left(\frac{\pi(r)}{\alpha} \right)^n = \frac{\pi(r)}{\alpha} \left[1 + \frac{1}{4} \left(\frac{\pi(r)}{\alpha} \right) + \frac{1}{18} \left(\frac{\pi(r)}{\alpha} \right)^2 + ... \right] \tag{3.47}$$

$$\approx \frac{\pi(r)}{\alpha} \tag{3.48}$$

$$\text{if} \qquad \frac{1}{4} \left| \frac{\pi(r)}{\alpha} \right| \ll 1 \tag{3.49}$$

The assumption (3.49) must be examined in detail. From the work of Patlak et al. (1963), we had a parameter ω', which was defined as

$$\omega' = \bar{c}_s(L_D - \sigma^2 L_P)$$

where $\bar{c_s}$ is the average solute concentration. Note that when deriving the equation for the osmotic pressure field, we replaced this average concentration by the actual concentration; but here, since we are looking for the magnitude of the terms only, we go back to this form. Also from Patlak et al. (1963), for a membrane of thickness δ, the solute permeability could be expressed as

$$P = \frac{\omega' RT}{\delta}$$

where R is the gas constant and T is the temperature. Rearranging these two relations gives

$$L_D - \sigma^2 L_P = \frac{P\delta}{\bar{c}_s RT}$$

Since we are only interested in the approximate values in this estimation process, and since $\bar{c}_s$ is an average concentration, then using van't Hoff's law we can introduce a representative osmotic pressure $\Pi = \bar{c}_s RT$. Then substituting into the expression for α, namely Eq. (3.31) we obtain

$$\alpha = \frac{(1-\sigma)c_1}{P\delta}\Pi$$

Now, $P\delta$ has the dimensions of a diffusion coefficient, namely L^2T^{-1}, and so we use the estimate $P\delta \sim D_c$, where we take the value for D_c to be that in the cleft (2.0×10^{-7} cm^2 s^{-1}) as given in Zhang et al. (2006a). Our final expression then is

$$\begin{aligned}\alpha &= \frac{(1-\sigma)c_1}{D_c}\Pi \\ &\approx 5\Pi\end{aligned}$$

using the values for c_1 from Table 3.1. For the first term approximation to be valid, we require

$$\frac{1}{4}\left|\frac{\pi}{\alpha}\right| \ll 1$$

and for the representative values,

$$\left|\frac{\pi}{\alpha}\right| \approx \frac{\Pi}{5\Pi} \approx \frac{1}{5}$$

which means that the value of

$$\frac{1}{4}\left|\frac{\pi}{\alpha}\right| \approx \frac{1}{20} \ll 1$$

and hence the approximation is reasonable. In such a case we have

$$\pi(r) = c_0 \ln r + c_{00} \tag{3.50}$$

having incorporated α into the arbitrary constants. Then application of the boundary conditions (3.24) gives

$$\pi(r) = \frac{\pi_i - \pi_g}{\ln(1+h)} \ln\left(\frac{r}{R}\right) + \pi_g \tag{3.51}$$

3.2.3 Stress and strain distribution

The motion of the fluid through the poroelastic capillary wall produces a local deformation of the material, and the resulting stress and strain distribution can easily be calculated from Eqs. (3.1), (3.8), (3.9) and (3.10), along with suitable boundary conditions. Substituting (3.8)-(3.9) into the equation of motion (3.1) gives

$$-\frac{\partial P}{\partial x_j} + \lambda \frac{\partial e}{\partial x_j} + 2G \frac{\partial}{\partial x_i} e_{ij} = 0 \tag{3.52}$$

where the first term is related to the filtration velocity W_j according to the generalized Darcy law (3.5). Consistent with our assumptions, the displacement vector $\vec{u} = (u(r), 0, 0)$ in cylindrical coordinates and the only strain tensor components different from zero are

$$e_{rr} = \frac{du}{dr} \tag{3.53}$$

$$e_{\theta\theta} = \frac{u}{r} \tag{3.54}$$

It follows that the cubic dilatation is given by

$$e = \frac{du}{dr} + \frac{u}{r} \tag{3.55}$$

while the divergence of the strain tensor consists only of its radial component which is simply $u''(r) + \frac{1}{r}u'(r) - \frac{1}{r^2}u(r)$, where the dashes denote derivatives. Consequently, Eq. (3.52) takes on the following form

$$u'' + \frac{u'}{r} - \frac{u}{r^2} = -\frac{c_1}{\kappa_c}\frac{1}{r} \tag{3.56}$$

where c_1 comes from the expression for the filtration velocity $\vec{W}$ and is given by Eq. (3.30), and we have introduced the consolidation coefficient κ_c defined by

$$\kappa_c = \frac{k}{\mu}(\lambda + 2G) \tag{3.57}$$

This differential equation is of the Euler type and its general solution is

$$u(r) = c_2 r + \frac{c_3}{r} - \frac{c_1}{2\kappa_c} r \ln r \tag{3.58}$$

where c_2 and c_3 are two arbitrary constants of integration whose determination requires imposition of two boundary conditions. These are obtained from the observation that the dynamics are determined completely by pressure gradients, and that contact stress is independent of pore pressure for incompressible constituents (Kenyon, 1976b). Thus we require that no contact forces act on the inner and outer walls, which amounts to requiring that

$$\tau_{rr}(R) = 0 \tag{3.59a}$$

$$\tau_{rr}(R + \Delta R) = 0 \tag{3.59b}$$

and since from the definition (3.9)

$$\tau_{rr} = \lambda \left(\frac{du}{dr} + \frac{u}{r} \right) + 2G \frac{du}{dr} \tag{3.60}$$

we obtain the two boundary conditions

$$(\lambda + 2G) \frac{du}{dr}\Big|_{r=R} + \left(\frac{\lambda}{R} \right) u\Big|_{r=R} = 0 \tag{3.61}$$

$$(\lambda + 2G) \frac{du}{dr}\Big|_{r=R+\Delta R} + \left(\frac{\lambda}{R + \Delta R} \right) u\Big|_{r=R+\Delta R} = 0 \tag{3.62}$$

which $u(r)$, given by Eq. (3.58), must satisfy. This leads to a closed linear system of algebraic equations for the two unknowns c_2 and c_3, and its solution is straightforward albeit tedious:

$$c_2 = \frac{c_1}{2\kappa_c} \left[1 - \nu + \ln R + \frac{(1+h)^2 \ln(1+h)}{h(h+2)} \right] \tag{3.63}$$

$$c_3 = \frac{c_1}{2\kappa_c} \left[\frac{R^2}{1-2\nu} \frac{(1+h)^2 \ln(1+h)}{h(h+2)} \right] \tag{3.64}$$

where we have assumed that the relation between λ, G, and the Poisson ratio ν is the same as for a Hookean material, namely

$$\frac{G}{\lambda + G} = 1 - 2\nu$$

We once again reiterate that these parameters refer to the solid-fluid mixture, and so the value of the Poisson ratio for the capillary wall is not known a priori, but must

be determined from measurement. Substitution of these expressions into Eq. (3.58), introducing a parameter $\tilde{h}$ defined as

$$\tilde{h} = \frac{(1+h)^2 \ln(1+h)}{h(h+2)}$$

and finally rearrangement gives the final formula for the displacement as

$$u(r) = \frac{c_1}{2\kappa_c}\left[\left(1-\nu+\tilde{h}-\ln\frac{r}{R}\right)r + \left(\frac{\tilde{h}}{1-2\nu}\right)\frac{R^2}{r}\right] \tag{3.65}$$

We note that the dimensionless factor $\frac{c_1}{2\kappa_c}$ can also be written as

$$\frac{c_1}{2\kappa_c} = \frac{\Delta P^{cg}}{4G}\frac{k_g}{k}\frac{R}{\ell_g}\frac{1-2\nu}{1-\nu} \tag{3.66}$$

where

$$\Delta P^{cg} = (p_c - p_g) - \sigma_g(\pi_c - \pi_g) \tag{3.67}$$

is proportional to the Starling force at the glycocalyx. Using the expression for p_g (3.29), we may alternatively write

$$\frac{c_1}{2\kappa_c} = \frac{(\Delta p_{cg} - \Delta p_{ig})(1-2\nu)}{4G(1-\nu)\ln(1+h)(1+\frac{\ell_g}{\gamma})} \tag{3.68}$$

With the displacement known it is then straightforward to calculate the components of the strain, and therefore the dilatation, as well as the radial and angular contact stress. The components e_{rr} and $e_{\theta\theta}$ are given by

$$e_{rr} = \frac{(\Delta p_{cg} - \Delta p_{ig})(1-2\nu)}{4G(1-\nu)\ln(1+h)(1+\frac{\ell_g}{\gamma})}\left[\tilde{h} - \nu - \ln\frac{r}{R} - \left(\frac{\tilde{h}}{1-2\nu}\right)\frac{1}{r^2}\right] \tag{3.69}$$

$$e_{\theta\theta} = \frac{(\Delta p_{cg} - \Delta p_{ig})(1-2\nu)}{4G(1-\nu)\ln(1+h)(1+\frac{\ell_g}{\gamma})}\left[\left(1-\nu+\tilde{h}-\ln\frac{r}{R}\right) + \left(\frac{\tilde{h}}{1-2\nu}\right)\frac{R^2}{r^2}\right] \tag{3.70}$$

and the dilatation is given by Eq. (3.55) which, thanks to Eqs. (3.65) and (3.68), turns out to be

$$e = \frac{(\Delta p_{cg} - \Delta p_{ig})(1-2\nu)}{4G(1-\nu)\ln(1+h)(1+\frac{\ell_g}{\gamma})}\left[(1-2\nu) + 2\tilde{h} - 2\ln\frac{r}{R}\right] \tag{3.71}$$

while the radial stress is given by Eq. (3.60), which leads to the result

$$\tau_{rr} = \frac{\Delta p_{cg} - \Delta p_{ig}}{2(1-\nu)\ln(1+h)(1+\frac{\ell_g}{\gamma})}\left[\tilde{h}\left(1-\frac{R^2}{r^2}\right) - \ln\frac{r}{R}\right] \tag{3.72}$$

Finally, the circumferential stress, or hoop stress, is obtained from (3.9), such that $\tau_{\theta\theta} = \lambda e + 2Ge_{\theta\theta}$, which can be expressed as

$$\tau_{\theta\theta} = \frac{\Delta p_{cg} - \Delta p_{ig}}{2(1-\nu)\ln(1+h)(1+\frac{\ell_g}{\gamma})}\left[1 - 2\nu - \ln\frac{r}{R} + \tilde{h}\left(1 + \frac{R^2}{r^2}\right)\right] \tag{3.73}$$

It should be noted that for a perfectly elastic incompressible material for which $\nu = \frac{1}{2}$ Eq. (3.71) gives $e = 0$, as it should. Furthermore, it is easy to check that the formula (3.72) for the radial stress obeys the boundary conditions (3.59) exactly.

3.3 Results

3.3.1 Parameters

Table 3.1: Model Parameters

Parameter	Symbol	Typical value	Reference
capillary hydrostatic pressure	p_c	2.7 kPa (20 mmHg)	Levick (1991)
capillary osmotic pressure	π_c	3.3 kPa (25 mmHg)	Levick (1991)
interstitial hydrostatic pressure	p_i	-1.3×10^2 Pa (-1 mmHg)	Levick (1991)
interstitial osmotic pressure	π_i	1.6 kPa (12 mmHg)	Levick (1991)
capillary wall reflection coefficient	σ	0.1	Hu and Weinbaum (1999)
glycocalyx osmotic pressure	π_g	1.3 kPa (10 mmHg)	Adamson et al. (2004)
glycocalyx reflection coefficient	σ_g	0.9	Michel and Phillips (1987)
glycocalyx permeability	k_g	3.16 nm^2	Weinbaum et al. (2003)
glycocalyx thickness	ℓ_g	150 nm	Adamson et al. (2004)
capillary wall permeability	k	21.8 nm^2	Adamson et al. (2004)
viscosity	μ	7×10^{-4} Pa s	Levick and Smaje (1987)
capillary radius	R	5 μm	Charm and Kurland (1974)
capillary wall thickness	ΔR	0.5 μm	Charm and Kurland (1974)
capillary length	L	1 mm	Charm and Kurland (1974)

Table 3.1 lists the parameters of our mathematical model, along with their symbols and typical values. Most of them have been either measured directly or derived from measurements and for these we give a reference to the literature in the last column of the table. On the other hand, it is quite clear that these measurements pose a very challenging task, with the result that the uncertainties on the value of some of these parameters are considerable. We now discuss those parameters which must be estimated.

The osmotic pressure just behind the glycocalyx, π_g, is not measurable due to the extremely small scales, and therefore must be inferred. Adamson et al. (2004), based on their detailed microstructural model, estimate π_g to be in the range 0.7-0.9 of π_i under normal hydrostatic pressures and we have thus chosen a value in between these limits. Prescribing a constant value assumes that the dependence of π_g on the flow can be neglected, which we assume will be the case in healthy tissue under normal physiological conditions. This assumption may be removed later, but it adds a layer of mathematical complexity if we wish to make π_g a function of the capillary pressure (and hence flow). We discuss this assumption in more detail at the end of Section 4.2.3.

Based on the estimate of Hu and Weinbaum (1999) for the reflection coefficient of the cleft, we consider it reasonable to take $\sigma = 0.1$ for the all important capillary wall reflection coefficient which enters into our modified Darcy law. Zhang et al. (2006a) used a value of 0.197, calculated from their theory in Zhang et al. (2006b), but even with this value, the magnitude of the filtration changes only slightly. In fact, we show in Section 4.2.3 that large changes in the value of σ have minimal effect on the predictions of our model. As for the capillary wall permeability, k, we derived the approximate value from the work of Weinbaum et al. (2003) in estimating the Darcy permeability for a hexagonal array of circular cylinders, and Adamson et al. (2004), who discuss the dimensions of the cleft-spanning structures.

The two parameters not shown in the table - namely the Poisson ratio ν and the shear modulus G - are needed to describe the stress and strain distribution in the capillary wall. To the best of our knowledge, these two parameters have never been measured in capillary walls. Therefore, we perform a parametric study meant to reveal the sensitivity of the transport process and of the stress and strain distributions to the values of these parameters.

3.3.2 Transport

Figure 3.2 shows the behaviour of the filtration velocity $W(r)$ at each point of the capillary wall predicted by our model for three values of the capillary pressure. From Eqs. (3.25) and (3.30), we observe that, since all physical parameters are positive, the part that determines the sign of c_1 and hence W is the difference $\Delta p_{cg} - \Delta p_{ig}$. Thus, assuming all parameters are constant except for the capillary pressure, we can look at the effect on W of different values of p_c. At low pressure $W(r)$ is slightly

negative, signifying reabsorption. As the capillary pressure increases, the filtration velocity becomes positive and larger - as one would expect - with a slight continuous decrease from the lumen side to the pericapillary side due to the $\frac{1}{r}$ dependence. The pressure at which W is identically zero is about 1.7 kPa, or 17 cmH_2O.

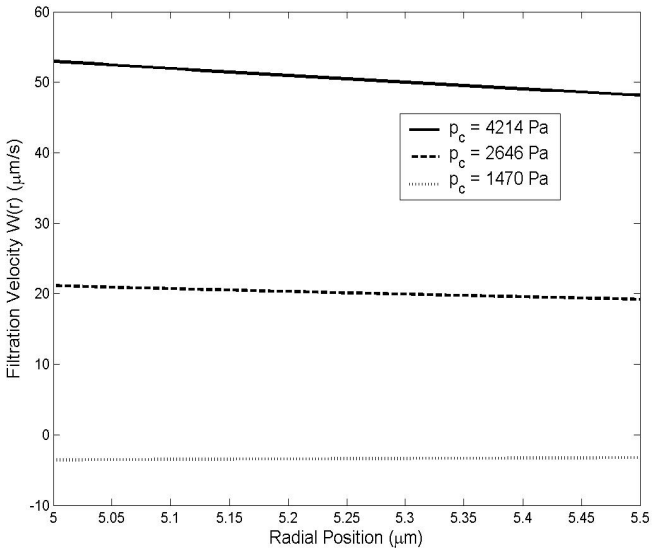

Figure 3.2: Filtration velocity as a function of position across the capillary wall for different values of the capillary pressure.

The behaviour of the effective pressure $P(r) = p(r) - \sigma\pi(r)$ is shown in Figure 3.3 along with the individual values of the hydrostatic and osmotic pressures at low, intermediate, and high values of the capillary pressure p_c. At intermediate and high capillary pressures the effective pressure is positive and decreasing from the lumen to the pericapillary side of the wall, while at low values of p_c we predict a slightly negative value of $P(r)$, increasing very slowly across the capillary wall. Both results are consistent with the sign of the filtration velocity in the respective regions as well as the generalized Darcy law. Interestingly, the effective pressure is close to a pure translation of the hydrostatic pressure. This is easily understood from the fact that the capillary wall reflection coefficient has been assumed to be $\sigma = 0.1$, which means that only 10% of the osmotic pressure contributes to driving the flow, and the fact that the osmotic pressure changes by only a small amount across the wall such that the contribution of $\sigma\pi$ to the effective pressure is close to the same everywhere. If the transport involved molecules larger than albumin, then σ would be larger and so would the contribution of the osmotic pressure. The fact that the osmotic pressure has the same profile regardless of the value of p_c is

due to the assumption mentioned above that π does not depend on the flow.

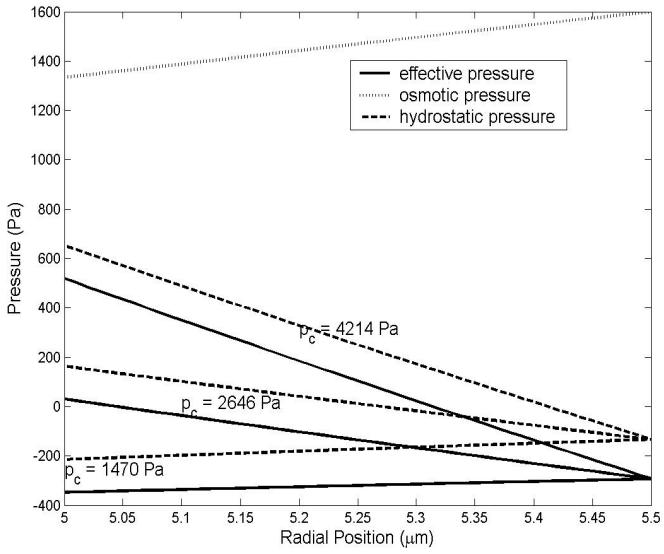

Figure 3.3: Effective pressure, hydrostatic and osmotic pressures as a function of position, for different values of the capillary pressure.

3.3.3 Stress and strain distribution

The contact (Terzaghi) stress distribution predicted by our model is given by Eq. (3.72). It depends on the revised Starling pressure at the glycocalyx $\Delta p_{cg} - \Delta p_{ig}$ and on the Poisson ratio ν, but not on the shear modulus G of the capillary wall. The dependence on ν is shown in Figure 3.4, where the values of the other parameters are those of Table 3.1. The contact stress builds up in the lumen side from zero - as required by the boundary condition (3.61) - to a few Pascal, reaches a maximum in the middle of the capillary wall, and then falls back to zero as required again by the boundary condition (3.62).

To obtain information about the strain, we need only know the displacement, $u(r)$. Eqs. (3.65) and (3.68) show the dependence on the various parameters. Figure 3.5 shows $u(r)$ for different values of the capillary pressure. As to be expected, high values of p_c, corresponding to a high flow situation, produce large displacements, with the maximum values occuring at the inner wall and the values declining across the wall. As capillary pressure decreases, the displacements will become smaller, until a pressure is reached where reabsorption occurs, and below this pressure the displacement is negative.

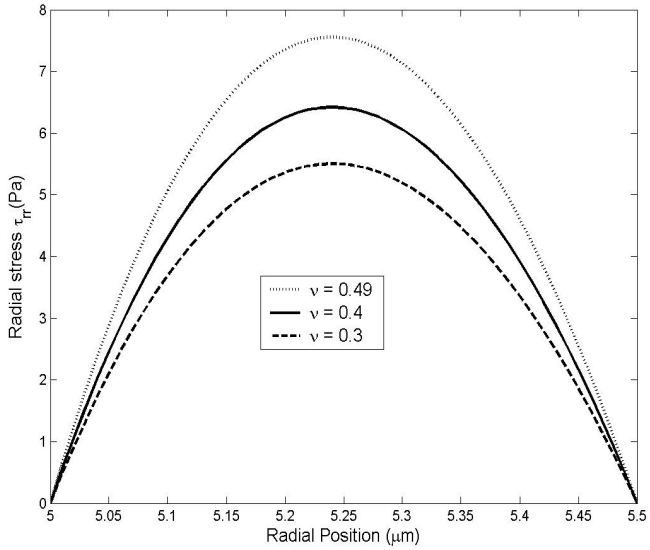

Figure 3.4: Radial stress distribution across the capillary wall, for different values of the Poisson ratio ν.

Figure 3.6 shows u as a function of position across the wall for different values of the shear modulus G and Poisson ratio ν. As expected, a capillary wall that is more stiff, corresponding to larger values of G, will be displaced less, as can be seen in the left figure. The variation with ν is such that as ν is increased, the displacement becomes smaller. Looking at the ordinate axes on both figures shows that u is much more sensitive to changes in G than changes in ν over the parameter range explored here, as the range of values at the luminal side of the wall in the right graph is about 0.02 μm, whereas it is close to 0.3 μm in the left graph.

Within the cylindrical geometry that we are using, it is straightforward to show that the strain consists of a radial part e_{rr} and an angular part $e_{\theta\theta}$. An example of the former is shown in Figure 3.7 for a few values of the shear modulus G and with the Poisson ratio fixed at $\nu = 0.4$. Since $e_{rr} = \frac{du}{dr}$, both the values and the slope of the curves in this figure can be understood from the behaviour of the displacement $u(r)$, which is positive and decreasing from the lumen to the capillary side for values of $p_c \geq 1.7$ kPa. Thus, for these values of p_c, e_{rr} will be negative, with the largest magnitude at the inner wall.

The angular component of the strain is given by $e_{\theta\theta} = \frac{u(r)}{r}$, and its behaviour is shown in Figure 3.7 for the same three values of G as for e_{rr}. The sum of these two is the dilatation e, that is the unit volume (actually, here area) expansion, given by Eq. (3.71) and plotted in Figure 3.8 for a few different values of shear modulus

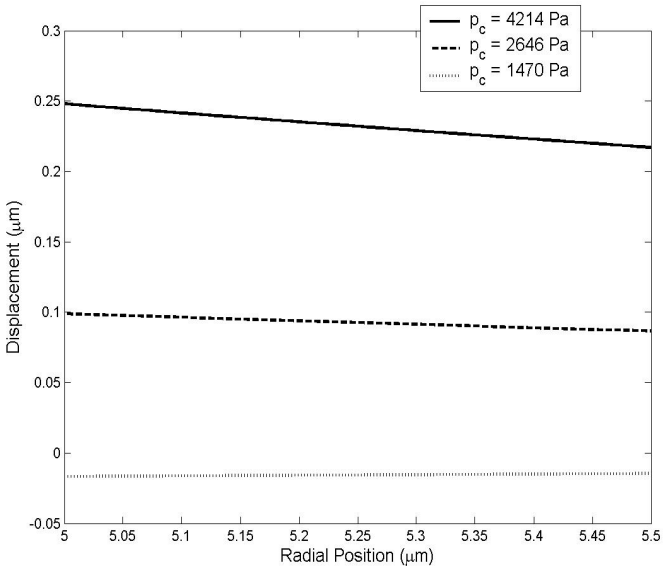

Figure 3.5: Displacement as a function of position for different values of the capillary pressure

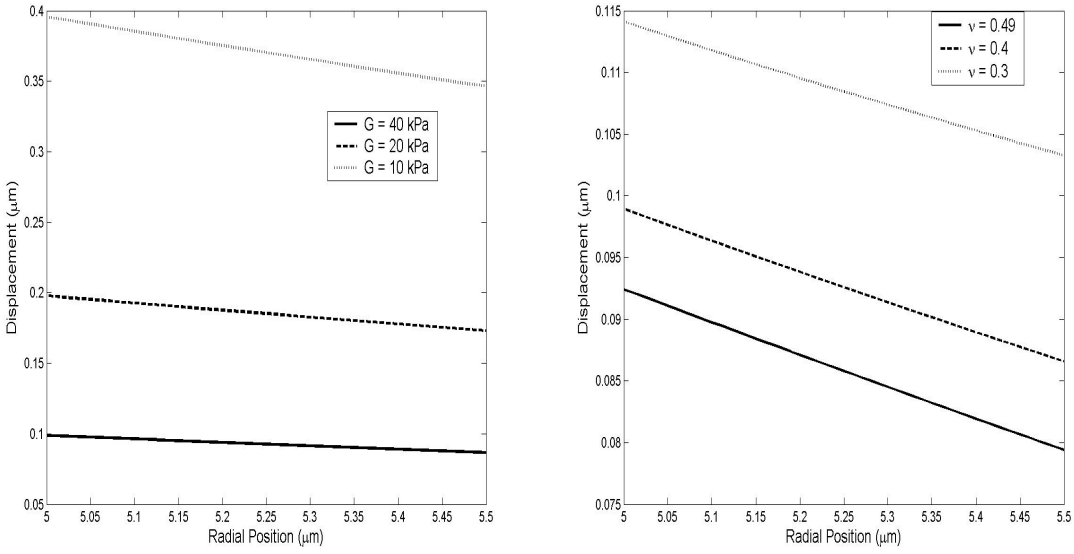

Figure 3.6: Left - Displacement $u(r)$ as a function of position for different values of G with ν fixed at 0.4. Right - Displacement $u(r)$ as a function of position for G fixed and different values of ν

G with ν fixed at 0.4 (left), as well as for values of the Poisson ratio varying from moderately compressible to almost incompressible at the fixed value of $G = 40$ kPa (right). The implications of all these results are discussed in the next section.

3.4 Discussion

The poroelastic model of transcapillary flow developed herein is based on two fundamental modifications of the classical theory of consolidation (Biot, 1941; Kenyon, 1979, 1976b). Firstly, we have extended Darcy's law to include the effect of osmotic pressure in the mechanism of filtration through the capillary wall. Secondly, we have embraced the Michel-Weinbaum hypothesis of a revised Starling law in which the balance of driving forces is applied across the endothelial glycocalyx layer rather than between lumen and tissue.

Our theoretical development is different from extant theoretical models which are based on the heterogeneous microstructure of the capillary wall (Hu and Weinbaum, 1999; Adamson et al., 2004; Zhang et al., 2006a; Fu et al., 1994). Classical poroelasticity models, in contrast, are based on homogenization of the microstructure - a mathematical procedure which replaces the actual porous medium with a homogeneous fluid-solid mixture (Burridge and Keller, 1981). This offers a considerable simplification of the problem, of course; but, more than that, it is a necessary approximation in view of our inability to map accurately the boundary surface between the fluid in the pores and the solid matrix. As the Reynolds number of this flow is very small, we know that the Stokes equations will give a very accurate representation of the fluid motion; and we know from Elasticity Theory how to accurately describe the solid matrix. What we don't know is how to enforce the boundary conditions (no slip, and continuity of the stresses) for the simple reason that such boundaries are unknown.

When confronted with this problem in their ultrastructural model Hu and Weinbaum (1999) replaced the wide part of the cleft between facing cells with two flat, parallel, and rigid walls separated by a very small distance. The space between the cells is assumed to be occupied partly by fluid and partly by 'obstacles' such as the crossbridging structures observed by Schulze and Firth (1992) and Adamson et al. (2004). This arrangement is very close to the well-known Hele-Shaw flow for which it is known that the no-slip conditions are satisfied on the plates but not on the surface of the 'obstacles' (Batchelor, 1967). The hydrodynamic resistance of the

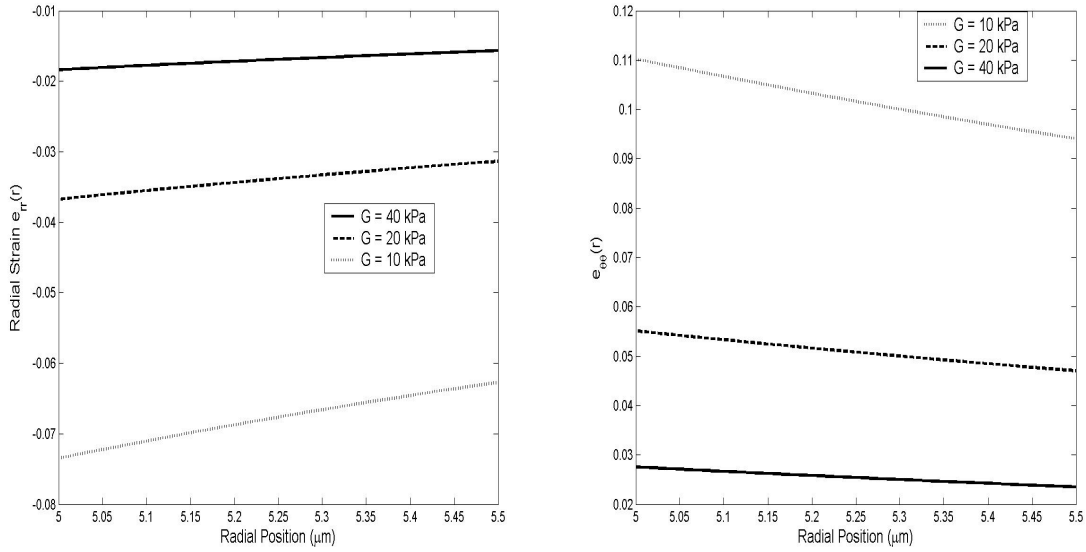

Figure 3.7: Left - Radial strain e_{rr} as a function of position for different values of G and ν fixed at 0.4. Right - Angular strain $e_{\theta\theta}$ as a function of position for different values of G and ν=0.4.

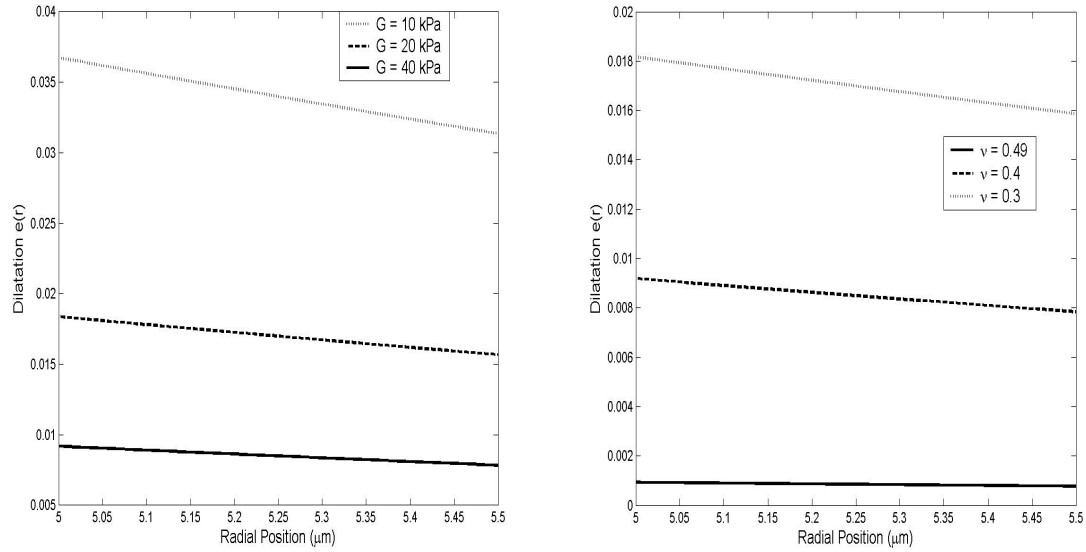

Figure 3.8: Left - Dilatation e as a function of position for different values the shear modulus G. Right - Dilatation as a function of distance for different values of the Poisson ratio ν.

latter, however, is partly recovered by a modification of the Hele-Shaw flow which ultimately results in the replacement of the viscosity by an effective viscosity, as first shown by Tsay et al. (1989).

The considerable mathematical complications introduced by this procedure is compounded by the calculation of the solute concentration field, which requires the solution of the convection-diffusion equation subject to the different boundary conditions dictated by the different regions of the cleft and the tissue space. As a consequence, this three-dimensional microstructural model is difficult to use, and was recognized as such by Zhang et al. (2006a), who replaced it with a simpler one-dimensional version in which the transport coefficients are adjusted to reproduce the fluxes predicted by the three-dimensional model.

These difficulties notwithstanding, the microstructural models have contributed enormously to our understanding of transcapillary flow, particularly for their ability to extract reasonably accurate values of the parameters that we have listed in Table 3.1. Because of homogenization, our filtration velocity cannot be compared directly with the calculation of Hu and Weinbaum. What has been measured, however, is the volume flow through a unit area of capillary wall as a function of capillary pressure. To compute this quantity, denoted $\frac{J_v}{A}$, we integrate $W(r)$ over the annulus $R \leq r \leq R + \Delta R, 0 \leq \theta \leq 2\pi$ and divide by the surface area of the capillary, which in our case is $2\pi RL$, where L is the capillary length. We find

$$\frac{J_v}{A} = \frac{c_1 h}{L} \tag{3.74}$$

which upon expanding c_1 becomes

$$\frac{J_v}{A} = \frac{k_g h R}{\mu \ell_g L} \left(\frac{1}{1 + \frac{\gamma}{\ell_g}} \right) \left(p_c - p_i - [\sigma_g(\pi_c - \pi_g) - \sigma(\pi_i - \pi_g)] \right) \tag{3.75}$$

The coefficient of p_c in Eq. (3.75) is the hydraulic conductivity, L_P, which can be simplified to

$$L_P = \frac{hR}{\mu L} \left(\frac{1}{\frac{\ell_g}{k_g} + \frac{R}{k} \ln(1+h)} \right) \tag{3.76}$$

Now if we recall the discussion from the classical Starling equation, the intercept on the graph was referred to as the isogravimetric capillary pressure or effective osmotic pressure, which is simply pressure at which there is no filtration, we can

write $p_0 = p_i + (\sigma_g(\pi_c - \pi_g) - \sigma(\pi_i - \pi_g))$, and express

$$\frac{J_v}{A} = L_P(p_c - p_0) \tag{3.77}$$

Note the difference with the classical Starling equation in that there are now two separate components of the osmotic force - that from capillary across the glycocalyx, and that from the region behind the glycocalyx to the interstitium.

We plot $\frac{J_v}{A}$ as a function of p_c in Figure 3.9, and our result compares favorably with both the old measurements of Michel et al. (1974) and the recent ones of Adamson et al. (2004). As our poroelastic theory is linear from the start, Eq. (3.75) is not directly comparable to the steady-state nonlinear theory of Michel and Phillips (1987), but we note that our prediction of $\frac{J_v}{A}$ is of the same order of magnitude as their transient results, and so is the slope of the line. The value of L_P in our equation is 1.0×10^{-7} cm cmH_2O^{-1} s^{-1} which compares well with the value of L_P quoted in the literature cited above (Adamson et al. (2004) give a value of 1.24×10^{-7} cm cmH_2O^{-1} s^{-1}). The intercept on the p_c-axis, corresponding to the pressure at which zero filtration occurs, is 17 cmH_2O.

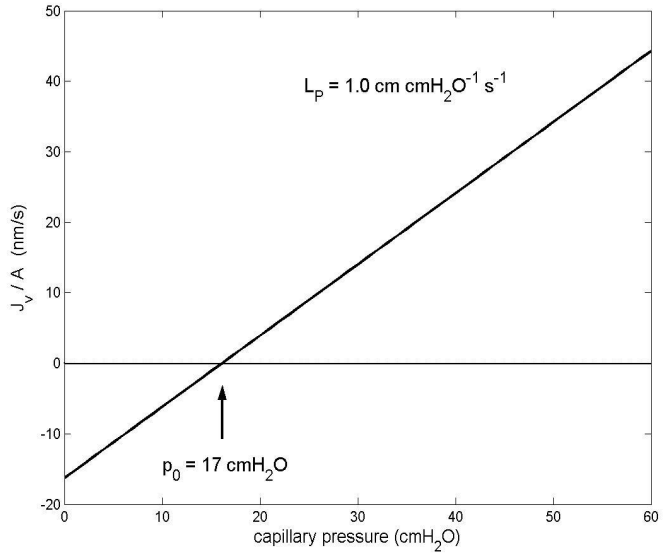

Figure 3.9: Classical Landis-Starling diagram - Filtration flux per unit area as a function of capillary pressure. The slope of the line is the hydraulic conductivity L_P, which is 1.0×10^{-7} cm cmH_2O^{-1} s^{-1}, and the intercept on the p_c axis is 17 cmH_2O.

One of the essential hypotheses that comes from the analysis of Hu and Weinbaum (1999) is that the interstitial protein concentration, and hence osmotic pressure, is not a major determinant of flow. Instead, it is the osmotic pressure behind

the glycocalyx. To test this experimentally, both Hu et al. (2000) and Adamson et al. (2004) elevated the albumin concentration in the tissue to that of the capillary, such that $\pi_i = \pi_c$. Then according to the classical Starling principle, the effective oncotic force would be zero, and hence the $\frac{J_v}{A}$ vs. p_c curve should pass through the origin. However, in both experiments, this was shown not to be the case, and thus it was inferred that although there was no concentration difference between the plasma and tissue, there is an oncotic force exerted. Adamson et al. (2004) proposed that this force must be exerted across the glycocalyx.

In our theory, π_i enters the expression for $\frac{J_v}{A}$ with a factor of σ in front. This is an important point, as the value of σ is only 0.1, meaning that even large changes in π_i have only a small effect on filtration. For instance, we take the value of π_i in Table 3.1 as our boundary condition, but if the value were doubled to π_c, the actual difference in the magnitude of $\sigma\pi_i$ would be less than 2 $\mathrm{cmH_2O}$, and thus the effect on the $\frac{J_v}{A}$ vs. p_c curve would be only a small shift. Thus, our model is faithful to the fact that the interstitial osmotic pressure is not an important determinant of flow.

It should be pointed out that when π_i is increased, the osmotic pressure behind the glycocalyx, π_g, which Hu and Weinbaum (1999) showed depends on the flow conditions, may or may not be affected. We use the simplifying assumption of a constant π_g as a boundary condition, and so there is no possibility of coupling in our model. This is discussed further in the Conclusion. However, we can perform a sensitivity analysis on π_g. Figure 3.10 shows the filtration flux as a function of capillary pressure in the case where $\pi_i = \pi_c$, for different values of π_g. For the low value of π_g, the result is shifted 2 $\mathrm{cmH_2O}$ from Figure 3.9. The curves are progressively shifted to the left as π_g is increased, with the intercept on the p_c-axis decreasing by about 5 $\mathrm{cmH_2O}$ for each value. For the highest value, where $\pi_g = \pi_i$, the line passes through the origin since the osmotic force across the wall would be identically zero. So although our poroelastic theory cannot explain the detailed mechanism of the coupling between π_i and π_g, we can estimate the filtration flux for a range of π_g values as in the figure.

A unique feature of the poroelastic model is its ability to predict the stress and strain distribution across the capillary wall. So far as we are aware, no similar calculations have been done before and no measurements have been attempted. However, taking advantage of our analytical results, we have carried out a sensitivity analysis of the dependence of these quantities on the two basic parameters of the theory, namely the shear modulus G and the Poisson ratio ν, and typical results

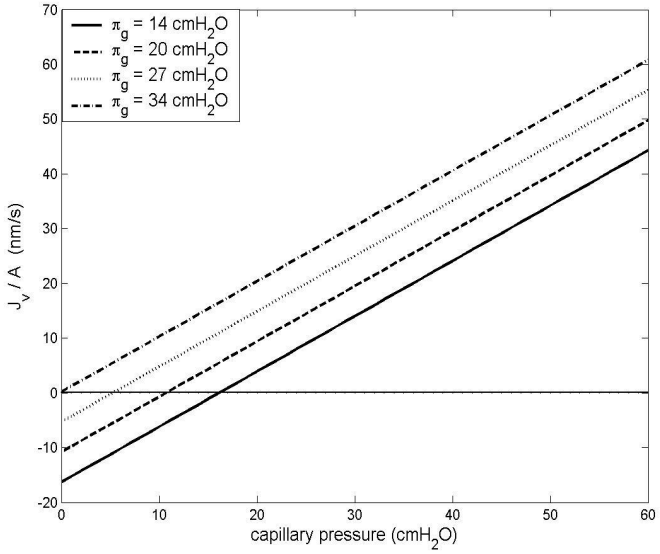

Figure 3.10: Filtration flux per unit area as a function of capillary pressure for different values of π_g in the case where π_i is elevated to that in the capillary.

are shown in Figures 3.4-3.8. Insofar as the contact stress is concerned, Eq. (3.72) shows that it is independent of G and that its dependence on ν is such that τ_{rr} increases as ν tends to the perfectly elastic solid value of 0.5, a behavior that is clearly illustrated in Figure 3.4.

The strain components depend on both G and ν and their behavior is displayed in Figure 3.7. The radial component takes on negative values, with small values of G leading to the largest (negative) values of e_{rr}. The angular component is positive and increases with decreasing G. Their sum - the dilatation, that is the local change of volume in the capillary wall - is exhibited in Figure 3.8 for the same values of G and ν. The dilatation increases with decreasing G, as to be expected from a less stiff material. With increasing ν, the dilatation decreases, of course approaching zero as ν approaches its elastic solid limiting value of $\frac{1}{2}$. Since, in order to be consistent with the linearity of the theory, the dilatation should not exceed a few percent, these results lead us to hypothesize that the value of ν for a capillary wall should lie in the interval $0.3 \leq \nu \leq 0.4$, while that of G should be approximately 20 kPa $\leq G \leq$ 40 kPa for a capillary pressure of the order of 3 kPa. We are hopeful that with the rapidly improving technological capabilities, experimentalists will soon be able to test our hypothesis.

The analysis carried out above leads us to draw the conclusion that *our poroelastic model is capable of reproducing the filtration flux as a function of capillary*

pressure predicted by the ultrastructural models and observed experimentally. This successful test of our model makes us confident that it will be able to give us valuable insights into both physiological and pathophysiological phenomena. In particular, a study by van den Berg et al. (2003) has shown that enzymatic degradation of the endothelial glycocalyx is one of the contributing factors to increased permeability of the capillary wall and pericapillary edema. Since the glycocalyx properties enter into our theory (in the Michel-Weinbaum hypothesis), a quantitative comparison seems a good test of our model. The following chapter will examine how the alteration of glycocalyx properties affects transcapillary flow.

Chapter 4

The effect of a deteriorated endothelial glycocalyx on transcapillary flow

4.1 Glycocalyx background and motivation for study

The existence of an endocapillary layer, later to be termed the endothelial glycocalyx, was first demonstrated by Luft (1966) via an electron microscopic study using ruthenium red staining. He observed the layer to be irregularly shaped, and estimated the thickness to be about 20 nm. Subsequent work aimed at identifying the composition of the layer and the reviews of Pries et al. (2000) and Weinbaum et al. (2007) give excellent summaries of various aspects of glycocalyx research. Vink and Duling (1996), by comparing the capillary anatomical diameter to its functional diameter, and Smith et al. (2003), who made the first direct estimates of glycocalyx thickness *in vivo*, estimate the thickness to be between 0.4-0.5 μm. Squire et al. (2001) used electron microscopy to show that the core proteins comprising the glycocalyx form a quasi-periodic bush structure in which the fiber diameter is 10-12 nm with spacing of 20 nm. In addition, this structure links to an underlying actin cortical web forming a hexagonal array with 100 nm spacing. Identification of these structural properties led investigators to examine the function of the glycocalyx, and in recent years a plethora of physiological functions have been identified. Al-

ready discussed above (Section 2.6) is the glycocalyx function as a molecular sieve in determining the Starling forces responsible for transcapillary flow.

The glycocalyx is most likely the primary factor involved in mechanotransduction of fluid shear stress into cell signaling processes triggering nitric oxide (NO) production and cytoskeletal reorganization (Tarbell and Pahakis, 2006). Weinbaum et al. (2003) proposed that the core proteins comprising the glycocalyx have a sufficiently stiff bending rigidity to withstand deformation due to physiological shear stresses, and through their connections to the underlying cortical cytoskeleton (CC) convert the fluid shear stress into deformations of the CC. Thi et al. (2004) showed, by measuring the levels of several key structural proteins (e.g. F-actin), that an intact glycocalyx is necessary for shear-induced cytoskeletal reorganization. It has also been found that after treatment with heparinase (Florian et al., 2003) or hyaluronidase (Mochizuki et al., 2003) (to break down the heparan sulfate or hyaluronan components of the glycocalyx, respectively), mechanotransduction was blocked with corresponding impaired shear-induced NO production. Thus, degradation of any component of the glycocalyx will reduce its capability to translate shear stress into biochemical signals.

Interactions of both red and white blood cells (RBCs, WBCs) with the glycocalyx have been studied extensively. Early models of RBC motion in capillaries lined with glycocalyx were able to predict the experimentally observed increase in resistance as compared to flow in glass tubes, as well as the reduction in capillary tube haematocrit (Secomb et al., 1998; Damiano, 1998). Feng and Weinbaum (2000) used lubrication theory to explain the pop-out phenomenon observed by Vink and Duling (1996), in which a RBC at rest will lift off the capillary wall as the flow velocity increases. They attribute this to a large repulsive force generated within the glycocalyx due to axial flow through the layer, and interestingly draw an analogy between this phenomenon and a human skiing on snow. Secomb et al. (2001) examined changes in shape of RBCs as a function of velocity, and were able to quantitatively describe the exclusion of RBCs from the glycocalyx layer in flowing capillaries. In terms of interactions with WBCs, the glycocalyx has been shown to inhibit WBC adhesion to the endothelium (Constantinescu et al., 2003) and in addition to mediate leukocyte rolling (Henry and Duling, 2000), suggesting that it is highly likely that there is an important role for the glycocalyx in the inflammatory response (see e.g. Weinbaum et al., 2007 for review).

Possibly the best evidence for an important physiological function of the glycocalyx is its modulation in pathogenic states. For example, recent work has found the

glycocalyx to be degraded or absent in conditions such as atherosclerosis (van den Berg et al., 2006; Brands et al., 2007), diabetes (Nieuwdorp et al., 2006), and ischaemia/reperfusion (Mulivor and Lipowsky, 2004).

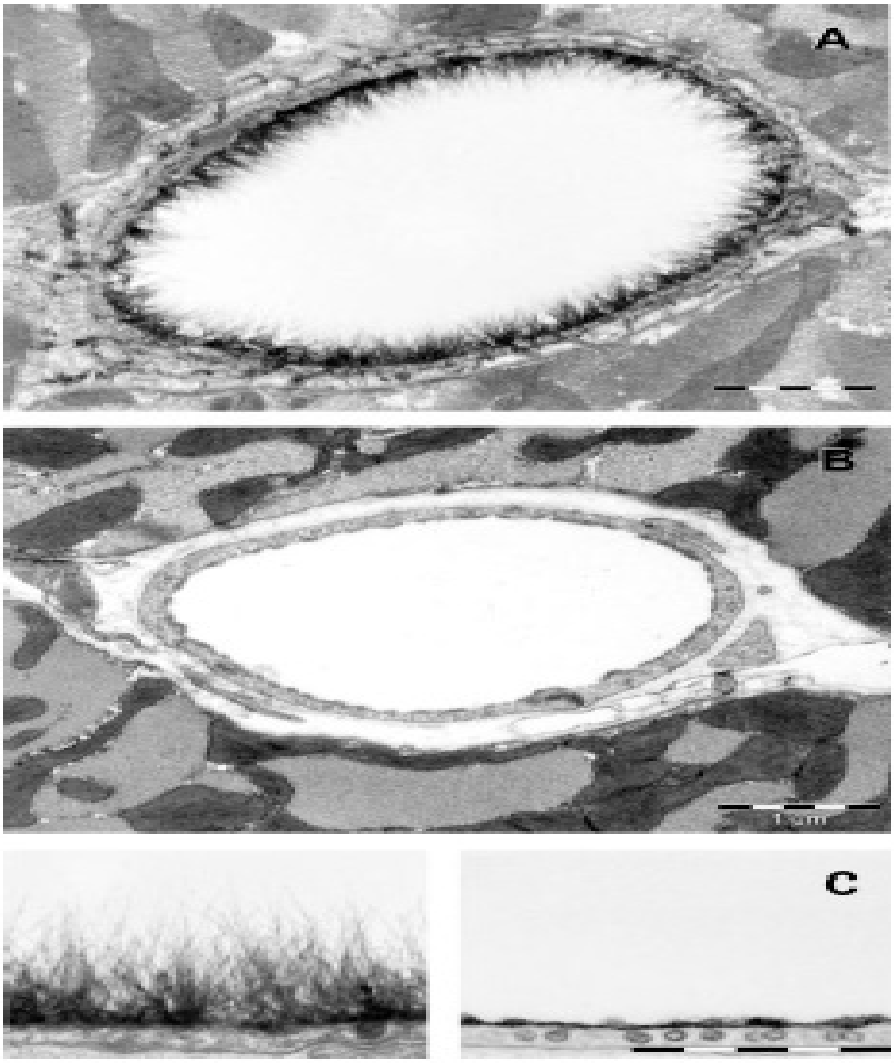

Figure 4.1: Electron microscopic images from van den Berg et al. (2003). In the control (A), the hair-like protrusions of the glycocalyx can clearly be seen, whereas the pericapillary space is barely visible. In the hyaluronidase-treated case (B), the glycocalyx is shown to be absent, and the pericapillary space (white area outside the capillary) is swelled. (C) is a close-up of the luminal surface of the endothelium. Reprinted with permission.

In a particularly interesting experiment, van den Berg et al. (2003) used hyaluronidase to degrade the glycocalyx in rat myocardial capillaries and measured the resulting glycocalyx dimension and that of the pericapillary space. By stabilizing the carbohydrate structures of the glycocalyx, they were able to visualize these structures using electron microscopy. They found that the glycocalyx dimension

was indeed decreased upon treatment with hyaluronidase, and correspondingly that the dimension of the surrounding pericapillary space was increased, as can be dramatically seen in Figure 4.1. This led to the conclusion that the glycocalyx acts as a protective barrier against edema formation, at least in rat myocardial capillaries.

Since the glycocalyx appears in our model of transcapillary exchange, specifically in the Michel-Weinbaum boundary condition (3.21), a comparison between the predictions of our theory with this experiment seems a natural test of our model. Under hyaluronidase treatment, the properties of the glycocalyx change, as seen for example in the decrease in thickness in the experiments of van den Berg et al. In the following, we seek to explain the formation of edema as a result of glycocalyx deterioration by using our model to examine how transcapillary flow is modified as a result of an altered glycocalyx that may occur due to enzymatic degradation.

We begin Section 4.2 by using the measurements of van den Berg et al. (2003) for the pericapillary space dimension around control and hyaluronidase-treated capillaries to predict the increase in the amount of fluid in the pericapillary space as a result of glycocalyx deterioration. We then recap how the glycocalyx enters into our model, in particular discussing the parameters that characterise the glycocalyx, such as its thickness and permeability. Following this, we use as input into our model the data of van den Berg et al. (2003) for glycocalyx thickness in normal and hyaluronidase-treated capillaries and attempt to draw a quantitative comparison. We continue with a parametric study before comparing our predictions to experimental data as well as other theoretical studies. Finally, in Section 4.2.5, we discuss both our modeling approach and others, pointing out the various predictions made by each, and where experimental observations will prove useful.

In Section 4.3, we continue our comparison with van den Berg et al. (2003), now using all of the available data, rather than simply the median of the measurements. We begin by finding probability distributions that best fit the data of van den Berg et al. (2003) for pericapillary space dimension in the control and hyaluronidase-treated cases. We then use those distributions to calculate the change in the amount of fluid in the pericapillary space, which is now a distribution also. Based on this, we then calculate the statistical properties for the glycocalyx thickness. We conclude with a discussion of our underlying assumptions, as well as the physiological implications of this work.

4.2 The effect of the endothelial glycocalyx

4.2.1 Increase in fluid content in the pericapillary space

Van den Berg et al. (2003) quantify edema formation by measuring the *pericapillary space dimension* (PSD) around capillaries in both the normal and deteriorated glycocalyx cases. They calculate the PSD by "subtracting the outer capillary diameter from the inner diameter of the surrounding myocardial tissue" (van den Berg et al., 2003), and after taking measurements in 0.2 μm intervals around the perimeter, they express the result as a median value. The median PSD is given as 0.28 μm for control capillaries (intact glycocalyx), and 0.46 μm for hyaluronidase-treated capillaries (deteriorated glycocalyx).

For our purposes, the PSD is important in that it allows us to calculate the increase in fluid content due to glycocalyx degradation. One could potentially measure the amount of fluid by counting pixels from an electron microscope image (e.g. Figure 4.1), but we instead make a simplifying assumption that the capillary cross-sectional geometry must be either circular or elliptic. This enables us to use the PSD to compute the area change, and hence estimate the change in fluid content in the pericapillary space, between control and hyaluronidase-treated capillaries for these two geometrical configurations.

We compute the area of the pericapillary space for the separate cases of intact and deteriorated glycocalyx, then find the relative area change using the formula

$$\Delta A = \frac{A_h - A_c}{A_c} \tag{4.1}$$

where A_h and A_c are the areas of the pericapillary space in hyaluronidase-treated and control capillaries, respectively. In the circular case, we know that the area of an annulus with inner radius R and outer radius $R+\Delta R$ is $A = \pi(R+\Delta R)^2 - \pi R^2$. Taking the inner radius to be that of the capillary, R, and the outer radius that of the capillary plus PSD, and letting R_h and R_c be the median PSD in the separate cases, the expression simplifies to

$$\Delta A = \frac{(R+R_h)^2 - (R+R_c)^2}{(R+R_c)^2 - R^2} \tag{4.2}$$

The relative area change is shown as a function of capillary radius R in the left graph of Figure 4.2.

For the case of an elliptic cross-section, and making the assumption that the pericapillary space is displaced the same amount ΔR in the directions of the semi-major and semi-minor axes, the area of the elliptic annulus is

$$A_e = \pi(a + \Delta R)(b + \Delta R) - \pi ab$$

where a, b are the semi-minor and semi-major axes. The expression for the area change is then

$$\Delta A_e = \frac{(a + R_h)(b + R_h) - (a + R_c)(b + R_c)}{(a + R_c)(b + R_c) - ab} \tag{4.3}$$

The relative area change is shown as a function of the semi-major axis b in the right side of Figure 4.2 for different values of the semi-minor axis a.

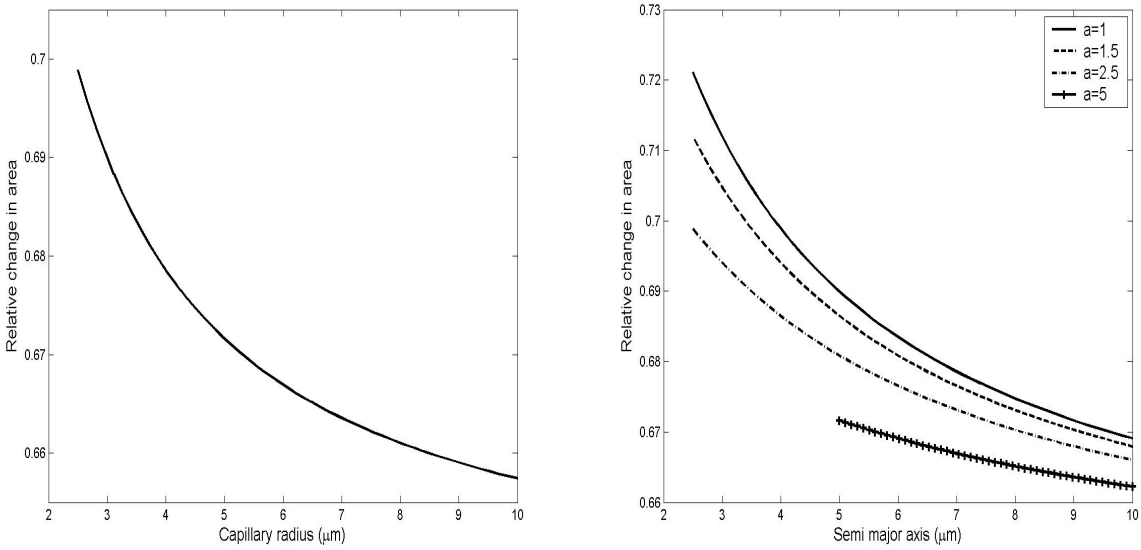

Figure 4.2: Left - Area change as function of capillary radius (circular case). Right - Area change as a function of semi-major axis, for various values of semi-minor axis a (elliptic case).

It is clear from Figure 4.2 that for a wide range of radii, or semi-major/minor axes, the relative area change lies between about 0.66-0.72 (i.e. is an increase of 66-72%). This means that for the measurements of pericapillary space dimension in van den Berg et al. (2003), and for capillary sizes in the physiological range, the increase in area of the annular region, and hence in the amount of fluid in the pericapillary space, has approximately this magnitude. The only assumptions made in this estimation are: 1) that the median values of PSD may be used for the calculation, and 2) that the cross-section of the capillary has simple geometry.

Regarding the former, this assumption is dropped in Section 4.3 when we attempt to fit the PSD histograms using probability distributions. As regards the latter, it is observed from the figures that circular and elliptic geometries produce only slightly different results, and thus any other geometric configuration will likely be close to the range of values calculated here.

To make a comparison, we must relate ΔA with a quantity that can be predicted by our model. We discuss this quantity as it relates to the glycocalyx in the next section.

4.2.2 The role of the glycocalyx in our model

In our mathematical model, the glycocalyx appears in the boundary condition enforcing the Michel-Weinbaum hypothesis (3.21), which relates the flow velocity behind the glycocalyx to the hydrostatic and osmotic pressure differences across it. The three parameters describing the glycocalyx are its thickness, ℓ_g, permeability, k_g, and reflection coefficient, σ_g. Our current aim is to investigate the effects of changes in the glycocalyx properties that may occur as a result of enzymatic degradation as in the experiments of van den Berg et al. (2003). To do this, we must solve the equations in the model and express the variables as functions of these glycocalyx parameters.

An important parameter in microvascular exchange, and a major focus herein, is the hydraulic conductivity, L_P. As previously mentioned, this quantity is the slope of the graph of $\frac{J_v}{A}$ versus the capillary pressure, p_c, and is thus essentially the determinant of how much fluid flows across the capillary wall for a given pressure drop. This parameter is important for our comparison not only because is it measurable, but also because our theory gives an expression for L_P in terms of the parameters that characterise the glycocalyx, namely its thickness (ℓ_g) and permeability (k_g), as seen in Eq. (3.76). We reproduce this equation now for convenience

$$L_P = \frac{hR}{\mu L}\left(\frac{1}{\dfrac{\ell_g}{k_g} + \dfrac{R}{k}\ln(1+h)}\right)$$

Since ℓ_g and k_g may be expected to change with enzymatic treatment, looking at the behaviour of L_P as these parameters vary will give a prediction of the effect of glycocalyx degradation on transcapillary fluid flow.

There are two important limits of L_P to observe, and these limits correspond to the cases when the resistance of the glycocalyx is much smaller than that of the capillary wall, and when the glycocalyx is the dominant resistance to flow. The key to looking at these limits is the dimensionless parameter $\frac{\gamma}{\ell_g}$, where, if we recall the definition of γ (see Eq. 3.29), we obtain

$$\frac{\gamma}{\ell_g} = \frac{k_g R \ln(1+h)}{\ell_g k}$$

so that using the relation $h = \frac{\Delta R}{R}$, and introducing $\Gamma = \frac{\gamma}{\ell_g}$ the expression for the important dimensionless parameter becomes

$$\Gamma = \frac{k_g}{k}\frac{\Delta R}{\ell_g}\frac{\ln(1+h)}{h} \tag{4.4}$$

In the form (4.4), it is easy to see that Γ contains two important ratios: that of the glycocalyx and capillary wall permeability k_g/k, and that of the thickness of the capillary wall region and glycocalyx $\Delta R/\ell_g$. The factor $\frac{\ln(1+h)}{h}$ is close to one since $h = 0.1$. Thus, Γ is a measure of the relative resistances to flow of the capillary wall and glycocalyx.

Therefore, the case in which the glycocalyx provides negligible resistance compared to that of the capillary wall is when $\Gamma \gg 1$, which corresponds to the situation when the glycocalyx thickness decreases to zero, or equivalently when the glycocalyx permeability approaches infinity. This limit is

$$\lim_{\ell_g \to 0} L_P = \lim_{k_g \to \infty} L_P = \frac{k}{\mu}\frac{h}{L\ln(1+h)} \tag{4.5}$$

The existence of this limit allows us to calculate how much resistance the glycocalyx contributes to the transcapillary flow for various parameter combinations, and this will be done in the next section. In the other limit, that is when the resistance to flow due to the glycocalyx is dominant (when $\Gamma \ll 1$), which can also be described as the limit in which the capillary wall permeability approaches infinity, we get the following

$$\lim_{k \to \infty} L_P = \frac{k_g}{\mu \ell_g}\frac{\Delta R}{L} \tag{4.6}$$

We now compare our model predictions for excess flow with the observations of edema formation in van den Berg et al., as well as results from other studies.

4.2.3 Consequences of glycocalyx deterioration

In order to compare the predictions from our theory to the experiments of van den Berg et al. (2003), we need to relate a parameter that our model is capable of calculating to the above approximation for the increase in fluid content. Recall that changes in L_P (for constant capillary pressure) represent changes in the amount of fluid flowing, and hence in the amount of fluid in the pericapillary space. For instance, if there is a two-fold increase in L_P, we would expect approximately a two-fold increase in fluid content in the pericapillary space. That is, we use the approximation

$$\Delta A = \Delta L_P = \frac{L_{P,d} - L_{P,c}}{L_{P,c}} \tag{4.7}$$

where $L_{P,c}$ and $L_{P,d}$ refer to the L_P values in the control and glycocalyx-degraded cases.

Of course, this is just a rough approximation. In reality, fluid that flows through the capillary wall moves slowly through the interstitial matrix, mixing with fluid from other capillaries before entering the lymphatic system. An excess amount of fluid in the interstitial space will in turn cause a corresponding increase in interstitial fluid pressure due to the compliance of the tissue, which will in turn oppose further flow in accordance with the Starling principle. This is a highly dynamic process, and a more realistic model would require a mathematical description of capillary and lymphatic networks embedded in a tissue, which is outside the scope of our current work. This assumption will be discussed in more detail below in Section 4.3.4, where the possibility of different functional relationships will be examined.

Under enzymatic degradation, the three characteristic paramaters of the glycocalyx, that is ℓ_g, k_g, and σ_g, may all be expected to change; unfortunately there are no data of which we are aware that documents changes in permeability or reflection coefficient. Thus, for the moment we restrict our consideration to changes in glycocalyx thickness, and discuss changes in k_g and σ_g later in this section. We take the measurements in van den Berg et al. (2003) of ℓ_g from 429 normal and 196 hyaluronidase-treated capillaries and use these as input into our model. The mean glycocalyx thickness "was determined by the distance between the luminal membrane and the optical background density plus 2×SD, representing ≈ 95% of detectable stained structures" (van den Berg et al., 2003). It was found to be 182 nm in normal capillaries and 77 nm in hyaluronidase-treated capillaries. As with the PSD measurements, we ignore the variation in data and proceed to our calculations using only the two mean values. For $\ell_g = 182$ nm, we predict an L_P of

0.88×10^{-7} cm s^{-1} cmH$_2$O^{-1}, whereas in the case when $\ell_g = 77$ nm, L_P increases up to 1.51×10^{-7} cm s^{-1} cmH$_2$O^{-1}. The increase in L_P is 72%. That is, we estimate the change in pericapillary fluid content due to glycocalyx deterioration as an increase of 72%, which agrees reasonably well with the change in area calculated in Eq. (4.2) and shown in Figure 4.2.

An alternative way to examine how our model compares to the data is the following. Recall the assumption made in Eq. (4.7) that the relative change in area will correspond to the relative change in hydraulic permeability. Thus, given the L_P value in the control situation (denoted $L_{P,c}$), we are able to calculate the value in the hyaluronidase-treated case where the glycocalyx is degraded (denoted $L_{P,d}$) based on the values of ΔA calculated from Eq. (4.2). To obtain the value of $L_{P,c}$, we must know the glycocalyx thickness in the control case, call it $\ell_{g,c}$, so that we can use the expression derived from our theory, namely (3.76). The separate forms for the control and glycocalyx-degraded cases are

$$L_{P,c} = \frac{hR}{\mu L}\left(\frac{1}{\frac{\ell_{g,c}}{k_{g,c}} + \frac{R}{k_c}\ln(1+h)}\right) \tag{4.8}$$

$$L_{P,d} = \frac{hR}{\mu L}\left(\frac{1}{\frac{\ell_{g,d}}{k_{g,d}} + \frac{R}{k_d}\ln(1+h)}\right) \tag{4.9}$$

where the parameters $k_{g,c}, k_{g,d}, k_c, k_d$ represent the glycocalyx permeability (control and degraded) and capillary wall permeability (control and degraded), respectively. Then, taking the ratio $\dfrac{L_{P,c}}{L_{P,d}}$ we may rearrange the equations to get a formula for $\ell_{g,d}$, the glycocalyx thickness upon degradation, in terms of $\ell_{g,c}$, the ratio $\dfrac{L_{P,c}}{L_{P,d}}$, and the other transport parameters which for now have been assumed to remain constant (that is $k_{g,c} = k_{g,d} = k_g$ and $k_c = k_d = k$). This relation is given by the following:

$$\ell_{g,d} = \ell_{g,c}\left(\frac{L_{P,c}}{L_{P,d}}\right) - \gamma\left(1 - \frac{L_{P,c}}{L_{P,d}}\right) \tag{4.10}$$

where we recall that $\gamma = \frac{k_g}{k} R\ln(1+h)$. Therefore, if we fix all of the parameters except for the glycocalyx thickness, we need only prescribe the value of $\ell_{g,c}$, since $L_{P,c}$ is given by (3.76) and the ratio $\dfrac{L_{P,c}}{L_{P,d}}$ is given by the relative area change calculated above. In the circular case with $R = 5$ μm, ΔA is 0.67, which upon rearranging (4.7) gives $L_{P,d} = 1.67 L_{P,c}$. Given this relation along with the control glycocalyx thickness, our model can predict the required decrease in glycocalyx thickness to produce the given change in area.

We can investigate the behaviour of $\ell_{g,d}$ for the limiting cases mentioned at the end of the previous section. First, dividing through Eq. (4.10) by $\ell_{g,c}$, then looking at the limit in which the glycocalyx is the dominant resistance to flow, that is when $\Gamma = \dfrac{\gamma}{\ell_{g,c}} \ll 1$, we obtain

$$\frac{\ell_{g,d}}{\ell_{g,c}} = \frac{L_{P,c}}{L_{P,d}} \tag{4.11}$$

where we note that Γ is defined in terms of the control glycocalyx thickness. This equation implies that the relative increase in L_P must be accompanied by a corresponding relative decrease of the same magnitude in ℓ_g. This makes sense intuitively, since if the glycocalyx is the dominant resistance, the capillary wall (hence k) essentially has no effect, and since in addition k_g is constant, the only way L_P could increase would be via changes in ℓ_g.

If we instead divide Eq. (4.10) by γ, then we can look at the limiting case of a glycocalyx that provides little resistance, namely when $\Gamma \gg 1$. However, the deteriorated glycocalyx will have a thickness less than that of the control, so $\ell_{g,d}$ will also be small compared to γ, and we are left with only $\dfrac{L_{P,c}}{L_{P,d}} = 1$. The fact that the capillary wall is the major resistance to flow means that glycocalyx degradation will have no effect on L_P, and since k is constant, there is no possibility of L_P changing.

Predictions of $\ell_{g,d}$ from Eq. (4.10) in the current case where the glycocalyx thickness is the only variable parameter are shown in Table 4.1. These entries give us information regarding the effects of the control values of glycocalyx thickness and permeability. When $\ell_{g,c}$ is 182 nm for instance, the lower value of k_g gives a predicted $\ell_{g,d}$ of 81 nm whereas with the higher permeability we predict a value of 28 nm. This is because a more permeable glycocalyx accounts for less of the total resistance to flow, such that decreases in glycocalyx thickness will not have as large of an effect on the amount of flow. Since we fix the relative increase in area and hence the ratio $\dfrac{L_{P,c}}{L_{P,d}}$, this implies that in the case of higher permeability, decreases in glycocalyx thickness of a larger magnitude would be necessary.

The last column of Table 4.1 shows the values of the dimensionless parameter Γ. For the case when $\ell_{g,c}$ is 182 nm, Γ is 0.38 for the lower permeability and 1.11 for the higher permeability, which corresponds to the discussion in the previous paragraph. For an $\ell_{g,c}$ of 400 nm, we obtain 0.17 and 0.51 for k_g values of 3.16 nm^2 and 9.24 nm^2, respectively. For the smallest value of Γ, we can compare the value of $\ell_{g,d}$ obtained from Eq. (4.10) to the approximation in Eq. (4.11) of the $\Gamma \ll 1$ limit. The approximation gives an $\ell_{g,d}$ of 240 nm, whereas the value in the table is 211

nm. Therefore, although the approximation is fair, a value of 0.17 for Γ is certainly not sufficiently small that the effect of the capillary wall can be disregarded.

Looking at the entries with the same k_g values, we can gauge the effects of the control glycocalyx thickness. This is best seen not through the absolute magnitudes of $\ell_{g,d}$, but by the percentage decrease. For $k_g = 3.16$ nm^2 and $\ell_{g,c} = 182$ nm, $\ell_{g,d}$ is predicted to drop to about 45% of its control value. When $\ell_{g,c}$ is 400 nm, $\ell_{g,d}$ is still above 50% of its control value. Since the glycocalyx contributes more to the overall flow resistance for larger values of $\ell_{g,c}$, glycocalyx degradation will have a more pronounced effect on fluid flow when $\ell_{g,c}$ is larger. So, to produce the same relative increase in L_P, the magnitude of the decrease in glycocalyx thickness required is lower. We expand upon these results in Section 4.3.3, where distributions have been used to make a more accurate representation of the data, and we have calculated statistics of $\ell_{g,d}$.

Table 4.1: Predicted values of $\ell_{g,d}$ for different values of control glycocalyx thickness and permeability, from Eq. (4.10). All other parameters are from Table 3.1.

$\ell_{g,c}$ (nm)	k_g (nm^2)	Predicted $\ell_{g,d}$ (nm)	Γ
182	3.16	81	0.38
	9.24	28	1.11
400	3.16	211	0.17
	9.24	158	0.51

Changes in permeability

Although there are no data available, one would expect that upon enzymatic degradation, there may be structural changes in the glycocalyx, for example alteration of pore size or spacing. In our model this is quite simply represented as an increase in the glycocalyx permeability k_g. Shown in Table 4.2 are our predicted increases in L_P upon enzymatic degradation of the glycocalyx for different parameter values. We take the ℓ_g values as in van den Berg et al. (2003) for the control and hyaluronidase-treated cases. We take for the values of $k_{g,c}$ those suggested in Weinbaum et al. (2003) and also the value used in Zhang et al. (2006a). Under hyaluronidase treatment, we allow $k_{g,d}$, the permeability in the glycocalyx-degraded case, to take either its control value, 1.5 times its control, or twice its control value. We perform all calculations for three different values of the capillary wall permeability, k.

Table 4.2: Percentage increase in L_P upon glycocalyx degradation. Note we are using the data from van den Berg et al. (2003) for control and degraded glycocalyx values of ℓ_g, respectively 182 nm and 77 nm.

		k=8	k=17	k=21.8
$k_{g,c}$ (nm^2)	$k_{g,d}$ (nm^2)	% increase in L_P		
3.16	$k_{g,c}$	40	63	72
	1.5 $k_{g,c}$	54	93	108
	2 $k_{g,c}$	63	113	133
9.24	$k_{g,c}$	17	31	38
	1.5 $k_{g,c}$	22	42	52
	2 $k_{g,c}$	24	48	60

In the first row with $k = 21.8$ nm^2, we see the 72% increase referred to in the discussion above. Increasing k for fixed $k_{g,c}$ and $k_{g,d}$ gives a larger percentage increase in L_P due to the fact that a higher capillary wall permeability will result in the glycocalyx providing more of the total resistance; hence its degradation will have a larger impact. Table 4.3 shows the values of Γ for different parameter combinations. Note that the definition of Γ is always in terms of the control values of the parameters, namely

$$\Gamma = \frac{k_{g,c}}{k_c}\frac{\Delta R}{\ell_{g,c}}\frac{\ln(1+h)}{h} \tag{4.12}$$

For increasing values of k with $k_{g,c} = 3.16$ nm^2 and $\ell_{g,c} = 182$ nm, Γ is 1.03, 0.49 and 0.38, respectively. For the same glycocalyx thickness with $k_{g,c} = 9.24$ nm^2, the values are 3.02, 1.42 and 1.11. The parameter combination corresponding to the lowest resistance glycocalyx gives a value of $\Gamma = 3.02$. In this case, our predicted increase in L_P is 17%, which is not too far off of the approximation in the $\Gamma \gg 1$ limit, where $L_{P,c} = L_{P,d}$. However, the value of Γ is not sufficiently large so that we may neglect effects of the glycocalyx altogether.

Increasing $k_{g,d}$ for fixed $k_{g,c}$ and k will also give larger percentage increases in L_P, as expected intuitively. For fixed k and $k_{g,c}$:$k_{g,d}$ ratio, a larger value of $k_{g,c}$ implies a smaller percentage increase in L_P. A larger control value of glycocalyx permeability means that the glycocalyx will provide less resistance to flow, which results in a smaller relative effect on L_P upon degradation.

Table 4.2 may serve as a guide when further experiments are performed and the values of k_g, k, ℓ_g, or the percentage increase in fluid in the pericapillary space,

Table 4.3: Value of Γ for different parameter combinations.

		k=8	k=17	k=21.8
$\ell_{g,c}$ (nm)	$k_{g,c}$ (nm^2)		Γ	
182	3.16	1.03	0.49	0.38
	9.24	3.02	1.42	1.11
400	3.16	0.47	0.22	0.17
	9.24	1.38	0.65	0.51

are measured or better estimated. For instance, if it is found that the control k_g is approximately 9.24 nm^2 and k=21.8 nm^2, then if the ℓ_g values before and after hyaluronidase treatment remain as above, Table 4.2 predicts a 60% increase in L_P for $k_{g,d} = 2k_{g,c}$. In this sense our model could be used as a predictive tool to project that a more than two-fold increase in k_g would be required upon glycocalyx degradation to match our calculations for the relative change in area in Figure 4.2.

Under enzyme treatments not only may the glycocalyx properties change, but there may also be changes in the endothelial monolayer. This may destabilize endothelial junctions and lead to contraction of endothelial cells such that there is increased permeability. To represent these changes in our model is not difficult, as the structural changes are simply reflected by changes in the value of the capillary wall permeability, k. This is a great advantage of using the poroelastic approach, namely that by treating the capillary wall as a homogenized material, there is a single parameter, k, which determines the resistance to flow through the capillary wall. This lumped parameter takes into account the individual resistances of the tight junction, crossbridging molecules in the cleft, etc. By contrast, in the ultrastructural models of Hu and Weinbaum (1999) and Adamson et al. (2004), the above changes would result in new values for several parameters, for example the dimension of the breaks in the junction strand, the average distance between breaks, and the cleft length per unit area of capillary wall. The measurements of these parameters are presumably difficult, so measuring them in the setting of enzymatic degradation will likely give rise to large uncertainties in the values. Homogenization, while a considerable simplification, allows for investigation of these effects by changing only one parameter.

In Table 4.4, we show the percentage increase in L_P for increases in the capillary wall permeability. This is similar to Table 4.2, in that we assume the glycocalyx thickness decreases from 182 nm to 77 nm as a result of some enzymatic treatment.

For now we assume that the glycocalyx permeability stays constant, so as to examine the effect of changing k only. It is seen from the data that increases in wall permeability of 50% and 100% from the control value greatly impacts the value of L_P. As in the case of changing glycocalyx permeability, if any of the parameters were to be measured, this table could be used to give estimates of k or k_g.

Table 4.4: Percentage increase in L_P upon increase in capillary wall permeability. Note we are using the data from van den Berg et al. (2003) for control and degraded glycocalyx values of ℓ_g, respectively 182 nm and 77 nm. We assume that k_g remains constant to isolate the effects of changes in k. Note that we show only the case when k_c=21.8 nm^2.

	$k_d = k_c$	$k_d = 1.5k_c$	$k_d = 2k_c$
$k_{g,c}$ (nm^2)	% increase in L_P		
3.16	72	104	125
9.24	38	81	116

Earlier, we were able to predict the decrease in glycocalyx thickness given the relative area change for the case where k_g and k remained constant. We now carry out a similar calculation in the case where k_g and k may change upon enzymatic treatment. We use the equations (4.8) and (4.9) and take their term by term ratio. Rearranging to solve for $\ell_{g,d}$ in terms of the other parameters gives

$$\ell_{g,d} = \left(\frac{k_{g,d}}{k_{g,c}}\right)\left[\ell_{g,c}\left(\frac{L_{P,c}}{L_{P,d}}\right) - \gamma\left(\frac{k_c}{k_d} - \frac{L_{P,c}}{L_{P,d}}\right)\right] \tag{4.13}$$

where $\gamma = \dfrac{k_{g,c}}{k_c} R\ln(1+h)$ is now defined in terms of the control variables. We can examine the two limiting cases, namely where the glycocalyx is the dominant resistance to flow, and where the glycocalyx provides little resistance as compared to the capillary wall. Dividing Eq. (4.13) by $\ell_{g,c}$, and looking at the case when $\Gamma \ll 1$, we obtain the relation

$$\frac{\ell_{g,d}}{\ell_{g,c}} = \left(\frac{k_{g,d}}{k_{g,c}}\right)\left(\frac{L_{P,c}}{L_{P,d}}\right) \tag{4.14}$$

as we might expect intuitively. The glycocalyx is the main resistance to flow, so changes in ℓ_g or k_g will affect L_P, whereas changes in k will not. An increase in L_P by a factor of two could be as a result of a reduction in glycocalyx thickness by a half with permeability remaining constant, a doubling of the permeability with thickness constant, or some combination where both parameters change.

In the limit when the glycocalyx produces no resistance to flow, that is when $\Gamma \gg 1$, we divide Eq. (4.13) by γ, again noting that $\ell_{g,d}$ will be much smaller than

γ, and we thus obtain

$$\frac{L_{P,c}}{L_{P,d}} = \frac{k_c}{k_d}$$

which implies that changes in hydraulic conductivity are due only to changes in the capillary wall permeability.

Table 4.5 shows the predicted values of $\ell_{g,d}$ based on Eq. (4.13). For now we show only the case when $\ell_{g,c} = 182$ nm and $k_{g,c} = 3.16$ nm^2. We can ascertain the effect of an increase in either glycocalyx or capillary wall permeability by comparing the first row to the subsequent four rows. In each case, it is observed that if $k_{g,d}$ or k_d increases, the value of $\ell_{g,d}$ increases as well. In other words, the decrease in glycocalyx thickness from the control value is of a smaller magnitude if the glycocalyx permeability or capillary wall permeability increases with enzymatic treatment. Precisely which of $k_{g,d}$ or k_d has more of an effect depends on the parameters such as the control glycocalyx thickness and permeability. For example, looking at the third and fifth rows, we see that the glycocalyx thickness is required to drop to 116 nm (from 182 nm) when the capillary wall permeability increases two-fold, whereas it only drops to 162 nm if the glycocalyx permeability doubles. Therefore, for this particular parameter combination, increasing $k_{g,d}$ has a more prominent effect on flow through the capillary wall than does increasing k_d by the same relative magnitude, such that the required decrease in glycocalyx thickness is smaller when glycocalyx permeability increases. We will expand upon these results in Section 4.3.3.

Table 4.5: Predicted values of $\ell_{g,d}$ when values of glycocalyx and capillary wall permeability change upon enzymatic treatment, from Eq. (4.13). $\ell_{g,c} = 182$ nm, $k_{g,c} = 3.16$ nm^2 and $k_c = 21.8$ nm^2.

$k_{g,d}$ (nm^2)	k_d (nm^2)	Predicted $\ell_{g,d}$ (nm)
$k_{g,c}$	k_c	81
$k_{g,c}$	1.5 k_c	104
$k_{g,c}$	2 k_c	116
1.5 $k_{g,c}$	k_c	121
2 $k_{g,c}$	k_c	162

Changes in reflection coefficient

The structural changes in the glycocalyx that may lead to an altered k_g may also cause a change in the value of the glycocalyx reflection coefficient, σ_g. As men-

tioned, no study of which we are aware measures changes in the reflection coefficient under enzymatic degradation; however the following studies may at least shed some light on changes in the value of the reflection coefficient under other experimental conditions. It is noted that the authors of the works discussed here refer to the reflection coefficient as σ; however the 'new view', as reflected in the Michel-Weinbaum hypothesis, identifies the glycocalyx as the osmotic barrier, and thus the glycocalyx reflection coefficient which we call σ_g corresponds to the σ from these papers. In subsequent sections, all references to σ are to our capillary wall reflection coefficient.

Michel and Phillips (1985) measured changes in L_P and the effective osmotic pressure $\sigma\Delta\pi$ after perfusion of Ringer solutions containing Ficoll 70 with bovine serum albumin (BSA) or cationised ferritin (CF). With either molecule present in the perfusate, there was an increase in $\sigma\Delta\pi$ and decrease in L_P compared to the control with Ficoll 70 only. Since the addition of either BSA or CF did not appreciably change the *in vitro* osmotic pressures, it was concluded that the increase in $\sigma\Delta\pi$ took place due to an increase in the value of σ for Ficoll 70. Mason et al. (1977) and Curry et al. (1987) similarly showed that increases in L_P were accompanied by decreases in $\sigma\Delta\pi$ upon perfusion with protein-free solutions, which were attributed to changes in the properties of the molecular sieve. These experiments point to a change in the value of the reflection coefficient when the hydraulic permeability changes. However, there is also some evidence to the contrary. Clough et al. (1988) sought to determine changes in L_P and $\sigma\Delta\pi$ after tissue temperature had been raised to create an inflammatory state. In some vessels, the rise in L_P was accompanied by a drop in $\sigma\Delta\pi$, in accordance with the observations of Mason et al. (1977), Michel and Phillips (1985), and Curry et al. (1987). However, in other vessels L_P increased as much as 15-fold with no corresponding change in $\sigma\Delta\pi$. Thus the permeability had increased in regions that retained the selectivity of undamaged vessels. This evidence would seemingly point to the reflection coefficient retaining its value even with changes in L_P. It would clearly be of interest to measure how the glycocalyx reflection coefficient changes for various glycocalyx-degrading substances, such as hyaluronidase, heparinase and pronase.

We cannot be sure whether or not changes in σ_g have indeed taken place in the study of van den Berg et al. (2003), or if they have, what the magnitude of these changes are. However, we have carried out simulations to study the effect of varying σ_g. Although σ_g does not directly enter the expression for L_P, it does have an effect on transcapillary filtration, namely on the magnitude of the filtration flux, as can be

seen from Eq. (3.75). Figures 4.3 and 4.4 show $\frac{J_v}{A}$ as a function of capillary pressure for different values of σ_g. The effect of decreasing σ_g is to translate the line to the left, decreasing the pressure at which zero filtration occurs (that is p_c at which $\frac{J_v}{A} = 0$). For $\sigma_g = 0.9$, this pressure is approximately 17 cmH_2O. As σ_g decreases to 0.8, 0.5, and 0.2, this quantity decreases to 15, 9, and 3 cmH_2O, respectively. These values are the same regardless of the values of ℓ_g and k_g, as it is clearly seen from Eqs. (3.75) and (3.76) that ℓ_g and k_g are present in the expression for L_P, and as such determine the slope of the $\frac{J_v}{A}$ vs. p_c curve, whereas σ_g determines solely the intercept on the p_c-axis. We note here that we have disregarded the possibility that a change in the value of σ_g may cause a corresponding change in π_g, the osmotic pressure behind the glycocalyx. However, we have reason to believe that this will not change the results by an appreciable amount, the rationale for which is elaborated on now.

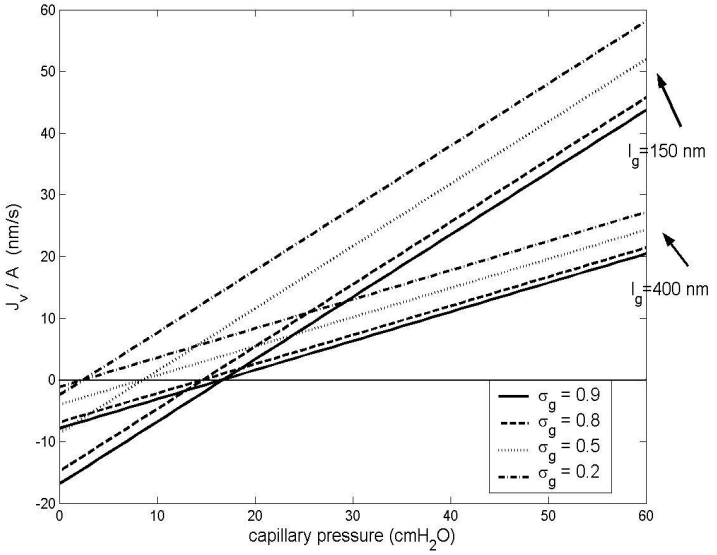

Figure 4.3: Filtration flux as a function of capillary pressure for four different values of σ_g and two values of ℓ_g (k_g has been set constant at 3.16 nm^2). Note that decreasing σ_g lowers the intercept of the curve while increasing ℓ_g decreases the slope of the line (i.e. the value of L_p).

Under high flow conditions where the permeability was increased and there was a corresponding decrease in σ_g, the value of π_g would be lowered. If, for example, we assume the reflection coefficient drops to 0.45 (half its control value), we may compare the magnitude of the term $\sigma_g(\pi_c - \pi_g) - \sigma(\pi_i - \pi_g)$ in Eq. (3.75) (since the changes affect the intercept but not the slope of the $\frac{J_v}{A}$ vs. p_c curves) for the cases when π_g is held fixed at its control value or lowered to take into

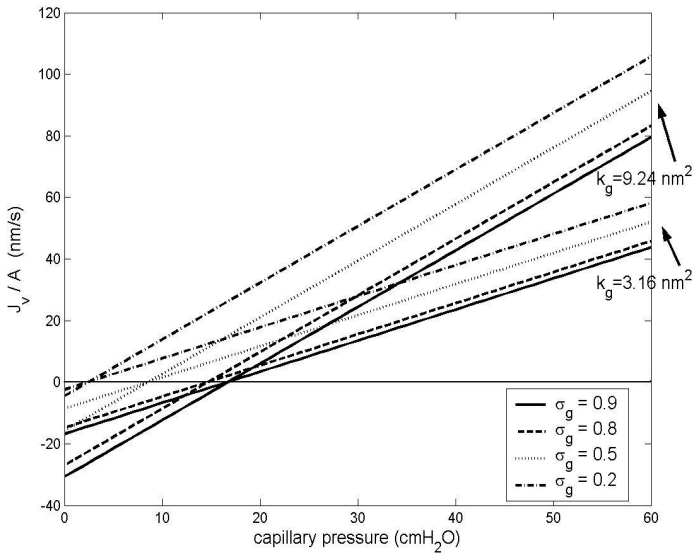

Figure 4.4: Filtration flux as a function of capillary pressure for four different values of σ_g and two values of k_g. Now ℓ_g has been set constant at 150 nm. Note again the effect of σ_g as in Figure 4.3. An increase in k_g creates a corresponding increase in the slope of the line.

account its dependence on the flow. The difference between the above term for π_g taking its value in Table 3.1 and half that value is only about 2 cmH_2O. If the decrease in π_g is 25%, the difference is only 1 cmH_2O. Since π_g is not a measurable parameter due to the extremely small scales involved, and thus must be inferred from a particular theory, we consider our approximation of a constant π_g to be reasonable and justifiable under these circumstances.

Of course not only may σ_g change, but there may also be changes in σ, the capillary wall reflection coefficient. As with our discussion of the parameter k, it is difficult to know from an ultrastructural perspective what effect enzymatic treatment may have on σ. We show in Figure 4.5 the filtration flux $\frac{J_v}{A}$ as a function of capillary pressure for a range of values for σ. The important point to note is that over the range $0 \leq \sigma \leq 0.9$, the lines are only slightly shifted, such that the pressure at which zero filtration occurs decreases by a small amount as σ increases (only 2 cmH_2O over the range of σ).

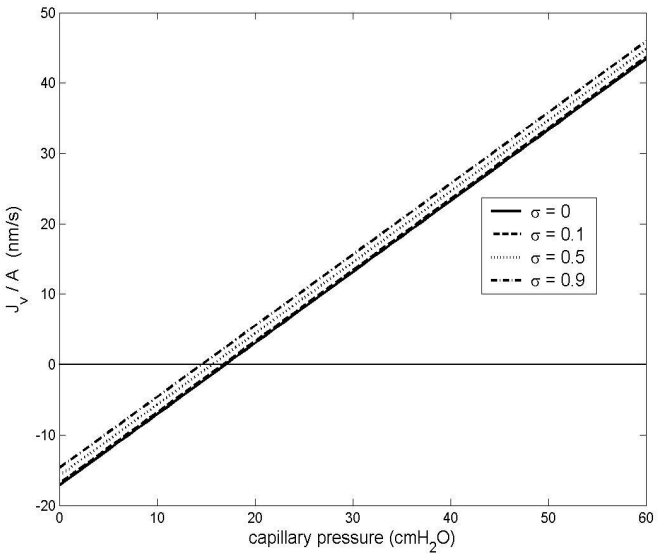

Figure 4.5: Filtration flux as a function of capillary pressure for different values of capillary wall reflection coefficient σ. Note $\ell_g = 182$ nm and $k_g = 3.16$ nm^2.

4.2.4 Comparison with other studies

We can compare our predictions for the change in L_P values upon glycocalyx degradation with some other studies in the literature. Adamson (1990) measured changes in L_P after pronase treatment to degrade the glycocalyx. The control L_P was 2.0×10^{-7} cm s^{-1} cmH$_2$O^{-1}, whereas after pronase degradation of the glycocalyx the L_P value increased to 4.9×10^{-7} cm s^{-1} cmH$_2$O^{-1}. Thus, there was approximately a 2.5-fold increase in hydraulic conductivity, leading to the conclusion that the glycocalyx accounts for approximately 60% of the resistance to flow across the capillary wall. Note that the percentage of the total resistance to flow due to the glycocalyx is calculated as

$$R_{glyc} = 1 - \frac{L_{P,c}}{L_{P,d}} \tag{4.15}$$

Therefore in the experiment of Adamson (1990), $L_{P,d} = 2.5\, L_{P,c}$, so the resistance is 0.6, or 60%. Since more recent studies (Adamson et al., 2004) indicate that the L_P value lies in the range 1.0-1.3$\times10^{-7}$ cm s^{-1} cmH$_2$O^{-1} in normal physiological situations, rather than compare the absolute changes, we compare our prediction for the relative increase in L_P upon glycocalyx degradation. For a 150 nm glycocalyx (as suggested by Adamson et al., 2004), we predict $L_P = 1.01 \times 10^{-7}$ cm s^{-1} cmH$_2$O^{-1}, whereas in the limit as the thickness goes to zero (as seen in Eq. (4.5)), L_P increases to 3.20×10^{-7} cm s^{-1} cmH$_2$O^{-1}. This implies that with the parameter

values in Table 3.1 the glycocalyx is responsible for 68% of flow resistance. If instead we assume a control ℓ_g value of 104 nm (corresponding to $L_P = 1.28\times10^{-7}$ cm s^{-1} cmH_2O^{-1}), then elimination of the glycocalyx gives the same 2.5-fold increase in L_P as in Adamson (1990). We note that Smith et al. (2003) estimate the glycocalyx thickness in vivo to be 400-500 nm, whereas here we use a smaller value. Below we consider values of ℓ_g in this range when calculating the percentage resistance to flow due to the glycocalyx (see Table 4.6).

A relevant question that arises is whether in Adamson's experiments the glycocalyx was totally eliminated or degraded but still present. If still present, then did for instance its permeability change, and by how much? These are important issues in understanding how much of the total resistance to flow is due to the glycocalyx. In the absence of data to resolve these questions, our model can be used to investigate parameter combinations that best fit the observations.

Further comparison of our model predictions can be made with the results of Zhang et al. (2006a), who show a plot of L_P as a function of glycocalyx thickness (Fig. 4.6). First, examining the left side of Figure 4.7, we show our prediction of L_P as a function of ℓ_g for three different values of glycocalyx permeability (namely the value suggested in Weinbaum et al., 2003, that used in Zhang et al., 2006a, and another nominal value) and two values of the capillary wall permeability. In examining the solid curves, we note that our estimate of L_P is higher than that of Zhang et al. for values of ℓ_g close to zero, for all k_g. As ℓ_g increases to 50-100 nm, the curve of Zhang et al. falls between our low and medium k_g solid curves, and above $\ell_g = 100$ nm, their predicted behaviour is quite similar to our model predictions in the medium permeability case. The larger predicted L_P values at low ℓ_g arise as a result of our choice of parameter values. The permeability of the capillary wall, k, is estimated based on measurements of the cleft-spanning structures cited in Adamson et al. (2004). Treating k as an adjustable parameter, we observe from Figure 4.7 that k determines the intercept of the L_P vs. ℓ_g curve, whereas k_g determines the curvature. To ensure L_P is the same as the value in Zhang et al. for $\ell_g = 0$, we use the value $k = 17$ nm^2, and when $k_g = 9.24$ nm^2 our result is very close to that of Zhang et al. for all values of ℓ_g.

Sugihara-Seki et al. (2008) modeled the three-dimensional flow through the microvascular wall using a Brinkman equation (the Stokes equation with an added term proportional to the velocity which represents the Darcy force) to account for the fiber matrices in the glycocalyx and cleft regions. A model of this type requires prescription of the permeabilities of the glycocalyx and cleft, which play

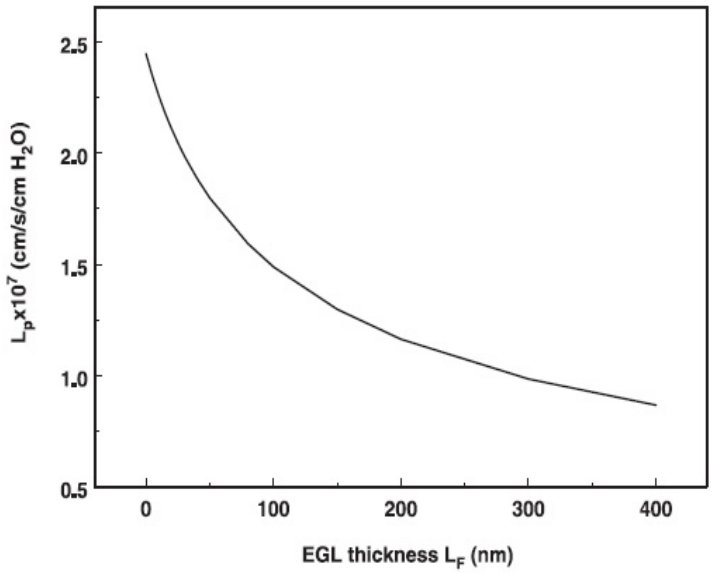

Figure 4.6: Zhang et al. (2006a) model prediction for L_P as a function of glycocalyx thickness.

roles similar to k_g and k in our model. The authors do not take any account of plasma proteins, and instead look at the transcapillary flow from a purely fluid mechanical point of view. They compute the fluid streamlines, pressure profiles and shear stress distribution in the cleft and glycocalyx regions. Also, using parameter values from Adamson et al. (2004), they were able to make predictions about the behaviour of L_P as the glycocalyx thickness is varied. In Figure 4.8 we show their plot of L_P as a function of ℓ_g for the separate cases of the presence or absence of cleft-spanning molecules. Note that the absence of these molecules corresponds to an infinite permeability - thus we can only compare to the case in which the molecules are present.

With cleft-spanning molecules present, their prediction of L_P for a glycocalyx thickness of 150 nm matches our prediction; however, variations of L_P with changes in ℓ_g differ markedly between the two models. In fact, L_P changes very little over the range of $0 \leq \ell_g \leq 1000$ nm, leading Sugihara-Seki et al. (2008) to predict that the glycocalyx provides much less resistance to the flow than previously assumed. For a finite cleft permeability, the increase in L_P upon removal of the glycocalyx is only 15%, implying that the glycocalyx accounts for only about 13% of the flow resistance. This is a major discrepancy between our study and theirs. In order for our model to arrive at a similar prediction, we would need to set k to a value of approximately 8 nm^2, and assign a very large value to k_g (note that in the limit as

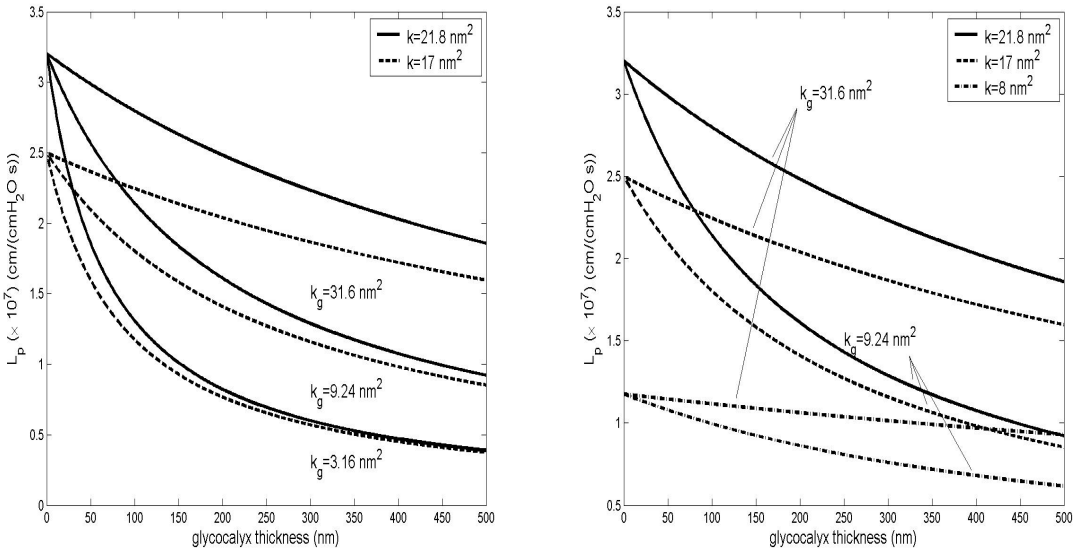

Figure 4.7: L_P as a function of ℓ_g for different values of k_g and k.

$k_g \to \infty$, L_P ceases to depend on ℓ_g – see Eq. (4.5)). This is seen in the dash-dot curve with $k_g = 31.6$ nm^2 on the right side of Figure 4.7.

Since in the study of Sugihara-Seki et al., there is not much variation of L_p with ℓ_g, there is a only a weak dependence of the percentage resistance due to the glycocalyx on the value of the control ℓ_g. In contrast, our model has a much stronger dependence on the choice of the control value for ℓ_g. We use our expression for the resistance due to the glycocalyx (4.15) along with our expression for the limit of L_P as $\ell_g \to 0$, namely (4.5). Table 4.6 shows the results for different values of the parameters. As mentioned above, it is quite possible that k_g changes with degradation, and one could make inferences based on Tables 4.2 and 4.6. But also note that taking the limit as $\ell_g \to 0$ is equivalent to taking the limit as $k_g \to \infty$, as seen in Eq. (4.5).

Clearly as the wall becomes more permeable (k increasing) with the other parameters fixed, the wall is less of a resistance to flow, and Γ decreases toward the high resistance limit of the glycocalyx. For k_g and k fixed, increasing the glycocalyx thickness means an increase in Γ, such that the glycocalyx provides more resistance to flow. For ℓ_g and k fixed, increasing k_g implies that the resistance due to the glycocalyx is lower, as one would expect intuitively, and the value of Γ correspondingly increases. One may compare the trends in Table 4.6 to those in Table 4.3, and note that the smallest values of Γ correspond to the largest values of R_{glyc}.

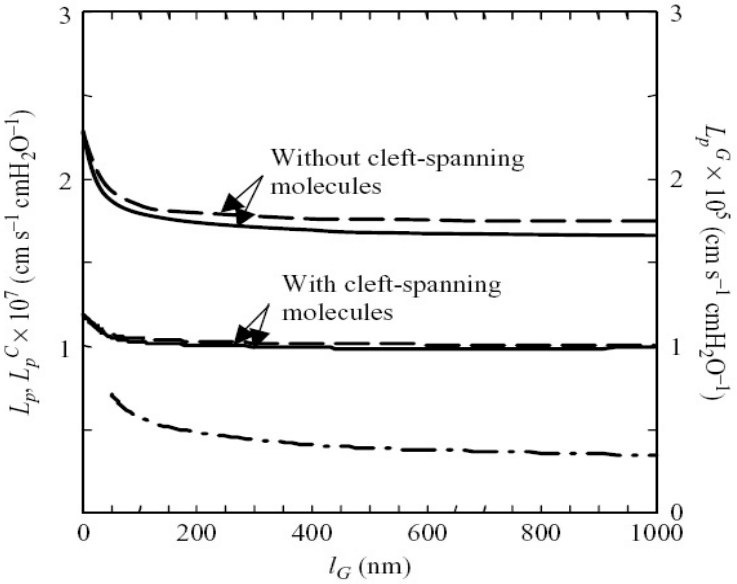

Figure 4.8: Sugihara-Seki et al. (2008) model prediction for L_P as a function of glycocalyx thickness. Reprinted with permission. ©Cambridge Journals.

Certainly with better experimental estimates of any or all of the parameters k_g, k, ℓ_g, or with better experimental estimates of the resistance to flow due to the glycocalyx, Table 4.6 may be directly checked against the experimental results, or used to give estimates of the unknown parameter values. For instance, if the known values of k_g and k were 9.24 nm^2 and 21.8 nm^2 respectively, and the estimate of the glycocalyx accounting for 60% of the resistance from Adamson (1990) were identically correct, our model would predict that the control glycocalyx thickness would be below 400 nm, but closer to 400 nm than 150 nm. If the resistance was closer to 50%, as suggested more recently by Adamson et al. (2004), the glycocalyx dimension would again be between 150 and 400 nm, but this time closer to 150 nm. Or, if R_{glyc} (4.15) were known to be 60% and the glycocalyx thickness was measured at 400 nm, this table could be used to estimate both the parameters k_g and k, as follows: if k_g were thought to be 3.16 nm^2, then k would have to be less than 8 nm^2. If this value of k was known to be too low, then according to our calculations, k_g would have to be larger.

4.2.5 Discussion

The objective of our model was to describe transcapillary flow in a more accessible manner than the three-dimensional ultrastructural model of Hu and Weinbaum

Table 4.6: Percentage resistance due to the glycocalyx for different values of the three parameters ℓ_g, k_g and k.

		k=8	k=17	k=21.8
ℓ_g (nm)	k_g (nm^2)	R_{glyc}		
150	3.16	45	63	68
	9.24	22	37	43
400	3.16	68	82	85
	9.24	42	61	66

(1999), without losing the essential predictive capabilities. In fact, this appears to have been also the motivating purpose for Zhang et al. (2006a), in formulating their simplified one-dimensional model. A major advantage of Zhang et al. (2006a) when compared to our model is their ability to generate much more intricate albumin concentration profiles. This is achieved by their splitting of the domain into five regions, each governed by a convection-diffusion equation subject to matching conditions. This enables the generation of nonlinear $\frac{J_v}{A}$ vs. p_c curves that are in good agreement with the experimental data of Adamson et al. (2004). Their model also predicts steady-state reabsorption under certain conditions, a phenomenon not yet observed experimentally, and is able to account for vesicular transport.

To describe albumin (or any plasma protein) in our model, we bypassed the use of convection-diffusion equations and instead derived an equation satisfied by the osmotic pressure field, $\pi(r)$. By truncating the series solution for π, we obtain a simple expression which does not depend on the capillary pressure, thus the behaviour of π (and hence the albumin concentration) remains the same under different flow conditions. In reality, the flow is coupled to the osmotic pressure below the glycocalyx, π_g, and we set π_g constant, as per the discussion above.

Both our model and the others discussed have their relative advantages depending on the problem at hand. If an experiment is performed in which tissue is backloaded at a high albumin concentration, and what is required are detailed albumin concentration profiles and/or $\frac{J_v}{A}$ vs. p_c curves, then clearly the model of Zhang et al. (2006a) will be preferable. If the velocity profiles and shear stress distributions in the glycocalyx and cleft are of interest, then the work of Sugihara-Seki et al. (2008) will be more pertinent. However, it is our contention that if the question to be addressed deals with glycocalyx degradation and its effect on fluid balance, our model is most accessible due to the relationship of L_P, a measurable quantity, with the parameters of the glycocalyx, namely k_g and ℓ_g.

In fact, we have shown above that our model can reproduce the L_P vs. ℓ_g curves predicted by both the models of Zhang et al. (2006a) and Sugihara-Seki et al. (2008) by selecting appropriate values for the parameters k_g and k. For Zhang et al. (2006a), values of $k_g = 9.24$ nm^2 and $k = 17$ nm^2 are required, whereas for Sugihara-Seki et al. (2008), $k_g = 31.6$ nm^2 and $k = 8$ nm^2 match their prediction quite well. Therefore, our simpler model, with its closed-form expressions for all variables including L_P, can describe a wide range of behaviours. Examination of two of our curves in Figure 4.7 show the markedly different situations which our model can capture with appropriate parameter values. In the left graph, the curve with $k_g = 3.16$ nm^2 and $k = 21.8$ nm^2 corresponds to the limit of a high-resistance glycocalyx, and it is observed that for small values of ℓ_g, there are large changes in L_P with changes in ℓ_g. In the right graph, the curve that fits Sugihara-Seki et al. (2008) corresponds to the limit of a low-resistance glycocalyx, and the value of ℓ_g has only a small effect on L_P. This may be important when used in conjunction with experimental data.

For example, if an experiment were performed in which L_P could be measured for several values of the glycocalyx thickness, then our model would give estimates of the glycocalyx permeability and capillary wall permeability. If L_P were measured for a completely abolished glycocalyx ($\ell_g = 0$), then the intercept of the L_P vs. ℓ_g curve would give an estimate of k and a curve fit would yield an approximation of k_g. Given the ingenuity and creativity of experimentalists in this field and the rapidly evolving technological capabilities, we feel confident that these types of measurements and experimental data will become available in the near future. We know L_P can be measured using the Landis technique (Michel et al., 1974). There are currently three methods to estimate the glycocalyx thickness; however each has associated drawbacks (Broekhuizen et al., 2009). As for k_g and k, we have estimated these using the theory in Weinbaum et al. (2003) and parameters from Adamson et al. (2004), but neither of these parameters has been directly measured.

Given knowledge of some parameters, we may use the model to estimate other parameter values bearing certain criteria in mind. First, according to Zhang et al. (2006a) and Adamson et al. (2004), control L_P should be between 1.0-1.3$\times 10^{-7}$ cm s^{-1} cmH_2O^{-1}. Next, there should be some agreement with van den Berg et al. (2003) for the change in fluid content in the pericapillary space upon deterioration of the glycocalyx. Here, measurements of the PSD as well as ℓ_g are required. Calculation of the relative area change can be carried out using our crude method of approximating capillary cross-sections as circular or elliptic, or by a more refined

method of looking pixel by pixel at an electron microscope image (e.g. Figure 4.1). Also, rather than taking only the median values of ℓ_g and the PSD from van den Berg et al. (2003), one could utilize a larger subset of their data, and perform a statistical analysis. This is precisely what we attempt to do in the following section.

Finally, the percentage resistance to flow due to the glycocalyx needs to be characterised by experimental observations. However, this represents a challenge as there is no method of direct measurement, so the results must be inferred from particular experimental data. Adamson (1990) approximates this as 60%, but in the discussion of Sugihara-Seki et al. (2008), they cite unpublished data in which L_P increases by 38% using heparinase treatment, or 260% using pronase treatment. This implies that the respective resistances are 28% and 72% respectively. It is likely that the glycocalyx is not totally eliminated as a result of heparinase treatment, so this value of 28% is probably too low. Using a wide range of parameter combinations, our model predicts values in the range of 22% to 85%, as seen in Table 4.6. We have also identified the parameter Γ, which is a measure of the relative resistances of the capillary wall and glycocalyx. Therefore, given experimental data of L_P as a function of ℓ_g along with the control glycocalyx thickness, Γ could be estimated and hence the relative resistance due to the glycocalyx would be known. Further experimental results are clearly required to definitively resolve this question.

4.3 Using probability distributions to represent the data

4.3.1 Expressing the histograms of van den Berg et al. as probablility distributions

Previously, we used the median values for pericapillary space dimension (PSD) in the control and hyaluronidase-treated cases to calculate the area change relative to the baseline that occurs as a result of hyaluronidase treatment. However, as can be seen from the histograms in Figure 4.9, there is quite significant variation in the data and we therefore attempt to make a more rigorous study using all of the available data. Our goal is to convert the histograms in Figure 4.9 to probability distributions, namely the χ^2 distribution. An advantage of using the χ^2 distribution

is that it has only one parameter, namely the degrees of freedom, k. This makes our calculations to find the distribution of best fit fairly straightforward. In the usual application of hypothesis testing, the value of k takes an integer value based on the problem at hand. In our case, since we are looking for the best fit to the data, we allow k to take non-integer values. We discuss in more depth the assumption of using the χ^2 distribution at the end of this section. For some background such as the probability density function and cumulative distribution function, the reader is referred to the Appendix.

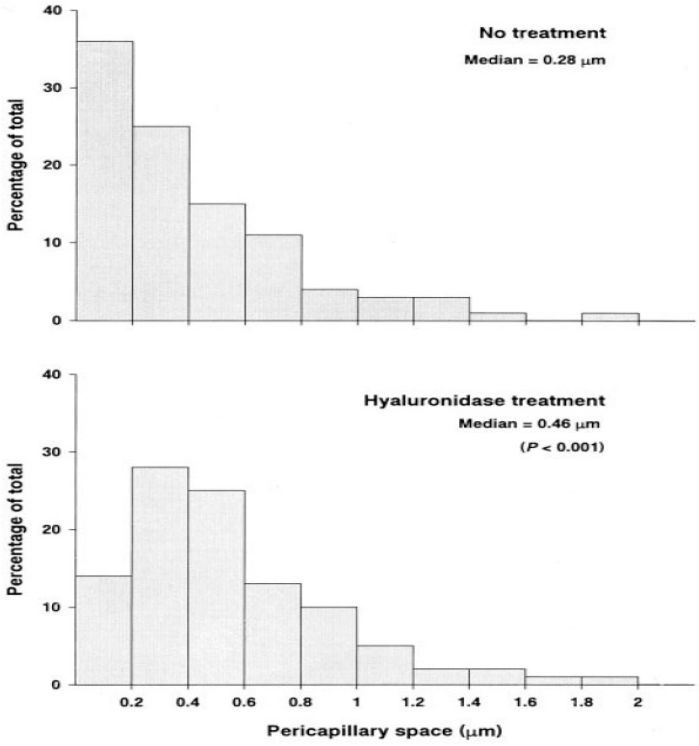

Figure 4.9: Histograms from van den Berg et al. for the pericapillary space dimension (PSD). Reprinted with permission.

Table 4.7: Estimated percentage in each interval in the histograms of van den Berg et al.

PSD (μm)	0.2	0.4	0.6	0.8	1.0	1.2	1.4	1.6	1.8	2
control	36	25	15	11	4	3	3	1	0	1
hyaluronidase	14	28	25	13	10	5	2	2	1	1

Table 4.7 shows our estimated values for the height of each bar in Figure 4.9. Note the values add up to 99% and 101% in the top and bottom row, respectively, but these are our best estimates. Now, the only statistics given in van den Berg et al. (2003) are the medians of the PSD measurements in the control and

hyaluronidase-treated cases, and therefore these will be be integral in our calculation. Let them be called $R_{c,m}$ and $R_{h,m}$, where subscripts c and h refer to control and hyaluronidase-treated, respectively, and m refers to the median. The values are $R_{c,m} = 0.28$ μm and $R_{h,m} = 0.46$ μm. We now explain the method of finding the optimal distribution, and note that a more detailed explanation is given in the Appendix.

To find the χ^2 distribution that will most accurately represent the histograms from van den Berg et al., we first generate distributions for a number of values of k and for each one determine the median value of the distribution, call it $R_{k,m}$. From this, we compute what we will term the scaling factor, which is a measure of how the x-coordinate is scaled between the dimensionless values given in a χ^2 distribution and the dimensional values of PSD as in the histograms of van den Berg et al. (2003). The scaling factors for the distribution with k degrees of freedom are

$$S_{c,k} = \frac{R_{c,m}}{R_{k,m}} \tag{4.16}$$

$$S_{h,k} = \frac{R_{h,m}}{R_{k,m}} \tag{4.17}$$

where the subscripts c and h refer to control and hyaluronidase-treated, respectively. By multiplying by the scaling factor, distributions are obtained with dimensional values on the x-coordinate axis.

At this stage we can find the optimal χ^2 distributions for each case. Consider now only the control case, but the method is identical for the hyaluronidase-treated. We first calculate the area enclosed by each distribution in each 0.2 μm segment, so that we may compare this area to the height of the histogram. Let A_i^{hist} be the area enclosed up to the ith segment of the van den Berg et al. histogram, where i runs from 1 to 10 (with $i = 1$ corresponding to a PSD between 0 and 0.2 μm, which from Table 4.7 gives $A_1^{hist} = 36$; $i = 2$ gives $A_2^{hist} = 36 + 25 = 61$, etc.). Then let A_i^k be the area enclosed in each segment of the χ^2 distribution with k degrees of freedom. We calculate the optimal distribution by finding the value of k based on a least-squares between the enclosed areas. Thus, for the kth degree of freedom, the error is

$$E_k = \sum_{i=1}^{10} (A_i^{hist} - A_i^k)^2 \tag{4.18}$$

The minimum value of E_k gives us the χ^2 distribution of best fit to the histogram.

We found the value of k to two decimal places, as the accuracy obtained is sufficient for our purposes. For the control case, we obtain $k = 1.97$, whereas in

the hyaluronidase-treated case, k is 4.73. The scaling factors are therefore $S_c = 0.2063\ \mu$m (control) and $S_h = 0.1127\ \mu$m (hyaluronidase-treated). In Figure 4.10 we show the distributions with the above degrees of freedom alongside the histograms of van den Berg et al.. For each of these distributions, we can use the scaling factors to calculate the mean and mode of the data in terms of the dimensional quantities. The mean value is 0.41 μm for the control case, and the mode clearly occurs at zero. For the hyaluronidase-treated case, the mean is 0.53 μm and the mode is 0.31 μm.

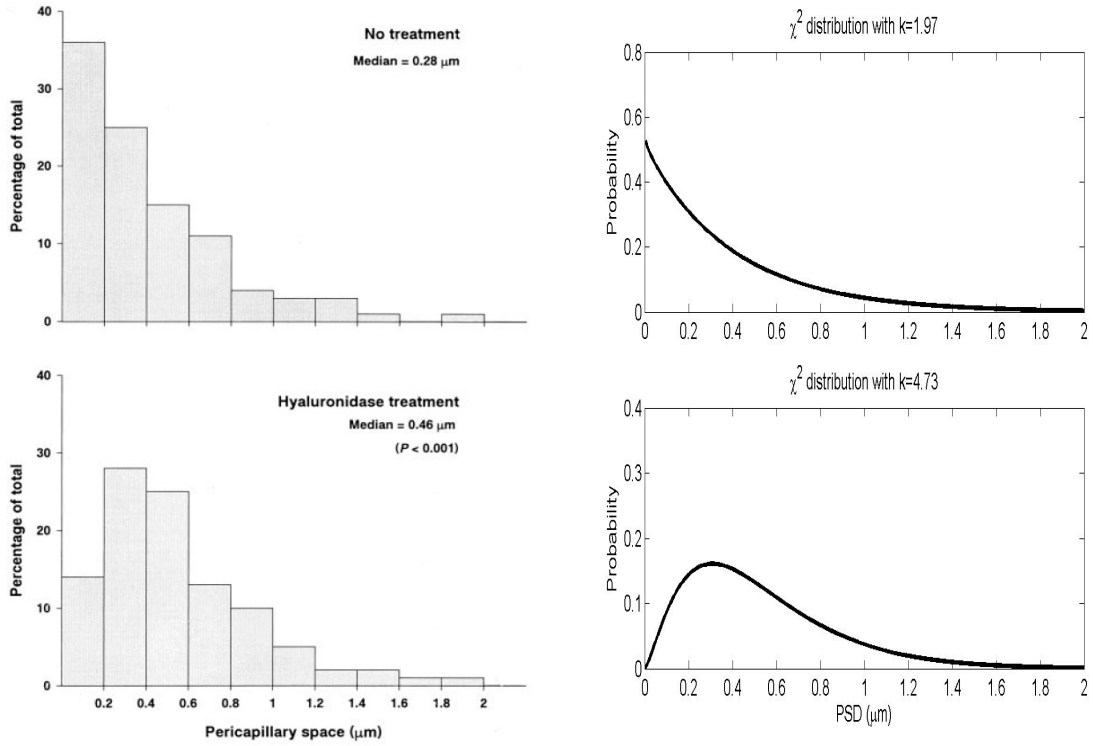

Figure 4.10: The χ^2 distributions corresponding to the histograms in van den Berg et al.. The parameter k, the degrees of freedom, is 1.97 for the control and 4.73 for the hyaluronidase-treated case.

Table 4.8 shows our calculation for the area enclosed by the distributions to the left of each 0.2 μm interval, and a comparison with van den Berg et al. We observe very good agreement in both the control and hyaluronidase-treated cases. This calculation satisfactorily displays to us that we may use the χ^2 distributions in Figure 4.10 to represent the measurements of van den Berg et al.

Table 4.8: Comparison between our estimate and the data of van den Berg et al. for area enclosed at 0.2 μm intervals

	PSD (μm)	0.2	0.4	0.6	0.8	1.0	1.2	1.4	1.6	1.8	2
control	estimate	39	63	77	86	91	95	97	98	99	99
	data	36	61	76	87	91	94	97	98	98	99
hyaluronidase	estimate	14	42	66	81	90	95	98	99	99	100
	data	14	42	67	80	90	95	97	99	100	100

4.3.2 Increase in fluid content

Having found the optimal distributions for the control and hyaluronidase-treated cases, we now aim to quantify the relative change of fluid content in the pericapillary space, or equivalently the relative change in area, using the control as a baseline value and examining the change that occurs upon hyaluronidase treatment. In Section 4.2.1, we calculated the area change for the separate cases of a circular and elliptic geometry, and had the expressions (4.2) and (4.3), which we re-write for convenience:

$$\Delta A = \frac{(R+R_h)^2 - (R+R_c)^2}{(R+R_c)^2 - R^2}$$

$$\Delta A_e = \frac{(a+R_h)(b+R_h) - (a+R_c)(b+R_c)}{(a+R_c)(b+R_c) - ab}$$

where we recall R_c and R_h are the respective pericapillary space dimensions in the control and hyaluronidase cases, R is the radius in the circular case, and a and b are the semi-minor and semi-major axes in the elliptic geometry. Previously, we set R_c and R_h equal to their median values and looked at the relative area change as a function of radius R or semi-minor and semi-major axes a and b. Here, we set R, a, and b equal to constant values, and allow R_c and R_h to be variables generated randomly from their respective χ^2 distributions. The distribution for R_c has $k = 1.97$ degrees of freedom, and that for R_h has $k = 4.73$. We use `MATLAB` to generate the distributions, with ten thousand data points for each variable. A set of ΔA values is thus obtained, and statistics of ΔA, such as the median and mean, may be calculated. But this is only a single realization, so to obtain more useful properties of ΔA, we perform one thousand realizations. For more details on this procedure, the reader is once again referred to the Appendix.

We find that the mean is not really a useful statistic in this case, due to the following example. In a single realization, one of the values given to R_c was 3.9×

$10^{-5}\mu$m, where the value of R_h was 0.65 μm. Here the relative change in area will take a value greater than 10^4, which is clearly not realistic. Since the median value is less than one, this will skew the mean to take values much larger than the median. In fact, looking at the distribution for R_c, one observes that there will be a disproportionate number of small values, and since there is no lower threshold, many values of ΔA that are not physical will be generated. We discuss this in detail in Section 4.3.4.

Table 4.9 shows the statistics that are useful, and they all utilize the median value for each realization. In performing several realizations, we compute the median, mean, maximum and minimum *of the medians from each realization.* The range of median ΔA values is 58-76% in the circular case, and are similar but slightly greater in the elliptic case. Since our model assumes a circular cylinder, we will consider only the circular geometry for the rest of this work. So based on our approximation that the χ^2 distributions calculated above adequately represent the data of van den Berg et al. (2003) for PSD, we expect that hyaluronidase treatment will increase the area of the pericapillary space relative to the control by 58-76%.

Table 4.9: Statistics of relative area change in the cases of a circular and elliptic cross-sectional geometry. All relative changes are positive and given in percentages. Note that $R = 5$ μm, $a = 2.5$ μm and $b = 5$ μm.

geometry/statistic	median	mean	maximum	minimum
circular	67	67	76	58
elliptic	68	68	77	59

Figure 4.11 shows the frequency of ΔA values for one realization in which the median value is 68%. We show two different scales to point out the fact that many of the values generated are much larger than one would expect on physical grounds. The spike on the right hand side takes into account all values greater than the largest x-value. We see from the left graph that approximately 3500 of the points have a relative area change of 2 or greater (corresponding to a 200% or larger increase), and that of these, about 1200 correspond to a 1000% or larger increase (from the right graph). These extremely large values of ΔA, which are due to the extremely small values of R_c, skew the mean, which is why it is not a useful statistic. In addition, it is observed that there are several values of ΔA that are less than zero, implying a decrease in the amount of fluid in the pericapillary spaces upon hyaluronidase treatment. This is not likely to represent the physical situation, and arises as a result of R_h taking on an extremely small value in a given

realization.

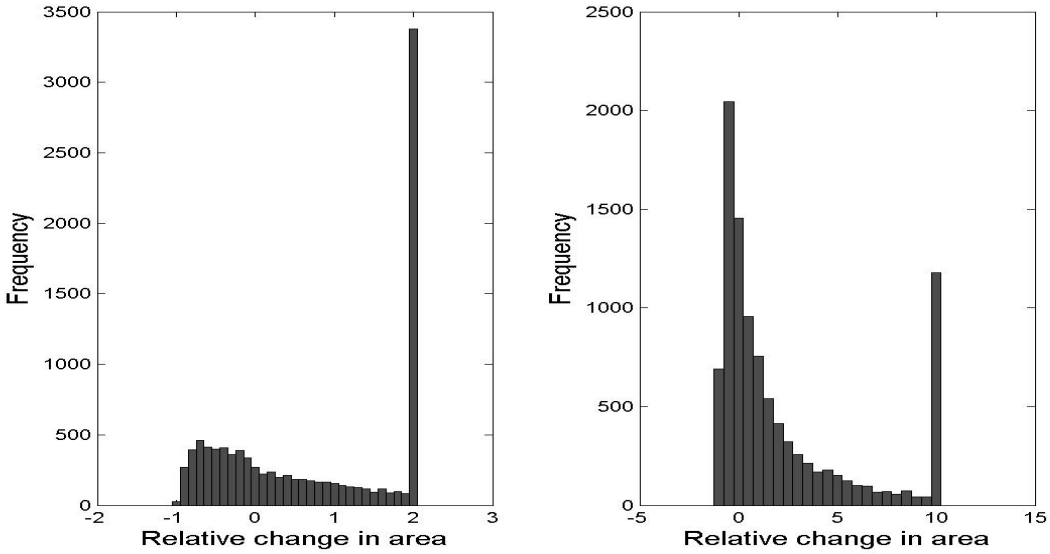

Figure 4.11: Histograms showing the frequency of the relative change in area (ΔA) in the circular case for one realization (with a median of 68%, or 0.68). Note the difference in scales on both axes. As explained in the text, the spike at the right side represents all values greater than the respective x-values. Note that $R = 5$ μm.

4.3.3 Estimation of glycocalyx thickness

The next task is to estimate the change in glycocalyx thickness given the relative area change of fluid in the pericapillary space. We use the same method as in Section 4.2.3, still using the assumption in Eq. (4.7) that the relative change in area will correspond to the relative change in hydraulic conductivity. The difference is that instead of a single value for ΔA, we now have several values which have been calculated in the previous section from the distributions for R_c and R_h. Thus we have several values for the ratio $\frac{L_{P,c}}{L_{P,d}}$, which in turn gives a number of values for $\ell_{g,d}$ based on Eq. (4.10), which we recall was for the case when glycocalyx permeability and capillary wall permeability remained constant during enzymatic treatment. This expression was

$$\ell_{g,d} = \ell_{g,c}\left(\frac{L_{P,c}}{L_{P,d}}\right) - \gamma\left(1 - \frac{L_{P,c}}{L_{P,d}}\right)$$

By performing a number of realizations, we can compute the statistical properties of $\ell_{g,d}$. Similar to the preceding section, it is found that there are anomalies due

to the use of statistical distributions to represent physical quantities. Thus there are cases when the glycocalyx thickness can have extremely large values, or even negative values. So again we find it useful to take the median of each realization, followed by taking the mean, maximum and minimum *of those medians* (note the median and mean of medians are very close, so we just show the mean). We display in Figure 4.12 a histogram that shows the frequency of these median values over the one thousand realizations.

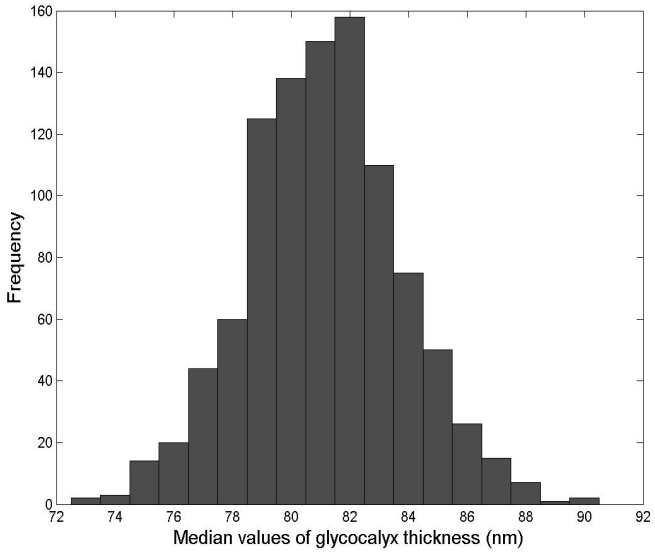

Figure 4.12: Histogram showing the frequency over all realizations of median glycocalyx thickness from each realization. $\ell_{g,c} = 182$ nm, $k_{g,c} = 3.16$ nm^2, and $k = 21.8$ nm^2.

In Figure 4.13 we show a single realization of the generated values for $\ell_{g,d}$ using the parameter values $\ell_{g,c} = 182$ nm, $k_g = 3.16$ nm^2 and $k = 21.8$ nm^2. In this realization the median value of $\ell_{g,d}$ was 81 nm. We note the two spikes in the histogram. The left spike corresponds to the fact that sometimes the relative increase in area (and hence L_P) is too large to be accounted for by changes in glycocalyx thickness only, and thus the predicted values of $\ell_{g,d}$ are less than zero, which is not physical. The right spike corresponds to the fact that some values of ΔA will be negative (i.e. L_P decreases upon hyaluronidase treatment), so large increases in ℓ_g upon glycocalyx degradation would be required to generate these values. As mentioned, this is not likely to represent the physical situation.

The mean, maximum, and minimum of the median of $\ell_{g,d}$ for each realization are shown in Tables 4.10 and 4.11. The current case in which the glycocalyx thickness is the only parameter to change is in the entries where $k_{g,d} = k_{g,c}$ and $k_d = k_c$.

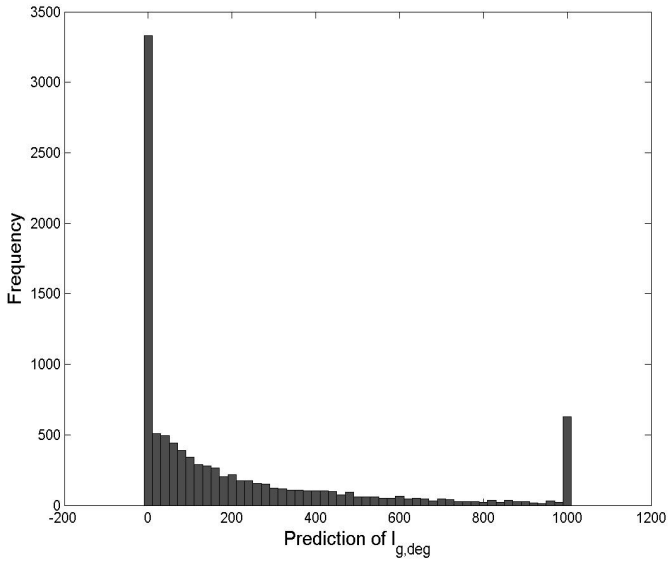

Figure 4.13: Histogram showing the frequency of different values of $\ell_{g,d}$ for one realization. Note the two spikes. The leftmost bar contains all points predicting a value of $\ell_{g,d} < 0$, which is not physical, and the rightmost bar contains all points where $\ell_{g,d} > 1000$. $\ell_{g,c}$ = 182 nm in this case, $k_g = 3.16$ nm^2 and $k = 21.8$ nm^2. The median value of $\ell_{g,d}$ was 81 nm.

The trends of how our $\ell_{g,d}$ prediction changes with changes in the parameters such as the control glycocalyx thickness and permeability were discussed above in Section 4.2.3, and shown in Table 4.1. The key point to remember was that the larger the amount of resistance due to the glycocalyx, the smaller the required decrease in glycocalyx thickness would be to produce the same amount of change in area in the pericapillary space, or change in L_P.

We would next like to discuss the variability and how it is affected by the parameters. We let $\ell_{g,d}^{\,max}$, $\ell_{g,d}^{\,min}$ and $\ell_{g,d}^{\,mean}$ represent the maximum, minimum and mean values *of the medians from each realization*, which are simply the values shown in Tables 4.10 and 4.11. To measure the spread of the data, it seems there are three possibilities. So we introduce ψ_i, $i = 1, 2, 3$ such that

$$\psi_1 = \frac{\ell_{g,d}^{\,max} - \ell_{g,d}^{\,min}}{\ell_{g,d}^{\,mean}} \tag{4.19a}$$

$$\psi_2 = \frac{\ell_{g,d}^{\,max} - \ell_{g,d}^{\,min}}{|\ell_{g,c} - \ell_{g,d}^{\,mean}|} \tag{4.19b}$$

$$\psi_3 = \frac{\ell_{g,d}^{\,max} - \ell_{g,d}^{\,min}}{\ell_{g,c}} \tag{4.19c}$$

It is difficult to decide which of these measures is the most appropriate, for after all we only have the data in the form of histograms from van den Berg et al. (2003), which gives just the frequency of PSD falling in a given range, rather than the actual data points. Thus, we perform this analysis by calculating all three, and discuss the implications at the end of this section. All three equations have the same numerator, which is the difference between the minimum and maximum calculated values of $\ell_{g,d}$. The denominators differ in that the first equation contains the mean value, the second contains the absolute value of the difference of the mean predicted value of glycocalyx thickness from the control value, and the third is simply the control value of glycocalyx thickness.

Regardless of what form is used, we can write out the expressions for $\ell_{g,d}^{\,mean}$, $\ell_{g,d}^{\,max}$, and $\ell_{g,d}^{\,min}$, using Eq. (4.10). To simplify, we introduce

$$\zeta_i = \left(\frac{L_{P,c}}{L_{P,d}}\right)_i$$

where i represents the mean, maximum, or minimum. It is convenient to use Eq. (4.7) to re-write this as

$$\zeta_i = \frac{1}{1+\Delta A_i}$$

and so for instance ζ_{min} corresponds to where ΔA is a minimum, yet due to the decreasing nature of the function, this will be the largest value of ζ_i. Also, when the area change is at its minimum, the degradation of glycocalyx will also be a minimum, meaning that the maximum value of $\ell_{g,d}$ occurs, and vice versa. Thus,

$$\ell_{g,d}^{\,mean} = \ell_{g,c}\zeta_{mean} - \gamma(1-\zeta_{mean}) \tag{4.20a}$$

$$\ell_{g,d}^{\,min} = \ell_{g,c}\zeta_{max} - \gamma(1-\zeta_{max}) \tag{4.20b}$$

$$\ell_{g,d}^{\,max} = \ell_{g,c}\zeta_{min} - \gamma(1-\zeta_{min}) \tag{4.20c}$$

Note that the three ζ_i terms are obtained from our approximation using the χ^2 distributions in Section 4.3.2 and displayed in Table 4.9. The values are $\zeta_{mean} = \frac{1}{1.67} \approx 0.60$, $\zeta_{max} = \frac{1}{1.76} \approx 0.57$, and $\zeta_{min} = \frac{1}{1.58} \approx 0.63$. Substituting Eqs. (4.20) into Eq. (4.19) gives

$$\psi_1 = \frac{\zeta_{min} - \zeta_{max}}{\zeta_{mean} - \left(\dfrac{\Gamma}{1+\Gamma}\right)} \tag{4.21a}$$

$$\psi_2 = \frac{\zeta_{min} - \zeta_{max}}{1-\zeta_{mean}} \tag{4.21b}$$

$$\psi_3 = (1+\Gamma)(\zeta_{min} - \zeta_{max}) \tag{4.21c}$$

The second equation, somewhat surprisingly, depends only on the relative change in L_P, whereas the first and third depend on the ζ_i's as well as Γ. In all of the entries of Tables 4.10 and 4.11 where $k_{g,d} = k_{g,c}$ and $k_c = k_d$, $\psi_2 \approx 0.16$. We discuss the general trends later in this section when studying the more general case where the permeability can vary.

Varying the permeabilities

In Section 4.2.3, we found an expression for the glycocalyx thickness in the case where k_g and k can change upon enzymatic treatment. Recall this expression (4.13)

$$\ell_{g,d} = \left(\frac{k_{g,d}}{k_{g,c}}\right)\left[\ell_{g,c}\left(\frac{L_{P,c}}{L_{P,d}}\right) - \gamma\left(\frac{k_c}{k_d} - \frac{L_{P,c}}{L_{P,d}}\right)\right]$$

We now use the calculations above for the distribution of $\frac{L_{P,c}}{L_{P,d}}$ in this equation to make further predictions. Two cases are considered for control glycocalyx thickness, namely when $\ell_{g,c}$ is 182 or 400 nm. For $k_{g,c}$, we take the two values as above, that is 3.16 or 9.24 nm^2, and we consider only one value for k_c, 21.8 nm^2. Simulations are then performed where $k_{g,d}$ and k_d take either their control values, or a 50% or 100% increase. As previously, we use ten thousand points on the distribution for each realization, then perform one thousand realizations, taking the mean, maximum and minimum values of the median of $\ell_{g,d}$ for each realization. The results are shown in Tables 4.10 (corresponding to $\ell_{g,c} = 182$ nm) and 4.11 (corresponding to $\ell_{g,c} = 400$ nm).

The mean values of $\ell_{g,d}$ for the parameters in the top half of Table 4.10 were discussed previously, and shown in Table 4.5. There were two main observations. First, if the glycocalyx or capillary wall permeability increases with enzymatic treatment, then the glycocalyx need not be degraded by as much to produce the same relative change in area. Second, which of $k_{g,d}$ or k_d has a larger effect depends on the values of the parameters, in particular the resistance to flow due to the glycocalyx. For this parameter combination, the resistance is large enough such that increases in $k_{g,d}$ produce more flow than do increases in k_d.

A similar trend is seen in Table 4.11 for both values of $k_{g,c}$. We compare the mean values in the third and fifth rows when $k_{g,c} = 3.16$ nm^2 to the value in the first row. When $k_d = k_c$, $\ell_{g,d}$ is 211 nm, whereas if k_d is doubled from its control value, $\ell_{g,d}$ is 246 nm. However, if $k_{g,d} = 2k_{g,c}$, we observe that the mean value of glycocalyx thickness is 423 nm, which is *larger than its control value*. Here, the

Table 4.10: Statistics of $\ell_{g,d}$ based on the medians of the realizations for different values of k_g and k. Note the glycocalyx control thickness is $\ell_{g,c} = 182$ nm and $k_c = 21.8$ nm^2.

Parameter values			Statistics of $\ell_{g,d}$		
$k_{g,c}$	$k_{g,d}$	k_d	mean	maximum	minimum
3.16	$k_{g,c}$	k_c	81	89	72
	$k_{g,c}$	1.5 k_c	104	114	96
	$k_{g,c}$	2 k_c	116	125	108
	1.5 $k_{g,c}$	k_c	121	136	110
	2 $k_{g,c}$	k_c	162	179	147
9.24	$k_{g,c}$	k_c	28	41	17
	$k_{g,c}$	1.5 k_c	95	108	83
	$k_{g,c}$	2 k_c	129	145	117
	1.5 $k_{g,c}$	k_c	41	61	23
	2 $k_{g,c}$	k_c	55	85	24

glycocalyx is thick and not very permeable, and thus it provides almost all of the resistance to flow (from Table 4.6 we find a value of 85%), such that increases in glycocalyx permeability will have very pronounced effects in comparison to increases in capillary wall permeability. In effect, our model predicts that for the control values of the parameters in this case, a doubling of glycocalyx permeability upon enzymatic degradation would be too large an increase to account for the measured increase in fluid in the pericapillary space.

This is in stark contrast to the bottom half of Table 4.10, where $\ell_{g,d}$ is 182 nm and $k_{g,c}$ is 9.24 nm^2, so the glycocalyx is thinner and more permeable. For $k_{g,d} = 2k_{g,c}$, the glycocalyx must be degraded to a thickness of 55 nm. If however the capillary wall permeability is doubled, a thickness of 129 nm will suffice to produce the same relative change in area. So, since in this case the glycocalyx contributes less to the total resistance, the effects of its degradation will be less.

Looking at the variability, ψ, requires we re-write Eq. (4.19) using Eq. (4.13) for the $\ell_{g,d}$ terms. This gives the equations:

$$\ell_{g,d}^{\,mean} = \left(\frac{k_{g,d}}{k_{g,c}}\right)\left[\ell_{g,c}\zeta_{mean} - \gamma\left(\frac{k_c}{k_d} - \zeta_{mean}\right)\right] \tag{4.22a}$$

$$\ell_{g,d}^{\,min} = \left(\frac{k_{g,d}}{k_{g,c}}\right)\left[\ell_{g,c}\zeta_{max} - \gamma\left(\frac{k_c}{k_d} - \zeta_{max}\right)\right] \tag{4.22b}$$

$$\ell_{g,d}^{\,max} = \left(\frac{k_{g,d}}{k_{g,c}}\right)\left[\ell_{g,c}\zeta_{min} - \gamma\left(\frac{k_c}{k_d} - \zeta_{min}\right)\right] \tag{4.22c}$$

Table 4.11: Statistics of $\ell_{g,d}$ based on the medians of the realizations for different values of k_g and k. Note the glycocalyx control thickness is $\ell_{g,c} = 400$ nm and $k_c = 21.8$ nm^2.

Parameter values			Statistics of $\ell_{g,d}$		
$k_{g,c}$	$k_{g,d}$	k_d	mean	maximum	minimum
3.16	$k_{g,c}$	k_c	211	228	196
	$k_{g,c}$	1.5 k_c	235	255	217
	$k_{g,c}$	2 k_c	246	262	227
	1.5 $k_{g,c}$	k_c	317	345	293
	2 $k_{g,c}$	k_c	423	450	395
9.24	$k_{g,c}$	k_c	158	181	139
	$k_{g,c}$	1.5 k_c	226	246	208
	$k_{g,c}$	2 k_c	259	278	241
	1.5 $k_{g,c}$	k_c	237	263	209
	2 $k_{g,c}$	k_c	316	355	279

where we recall that the parameter $\gamma = \frac{k_{g,c}}{k_c} R \ln(1+h)$ contains the values in the control situation. To simplify our expressions, we introduce two new parameters which represent the change in glycocalyx permeability and change in capillary wall permeability, respectively. These are

$$\xi = \frac{k_{g,d}}{k_{g,c}} \tag{4.23}$$

$$\theta = \frac{k_d}{k_c} \tag{4.24}$$

Inserting these into Eqs. (4.22), and substituting into Eq. (4.19) gives, after considerable simplification,

$$\psi_1 = \frac{\zeta_{min} - \zeta_{max}}{\zeta_{mean} - \dfrac{\Gamma}{\theta\left(1+\Gamma\right)}} \tag{4.25a}$$

$$\psi_2 = \frac{\zeta_{min} - \zeta_{max}}{\left| \dfrac{\frac{1}{\xi} + \frac{\Gamma}{\theta}}{1+\Gamma} - \zeta_{mean} \right|} \tag{4.25b}$$

$$\psi_3 = \xi(1+\Gamma)(\zeta_{min} - \zeta_{max}) \tag{4.25c}$$

In the case when the permeability of the glycocalyx and capillary wall stays constant (i.e. when $\xi = \theta = 1$), these expressions reduce to Eq. (4.21), as they should. Also, note that the expression for ψ_1 contains θ but not ξ, the expression for ψ_3 contains

ξ but not θ, and the expression for ψ_2 contains both ξ and θ. The values of these quantities are shown in Table 4.12 for the parameter combinations shown in Tables 4.10 and 4.11.

Table 4.12: Values of ψ_i for various parameter combinations.

$\ell_{g,c}$	$k_{g,c}$	ξ	θ	ψ_1	ψ_2	ψ_3
182	3.16	1	1	0.20	0.16	0.09
		1	1.5	0.16	0.21	0.09
		1	2	0.14	0.25	0.09
		1.5	1	0.20	0.41	0.14
		2	1	0.20	1.66	0.18
	9.24	1	1	0.91	0.16	0.14
		1	1.5	0.26	0.29	0.14
		1	2	0.19	0.47	0.14
		1.5	1	0.91	0.27	0.21
		2	1	0.91	0.40	0.28
400	3.16	1	1	0.14	0.16	0.08
		1	1.5	0.13	0.19	0.08
		1	2	0.12	0.20	0.08
		1.5	1	0.14	0.56	0.11
		2	1	0.14	2.65	0.15
	9.24	1	1	0.25	0.16	0.10
		1	1.5	0.17	0.23	0.10
		1	2	0.15	0.28	0.10
		1.5	1	0.25	0.36	0.15
		2	1	0.25	0.94	0.20

We begin with a discussion of ψ_3. It is seen that for fixed $\ell_{g,c}$ and $k_{g,c}$, ψ_3 increases with ξ in a linear fashion, as observed from Eq. (4.25). In the four entries in which $\xi = \theta = 1$, the smallest value of ψ_3 (0.08) is when $\ell_{g,c}$ is 400 nm and $k_{g,c}$ is 3.16 nm^2, which recall is the case when the resistance due to the glycocalyx is its largest (and Γ is smallest). As the value of Γ increases, so too does the value of ψ_3, such that its largest value of 0.14 occurs in the case when the resistance due to the glycocalyx is smallest. Thus for this particular measure, the relative variability ψ_3 is smallest when Γ is small, and largest when Γ is large. For our predictions, this means that in the limit of a high-resistance glycocalyx, our calculations for $\ell_{g,d}$ are more precise. This is easily seen from the equation for ψ_3 when $\Gamma \ll 1$, as there

is no longer dependence on the value of Γ. This makes sense intuitively, because if the glycocalyx provides little resistance as compared to the capillary wall, then the calculations will not be as sensitive to changes in glycocalyx parameters, hence leading to larger variability in the predicted values of $\ell_{g,d}$.

The behaviour of ψ_1, while quite different, actually allows us to draw the same conclusion. Note that ψ_1 decreases as θ increases, although this is not a linear relationship. When $\xi = \theta = 1$, the minimum of ψ_1 occurs for the parameters corresponding to the glycocalyx with highest resistance, the same as for ψ_3. Thus, for the same reason as above, the variability is smallest when the glycocalyx is the dominant resistance to flow, and increases as Γ increases.

Since ψ_2 depends on both ξ and θ, its behaviour is a bit more complex. First, when $\xi = \theta = 1$, the four entries are the same, 0.16, due to the fact that there will be no dependence on Γ. Increases in both ξ and θ produce increases in ψ_2, and which of ξ, θ produce larger increases depends on the control values of glycocalyx thickness and permeability, and hence Γ. When $\Gamma > 1$, which is only for the case when $\ell_{g,c}$ is 182 nm and $k_{g,c}$ is 9.24 nm^2, changes in θ will produce changes of larger magnitude in ψ_2. For the other three cases (when $\Gamma < 1$), changes in ξ produce larger changes in ψ_2.

As mentioned, it is not obvious which one of these measures is the most useful. However, the behaviour of the ψ_i's does allow us to draw the conclusion that when the resistance due to the glycocalyx is larger, our calculation for the predicted glycocalyx thickness is more precise.

4.3.4 Discussion

The validity of this work rests on three assumptions. First, we assume that the histograms in van den Berg et al. (2003) may be represented by the χ^2 distributions generated in Figure 4.10. We are limited by the fact that these histograms give only the percentage of values in each 0.2 μm interval of PSD, rather than the raw data. In the presence of the measured data points, a more thorough statistical analysis could be performed. However, in this work we are interested only in finding a reasonable estimate that can be used to test the predictions of our model against the experimental data, and although there may be optimization procedures or other distributions which give slightly better fits to the data, it is clearly seen from Table 4.8 that our estimates fit the data quite well. In addition, a similar procedure

to that above has been performed attempting to fit the data using a non-central χ^2 distribution, which is a two-parameter distribution. The optimal distributions have approximately the same least-squares error as above, and result in the area enclosed in each 0.2 μm interval being identical to those shown in Table 4.8 up to the number of significant figures displayed.

Another important issue that arises is the fact that using these distributions, there are many values for the relative area change and glycocalyx thickness that are not physical (represented by the left and right spikes in the histograms of Figures 4.11 and 4.13). In fact, the physical situation appears to be represented only about 35-40% of the time. This could be improved by the use of truncated distributions. If we had set lower and upper thresholds on the values of R_c and R_h, which could be obtained from the minimum and maximum values of the measurements in each case, then the spikes could be made less prominent. However, they are still present due to the fact that the values are generated randomly, and thus calculation of any ΔA may use a large value of R_h and a small value of R_c, or vice versa. One way this could be avoided is by ordering R_c and R_h. Then ΔA would be calculated assuming that the minimum R_c value corresponds to the minimum of R_h, etc. In the actual experiment of van den Berg et al. (2003), different vessels are used for the control and hyaluronidase-treated cases, and thus it is not known whether this has any validity. All in all, the spikes at the edges of the histogram should not be too much of a concern – for this is a physiological problem and thus we know which part of the distribution makes sense physically.

The second major assumption is that the relative increase in fluid content in the pericapillary space, and hence the area change, from control to hyaluronidase-treated capillaries is assumed to be equal to the relative change in hydraulic conductivity L_P, as in Eq. (4.7). We have discussed the questionable nature of this assumption in Section 4.2.3, but we now examine the possible functional relationship between these quantities. If we imagine what a graph of ΔA vs. ΔL_P may look like, we know that the curve must pass through the origin and be monotonically increasing, for reasons that are fairly obvious. One possibility is that there are two regimes. The first is in the physiological range, where the relationship between ΔA and ΔL_P may be approximated as linear, with a slope that may differ from unity. With larger increases in L_P, the area cannot continue to increase at the same rate (due to compliance, etc.), so the curve flattens out. Additionally, there must be some threshold for ΔL_P, above which the vessel may collapse for instance. If experiments could be performed such that a functional relationship between ΔA

and L_P were found, we could modify our Eq. (4.7) to accommodate this, and our calculations could be carried out again. If the relationship were linear with a slope not equal to unity for a certain range of values, this would add only a constant multiple to all of our results. Thus, we will take Eq. (4.7) as a first approximation, subject to change with further experimental data.

Our final assumption is that our theoretical relation between L_P and the other physical parameters, given in Eq. (3.76), holds. Of course this must be the case in order for our calculations of $\ell_{g,d}$ to be accurate. These three assumptions, while all containing possible drawbacks, are all easily modified should new experimental data become available.

4.4 Physiological implications

As we have seen, deterioration of the endothelial glycocalyx causes a breakdown of the barrier to transcapillary flow, leading to edema formation. In addition, glycocalyx perturbation in capillaries results in a reduction of functional capillary density and increase in capillary tube haematocrit (Cabrales et al., 2007; VanTeeffelen et al., 2008). Cabrales et al. (2007) found that the changes in functional capillary density result in a redistribution of RBCs in the capillary network such that perfusion was not optimal. Keeping in mind that the main function of the cardiovascular system is the efficient delivery and removal of various substances, dysregulation of optimal conditions could lead to pathological (disease) states.

Although we have focused entirely on the glycocalyx in the microcirculation, recent experimental evidence shows that the glycocalyx in large vessels may play an equally important role. It was found that the glyocalyx was dramatically reduced in regions at high atherogenic risk and by an atherogenic diet (van den Berg et al., 2006), which reflects the fact that a perturbed glycocalyx corresponds to increased vascular vulnerability.

As detailed in Section 4.1, the glycocalyx is involved in mechanotransduction of fluid shear stress into cell signaling processes that trigger nitric oxide (NO) production. Since NO is atheroprotective and an important determinant in vasodilation (VanTeeffelen et al., 2007), regulation of NO production is required to protect against inflammation. Therefore, damage to the glycocalyx results in impaired

shear stress-dependent NO production, and may be associated with inflammatory states.

Shear stress helps to increase glycocalyx dimension by incorporating hyaluronan and other components into the glycocalyx (Gouverneur et al., 2006b), but regions at high atherogenic risk such as near arterial bifurcations have disturbed flow profiles, and therefore irregular shear stress distributions. The fact that the glycocalyx dimension is reduced in the experiments of van den Berg et al. (2006) mentioned above is thus to be expected. Also, van den Berg et al. (2009) observed preferential accumulation of lipids in regions with a perturbed glycocalyx, and Noble et al. (2008) hypothesize that this lipid accumulation combined with the inflammation associated with a perturbed glycocalyx may be essential in the development of atherothrombosis.

Caro et al. (1969, 1971) proposed that atherosclerosis develops preferentially in regions where the arterial wall shear stress is low, and that lipid deposits in the arterial wall were due to shear-dependent mass transfer mechanisms (reviewed in Caro, 2009). In support of this idea, Friedman et al. (1981) showed that intimal thickness correlated negatively with wall shear rate (intimal thickening is a hallmark of atherosclerosis). Since the glycocalyx is reduced at sites of low shear, there should be a correlation between glycocalyx dimension and intimal thickness, and hence between glycocalyx dimension and atherogenic risk. Indeed in the experiments of van den Berg et al. (2006), increased atherogenic risk corresponded to smaller glycocalyx dimensions and increased intimal thickness. Further, the preferential lipid accumulation shown in van den Berg et al. (2009) is precisely a result of the shear-dependent mass transfer referenced above. This is a promising area of research and will be explored further in the Conclusion.

In the future, the endothelial glycocalyx may prove to be a useful diagnostic tool and even a therapeutic target. There have been attempts to measure the systemic glycocalyx volume in humans (Nieuwdorp et al., 2006, 2008); however, the experimental methods have recently been called into question (Michel and Curry, 2009). Thus, more work needs to be done in that area. But, there is evidence showing that the glycocalyx may be therapeutically restored, at least partially (Meuwese et al., 2009). By repairing a damaged glycocalyx through infusion of glycocalyx components, the atheroprotective properties of the vascular wall may be enhanced, thereby lowering the risk for cardiovascular disease.

Chapter 5

Conclusions

In this Thesis a model has been developed to describe the transcapillary flow of fluid and proteins by idealizing the capillary wall as a poroelastic material. The result is that the endothelial cleft, its junction strand with periodic orifices, and the cleft-spanning structures are replaced by an isotropic, homogeneous fluid-solid mixture. This is in contrast to the models of Hu and Weinbaum (1999), who use Hele-Shaw flow, Adamson et al. (2004), who treat the flow in the cleft using a Brinkman equation, and Zhang et al. (2006a), who use a one-dimensional flow through a narrow slit. The similarity between these approaches, however, is that the magnitude of the flow will depend on the amount of resistance in the capillary wall; this can be characterised in each by an effective permeability of the capillary wall region. Consistent with all of these models, we enforce the Michel-Weinbaum hypothesis at the inner wall, just behind the glycocalyx. The result is that the flow has two resistances – that of the glycocalyx, and that of the capillary wall.

Due to the presence of protein concentration gradients in the capillary wall, classical poroelasticity theory must be modified, and the usual assumption of Darcy's law for flow through the porous matrix is not valid. We obtain an equation for the filtration velocity that depends on both hydrostatic and osmotic pressure gradients. In this case, the stress components will also be affected, and thus the constitutive equation is modified to contain an effective pressure, a combination of the hydrostatic and osmotic pressures, which represents the diagonal components of the stress tensor. To close the system of equations, an equation for the osmotic pressure is required. From nonequilibrium thermodynamics, we are able to derive a nonlinear differential equation satisfied by the osmotic pressure field. Through a series

of transformations, a series solution is obtained; and by making an appropriate assumption, this series can be truncated after the first term, giving an analytical solution.

Our results for the transport variables, that is the velocity, hydrostatic pressure, and osmotic pressure, are difficult to compare with other theoretical predictions due to the differences in models, or with experimental works due to the difficulty of obtaining measurements at the small length scales involved. To our knowledge, our predictions for the stress and strain are the first of their kind; we hope that our results stimulate future experimental work to validate our theoretical model.

What we can compare with both theory and experiment is the behaviour of the filtration flux as a function of capillary pressure, and the slope of the line in the graph, namely the hydraulic conductivity L_P. The Starling equation implies that the relation between filtration and capillary pressure should be linear, with intercept equal to the effective osmotic pressure difference. However, the work of Michel and Phillips (1987) showed that for low capillary pressure in the steady-state, the relation was nonlinear and thus there could be no reabsorption. Hu and Weinbaum (1999) predict a nonlinear relation with no steady-state reabsorption, and both the model prediction and experimental results of Adamson et al. (2004) also show no reabsorption in the steady-state. In contrast, one of the main results from Zhang et al. (2006a) is that their model predicts that steady-state reabsorption can occur if the interstitial concentration is low. Their curve is nonlinear, however, with filtration for capillary pressures above 17 $\mathrm{cmH_2O}$ and reabsorption below 17 $\mathrm{cmH_2O}$.

By construction, our model cannot account for the nonlinear behaviour observed in Michel and Phillips (1987) and predicted theoretically by the three studies above. This is due to the fact that we fix the osmotic pressure (hence concentration) just behind the glycocalyx rather than solving the more complicated coupled problem as above. Fixing π_g allows an analytical solution of the governing equation for the osmotic pressure, which in turn gives an analytical solution for filtration velocity and hydrostatic pressure. Since our original goal in Speziale et al. (2008) was to describe transcapillary flow in healthy tissue, this assumption is reasonable. In the case of a deteriorated glycocalyx, the assumption may be called into question; however, in Section 4.2.3 we discussed the reasons for its legitimacy.

The fact that we have a linear relation should not be much cause for concern. The important question experimentally is whether there is in fact reabsorption for

low capillary pressures. Zhang et al. (2006a) predict that reabsorption occurs for capillary pressure below 17 cmH_2O, the same value as our model prediction. So whether or not the curve bends slightly does not change the overall picture, just the magnitude, and only by a small amount. In addition, measurements have not been made with capillary pressures of less than 10 cmH_2O (minimum measured capillary pressure for Adamson et al. (2004) was 15 cmH_2O, for Michel and Phillips (1987) was 12 cmH_2O), since these low pressures are also unlikely to occur in capillaries, except in pathological conditions where flow stasis is possible. Thus, where we depart from Zhang et al. (2006a) is over a small range of capillary pressures, and the departure is of a small magnitude and not likely to change the overall conclusions.

Although the inability to describe the nonlinearity in the curve is a drawback of the model, our approach has some clear advantages. First, we have a theoretical relation for the filtration flux $\frac{J_v}{A}$, and hence also have a relation for the hydraulic conductivity L_P in terms of the parameters characterising the flow, including the glycocalyx thickness and permeability, and capillary wall permeability. Our predicted value of L_P for the best estimates of the parameters is close to the value found experimentally by Adamson et al. (2004). Since L_P is a measurable quantity, as is the glycocalyx thickness ℓ_g, it could be of use to experimentalists to have a relation between these quantities. Additionally, the curves in Section 4.2.4 for L_P as a function of ℓ_g for different values of the capillary wall permeability and glycocalyx permeability, k and k_g respectively, would be of use in estimating k and k_g if L_P and ℓ_g could be measured simultaneously.

Using the results from our model solutions, including those in the previous paragraph, we investigated how a deteriorated glycocalyx could contribute to edema formation, as observed in the experiments of van den Berg et al. (2003). We used a geometric simplification to estimate the change in the fluid content of the pericapillary space under hyaluronidase treatment in which the glycocalyx was deteriorated, and postulated a relation between this quantity and L_P, the assumptions of which have been discussed in detail in Sections 4.2.3 and 4.3.4. The theoretical expression for L_P could then be used to estimate the glycocalyx thickness given the relative change in fluid content, which was calculated first using the median values from the experiments only. Due to the fact that upon hyaluronidase treatment, the glycocalyx permeability as well as the capillary wall permeability may also change, we performed a sensitivity analysis. An important dimensionless parameter, Γ, was identified which describes the relative resistance to flow between the glycocalyx and capillary wall. The limit $\Gamma \ll 1$ corresponds to the glycocalyx being the dominant

resistance, whereas $\Gamma \gg 1$ corresponds to a glycocalyx that provides negligible resistance relative to the capillary wall. The main findings were quite intuitive: if the glycocalyx provides most of the resistance to flow, then its degradation will produce large changes in the amount of flow; if the glycocalyx provides only a small amount of resistance, its degradation will not produce sizable changes in the flow. Thus, to produce a fixed relative change in fluid content, a higher resistance glycocalyx would be required to be degraded less than a lower resistance glycocalyx. The major contribution is in the quantification of these values under different conditions, which are shown in the various tables and figures of Chapter 4.

Later in the chapter, we found probability distributions which optimally fit the histograms of van den Berg et al. (2003) for pericapillary space dimension. These were used to perform all calculations as above, such that the relative change in fluid content ΔA and predicted glycocalyx thickness $\ell_{g,d}$ were also distributions. It was found that using distributions produced some values of glycocalyx thickness that were not physical (negative or extremely large), due to very small values of the PSD in a single realization either in the case of control and hyaluronidase-treated capillaries. For this reason, the statistics we worked with were not the usual statistics in which for instance confidence intervals can be generated. Instead we took the median of each of several realizations, and then looked at the distribution of the medians.

This may be reasonable if we consider that for a single vessel, the PSD is calculated by taking measurements in short intervals around the vessel perimeter, then taking the median of those measurements. This is repeated for a number of vessels in both the control and hyaluronidase-treated cases, and the histograms are then constructed. We can envision each of our realizations as a series of measurements on a single capillary, so that the median value of PSD would correspond to the value placed in the histogram of van den Berg et al. (2003). The difference is that the vessels used in the control and hyaluronidase-treated cases are not the same; in our model however we wish to calculate the relative increase in fluid, assuming that the measurements are taken in a single vessel, first in the control case, then when hyaluronidase has been applied. This is why we first use the distributions to calculate the change in fluid content and glycocalyx thickness, then take the median of each realization. Other issues regarding these assumptions have been discussed in Section 4.3.4.

With regards to improvements or extensions of the current model, it would seem that there are two avenues to explore, namely: 1) coupling the osmotic pressure

behind the glycocalyx to that in the interstitial space, and 2) the transient case. With respect to the former, the manner in which coupling is achieved in the above models is by solving convection-diffusion equations for the concentration of plasma proteins in both the glycocalyx and cleft regions. The boundary conditions then require continuity of concentration and flux across the interface. Thus the concentration (and hence osmotic pressure) at the interface (behind the glycocalyx) emerges as part of the solution of the overall boundary value problem, of which the interstitial protein concentration is a part.

This is not straightforward to take into account in our theory. We obtain an equation for the osmotic pressure directly without computation of the concentration. Seemingly, the most straightforward approach would be to use our osmotic pressure equation in the glycocalyx. However, a rather subtle point arises: in the boundary condition enforcing the Michel-Weinbaum hypothesis, flow across the glycocalyx is treated as a 1-D flow across a membrane, rather than a radial flow as we assume in the capillary wall. This assumption is reasonable if the glycocalyx thickness is much less than the capillary radius, which it is in our case. So then one might ask, should the equation for osmotic pressure in the glycocalyx be in polar or Cartesian coordinates? If we choose polar coordinates, we could truncate the series solution after the first term (the same assumption of $\frac{\pi}{\alpha} \ll 1$ holds in the glycocalyx), and determine the constants by requiring continuity of osmotic pressure and flux at the boundary. We would be required to use the van't Hoff relation to obtain the flux in terms of osmotic pressure, but the RT part would cancel from each term. The problem is that the theories above have a built-in mechanism, the junction strand, that keeps the osmotic pressure behind the glycocalyx low, whereas our homogenized poroelastic material by construction has nothing of this nature. Since the osmotic pressure is high in the capillary, and lower in the tissue, the proposed approach would predict that the osmotic pressure behind the glycocalyx takes a value between the two. As mentioned earlier, this is an advantage of the microstructural models – they can explain why the behaviour occurs. In this work, we do not attempt to do this; instead we use their result for the behaviour of π_g under different flow conditions to investigate our specific problem.

Regarding the transient case, recall from Section 2.5 that the Starling forces were dynamic; that is, that the interstitial hydrostatic and osmotic pressures were not only determinants of the flow, but they also are dependent on the flow. Michel and Phillips (1987) found that transient reabsorption lasts less than two minutes before a steady-state with low to zero filtration is reached. Zhang et al. (2008)

put forward a hypothesis to explain the transient nature of the phenomenon, in which pericytes covering the cleft exits create *trapped microdomains* which regulate the time-dependent response. The model of Zhang et al. (2006a) was adapted to include two new regions: a trapped microdomain, and the exit region of the trapped microdomain at the pericyte edge. They predict an equilibration time on the order of one minute.

Extending our theory to the time-dependent case is certainly possible, although the problem becomes significantly more complicated, as the transport and stress-strain problems are coupled. In addition, it is not likely that this phenomenon can be explained solely by consolidation effects. From Biot (1941), one finds that the dilatation (local volume change) of the porous material obeys a diffusion equation, with the consolidation coefficient κ_c taking the place of the diffusion coefficient. Thus, the time scale for this process is L^2/κ_c, where L is the length scale. Taking L to be the thickness of the capillary wall ΔR, and the value for κ_c from Chapter 3, this time scale is of the order of 10^{-4} s, much too small to explain transient reabsorption.

Finally, we end our discussion with a couple of problems to which the theory developed in this Thesis may be applied. The first is in relation to cardiovascular disease, and was discussed at the end of Chapter 4. In the microcirculation, a deteriorated glycocalyx leads to edema formation and less than optimal perfusion conditions. How efficiently a network is perfused depends on many parameters, such as the flow rate, vascular pressure, vessel diameter (and thus resistance), hematocrit and viscosity, as well as the wall shear stress, wall thickness and circumferential wall stress. These hemodynamic parameters along with the metabolic demands of the tissue drive the continuous structural adaptation, or remodeling, of the microcirculation (Pries and Secomb, 2008). For example, vessels can sense wall shear stress, so if the flow rate of the blood is increased (which in turn would increase shear stress), then the diameter of the vessel increases (vasodilation) such that the shear stress returns to its normal level. This is precisely what occurs during exercise. Another example of structural adaptation is when there are decreased oxygen levels in a tissue, a signal is sent to increase perfusion thus bringing more oxygen to the tissue.

Upon glycocalyx degradation, all of these hemodynamic parameters may be subject to change. The response of the vasculature to hemodynamic or metabolic stimuli can change the functional properties of the network (Pries et al., 2005), and so a deteriorated glycocalyx disturbs the delicate balance of the various factors,

thus affecting the adaptation of the network. If we recall from the discussion at the end of Chapter 4 that the glycocalyx 'senses' shear stress and that shear stress increases glycocalyx dimension, it is clear that the interplay of these two will be important. An illustration of this was observed in the study of Yao et al. (2007), who showed that with an intact glycocalyx, endothelial cells align with flow, yet after removal of the glycocalyx the cells no longer align. Thus, the glycocalyx is required for the endothelial cell response to fluid shear. Wang (2007) modeled how changes in the properties of the glycocalyx affect the stress and shear rate on the endothelial monolayer, and found that with parameter changes corresponding to glycocalyx degradation, the pulling stress on the endothelium was decreased and the shear rate was increased. A more detailed model involving the interactions of the various factors driving structural adaptation would be useful.

Shear stress is as important in large vessels as it is in the microcirculation. In atherosclerosis, there is accumulation of low-density lipoprotein (LDL) and other lipids at sites in the arterial wall where the shear stress is low, which was proposed to be due to a shear-dependent mass transfer mechanism (Caro et al., 1969, 1971). Recall that regions of atherogenic risk as well as an atherogenic diet reduce glycocalyx thickness, and also that regions with a thinner glycocalyx correspond to regions where the intimal layer is thicker. These sites further correspond to the regions of lipid deposits. A mathematical description of the transport of LDL through the glycocalyx, intima, and other structures in the arterial wall, would be able to shed light on this complex process.

A question naturally arises regarding the relationship between the glycocalyx in large and small vessels. If the glycocalyx was found to be reduced in a large artery, could it be inferred that the glycocalyx dimension was decreased in the microcirculation, and to what extent? It seems that the answer should be yes, but the extent of which is unknown. We are unaware of any quantitative studies that attempt to answer this question. Perhaps the attempts to measure systemic glycocalyx volume in humans could be performed in mice. Then, this data could be combined with data from electron microscope images as in van den Berg et al. (2003) measuring the glycocalyx dimension in small vessels of these same mice. By analysing the data from the estimates in small vessels along with the systemic volume, it is possible that a clearer picture may emerge of how the glycocalyx is distributed throughout the circulation.

The other area of application is in the study of tumour vasculature, and more specifically drug delivery to tumours. Blood vessels in tumours have irregular struc-

ture, are heterogeneous, and do not fit into the regular branching patterns of arterioles, capillaries and venules. Most importantly, the walls are often referred to as 'leaky', due to the fact that they are an order of magnitude more permeable than vessels in normal tissue. Hashizume et al. (2000) found that there was a defective endothelial monolayer and moreover, that there were large intercellular openings with an average diameter of 1.7 μm that could explain the vessel leakiness. However, recently Sarin et al. (2009) reported that the upper limit of pore size in tumour vessels was only 12 nm, which would be consistent with the glycocalyx acting as the primary impediment to transcapillary flow. They suggest that this huge discrepancy (two orders of magnitude) is due to the fact that cationic nanoparticles were used in other studies and were most likely toxic to the negatively charged glycocalyx, in a process analogous to enzymatic degradation. Thus, large particles could traverse the capillary wall and the upper limit of pore size would be overestimated. This was not a criticism of the methods used by Hashizume et al. (2000) in particular, but of those used by another study (Hobbs et al., 1998) that had similar conclusions. However, in Hashizume et al. (2000), the large holes in the endothelial monolayer are visible from the scanning electron microscope images.

Whether the glycocalyx is indeed present in tumour vessels and to what extent it is functional is a significant question. Another fundamental piece of information is the pore cut-off size of tumour blood vessels. With the ever-expanding use of nanoparticles as delivery systems for anti-cancer drugs, characterisation of the capillary wall structure in tumours is key to understanding which agents will be effective at penetrating deep into the tumour tissue and thus reaching the cancer cells. For instance, if the upper limit of pore size was 12 nm, then one would not expect nanoparticles of say 100 nm to pass through the wall and reach the cancer cells; however, they do.

The work in this Thesis can be useful in the sense that we describe the relative resistances to flow of the glycocalyx and capillary wall and we have relations between various important parameters such as the hydraulic conductivity, glycocalyx thickness and permeability, and capillary wall permeability. Thus, in combination with experimental data, our model could estimate both the effect of the glycocalyx and physiological limit of pore size in tumour blood vessels. Additionally, our model allows study of the transport of drug or nanoparticle through the capillary wall. Ultimately, it is possible that the model could explain the permeability of a vessel to a given nanoparticle.

However, to describe accurately the efficacy of a drug, a model of the entire

vascular network is required. Tumour vasculature is abnormal, inefficient, and has a large degree of spatial heterogeneity. Thus, a model of the vascular network should be of a stochastic rather than deterministic nature. The important parameters that characterise a given vasculature, namely the vessel diameters, vessel density, and spacing between vessels, are heterogeneous among different tumours, and in fact are spatially and temporally heterogeneous within the same tumour. The combination of this dysregulated network with the lack of functional lymphatics leads to an increased interstitial fluid pressure (IFP), which Jain (1987) pointed out is a hindrance to drug delivery. Baxter and Jain (1989, 1990) used a flow through porous media approach to describe the transport of fluid and anti-cancer agents in a tumour. They found that the interstitial fluid pressure was uniformly high throughout most of the tumour and dropped sharply in the periphery, and that this pressure gradient prevented drug molecules at the outer regions of the tumour from being transported by convection to the centre of the tumour, with the effect that not all tumour cells would receive the drug.

To overcome this, Jain (2001) proposed the use of anti-angiogenic agents in combination with conventional chemotherapy. The idea was that anti-angiogenic agents could transiently *normalize* the vasculature, with the consequence that IFP would be reduced and thus the penetration of drugs would improve. In a stochastic model of the vasculature, anti-angiogenic treatment would be described by a change in the properties such as vessel density and spacing. Identifying the time-course of these changes and their effects on IFP could be helpful in optimizing treatment strategies.

Appendix
The χ^2-distribution

If $X_1, X_2, \ldots X_n$ are normally distributed random variables each with a mean of zero and variance of one, then the random variable

$$Y = \sum_{i=1}^{k} X_i^2$$

is distributed according to the chi-square distribution with k degrees of freedom. We can write

$$Y \sim \chi^2(k)$$

The probability density function (pdf) is

$$f(x; k) = \frac{1}{2^{k/2}\Gamma(k/2)} x^{k/2-1} e^{-x/2}$$

where $\Gamma(k/2)$ is the Gamma function, defined as

$$\Gamma(z) = \int_0^\infty t^{z-1} e^t \, dt$$

The cumulative distribution function (cdf) is

$$F(x; k) = \frac{\gamma(k/2, x/2)}{\Gamma(k/2)}$$

where $\gamma(k/2, x/2)$ is the lower incomplete Gamma function, defined by

$$\gamma(s, x) = \int_0^x t^{s-1} e^{-t} \, dt$$

The χ^2 distribution is defined for $x \geq 0$. Using the definition, one can show that the mean of the distribution with k degrees of freedom is exactly k. The mode is $k - 2$ for $k \geq 2$, or zero for $k < 2$, and the variance is $2k$.

The χ^2 distribution is used in inferential statistics, namely in hypothesis testing and regression line fitting. Pearson's chi-square test is used for two kinds of tests: goodness of fit, in which it is checked whether an observed, or experimentally measured, distribution matches a theoretical one, and tests of independence, in which it is determined when observations on two variables are independent of one another.

We, however, wish to use the χ^2 distribution only as a curve fit for the histograms of van den Berg et al. (2003). The only statistics given in van den Berg et al. (2003) were the medians, which we defined as $R_{c,m}$ and $R_{h,m}$ to represent the control and hyaluronidase-treated cases. Using the function `chi2pdf` in `MATLAB`, we generate χ^2 distributions for values of k between 1 and 10. Then the median of the distribution with k degrees of freedom, denoted $R_{k,m}$, is found using the `chi2inv` function. The scaling factors $S_{c,k}$ and $S_{h,k}$ are then computed as explained in the main text, and used to scale the distributions so that the $x-$coordinate is now a dimensional quantity, namely the PSD. Using the `chi2cdf` function, the cumulative area under each 0.2 μm section is calculated, which can then be compared with the histograms of van den Berg et al. (2003). The value of k in each case corresponds to the best fit in a least-squares sense. We find that

$$R_c \sim \chi^2(1.97) \tag{A.1}$$

$$R_h \sim \chi^2(4.73) \tag{A.2}$$

These distributions were then used to calculate the increase in fluid content in the pericapillary space in Section 4.3.2. In order to do this, data points for R_c and R_h are generated from their respective distributions, which we accomplish using the function `chi2rnd` in `MATLAB`. This function generates a given number of points randomly from the distribution. We use ten thousand points for each, and scale the $x-$axis according to the scaling factors above. Then the expressions (4.2) and (4.3) give the relative change in area and hence fluid content, which is now a distribution. Finally, using the assumption in Eq. (4.7), we use the calculated distributions to predict the glycocalyx thickness corresponding to the given area change and hence change in L_P.

References

R. H. Adamson. Permeability of frog mesenteric capillaries after partial pronase digestion of the endothelial glycocalyx. *J. Physiol. (Lond.)*, 428:1–13, Sep 1990.

R. H. Adamson and G. Clough. Plasma proteins modify the endothelial cell glycocalyx of frog mesenteric microvessels. *J. Physiol. (Lond.)*, 445:473–486, Jan 1992.

R. H. Adamson and C. C. Michel. Pathways through the intercellular clefts of frog mesenteric capillaries. *J. Physiol. (Lond.)*, 466:303–327, Jul 1993.

R. H. Adamson, J. F. Lenz, X. Zhang, G. N. Adamson, S. Weinbaum, and F. E. Curry. Oncotic pressures opposing filtration across non-fenestrated rat microvessels. *J. Physiol. (Lond.)*, 557:889–907, Jun 2004.

S. Bader and H. Kooi. Modelling of solute and water transport in semi-permeable clay membranes: comparison with experiments . *Adv. Water Res.*, 28:203–214, Mar 2005.

G. K. Batchelor. *An Introduction to Fluid Dynamics*. Cambridge University Press, Inc., New York, 1967.

D. O. Bates, J. R. Levick, and P. S. Mortimer. Starling pressures in the human arm and their alteration in postmastectomy oedema. *J. Physiol. (Lond.)*, 477 (Pt 2):355–363, Jun 1994.

L. T. Baxter and R. K. Jain. Transport of fluid and macromolecules in tumors. I. Role of interstitial pressure and convection. *Microvasc. Res.*, 37:77–104, Jan 1989.

L. T. Baxter and R. K. Jain. Transport of fluid and macromolecules in tumors. II. Role of heterogeneous perfusion and lymphatics. *Microvasc. Res.*, 40:246–263, Sep 1990.

M. A. Biot. General theory of three-dimensional consolidation. *J. Appl. Phys.*, 12: 155–164, Feb 1941.

J. Brands, B. M. VanTeeffelen, J. W. G. E. van den Berg, and H. Vink. Role for glycocalyx perturbation in atherosclerosis development and associated microvascular dysfunction. *Future Lipidol.*, 2:527–534, 2007.

H. C. Brinkman. A calculation of the viscous force exerted by a flowing fluid on a dense swarm of particles. *Appl. Sci. Res*, A1:27–34, 1947.

L. N. Broekhuizen, H. L. Mooij, J. J. Kastelein, E. S. Stroes, H. Vink, and M. Nieuwdorp. Endothelial glycocalyx as potential diagnostic and therapeutic target in cardiovascular disease. *Curr. Opin. Lipidol.*, 20:57–62, Feb 2009.

R. Burridge and J. B. Keller. Poroelasticity equations derived from microstructure. *J. Acoust. Soc. Amer.*, 70:1140–1146, 1981.

P. Cabrales, B. Y. Vazquez, A. G. Tsai, and M. Intaglietta. Microvascular and capillary perfusion following glycocalyx degradation. *J. Appl. Physiol.*, 102:2251–2259, Jun 2007.

C. G. Caro. Discovery of the role of wall shear in atherosclerosis. *Arterioscler. Thromb. Vasc. Biol.*, 29:158–161, Feb 2009.

C. G. Caro, J. M. Fitz-Gerald, and R. C. Schroter. Arterial wall shear and distribution of early atheroma in man. *Nature*, 223:1159–1160, Sep 1969.

C. G. Caro, J. M. Fitz-Gerald, and R. C. Schroter. Atheroma and arterial wall shear. Observation, correlation and proposal of a shear dependent mass transfer mechanism for atherogenesis. *Proc. R. Soc. Lond., B, Biol. Sci.*, 177:109–159, Feb 1971.

C. G. Caro, T. J. Pedley, R. C. Schroter, and W. A. Seed. *The Mechanics of the Circulation*. Oxford University Press, Toronto, 1978.

S. E. Charm and G. S. Kurland. *Blood Flow and Microcirculation*. Wiley, New York, 1974.

G. Clough, C. C. Michel, and M. E. Phillips. Inflammatory changes in permeability and ultrastructure of single vessels in the frog mesenteric microcirculation. *J. Physiol. (Lond.)*, 395:99–114, Jan 1988.

A. A. Constantinescu, H. Vink, and J. A. Spaan. Endothelial cell glycocalyx modulates immobilization of leukocytes at the endothelial surface. *Arterioscler. Thromb. Vasc. Biol.*, 23:1541–1547, Sep 2003.

F. E. Curry. *Mechanics and Thermodynamics of Transcapillary Exchange*, chapter 8, pages 309–374. Handbook of Physiology. Waverly Press, Inc., Bethesda, Maryland, 1984.

F. E. Curry and C. C. Michel. A fiber matrix model of capillary permeability. *Microvasc. Res.*, 20:96–99, Jul 1980.

F. E. Curry, C. C. Michel, and J. C. Mason. Osmotic reflextion coefficients of capillary walls to low molecular weight hydrophilic solutes measured in single perfused capillaries of the frog mesentery. *J. Physiol. (Lond.)*, 261:319–336, Oct 1976.

F. E. Curry, C. C. Michel, and M. E. Phillips. Effect of albumin on the osmotic pressure exerted by myoglobin across capillary walls in frog mesentery. *J. Physiol. (Lond.)*, 387:69–82, Jun 1987.

E. R. Damiano. The effect of the endothelial-cell glycocalyx on the motion of red blood cells through capillaries. *Microvasc. Res.*, 55:77–91, Jan 1998.

J. Feng and S. Weinbaum. Lubrication theory in highly compressible porous media: the mechanics of skiing from red cells to humans. *J. Fluid Mech.*, 422:281–317, Jan 2000.

J. A. Florian, J. R. Kosky, K. Ainslie, Z. Pang, R. O. Dull, and J. M. Tarbell. Heparan sulfate proteoglycan is a mechanosensor on endothelial cells. *Circ. Res.*, 93:e136–142, Nov 2003.

M. H. Friedman, G. M. Hutchins, C. B. Bargeron, O. J. Deters, and F. F. Mark. Correlation between intimal thickness and fluid shear in human arteries. *Atherosclerosis*, 39:425–436, Jun 1981.

B. Fu, F. R. Curry, R. H. Adamson, and S. Weinbaum. A model for interpreting the tracer labeling of interendothelial clefts. *Ann Biomed Eng*, 25:375–397, 1997.

B. M. Fu, S. Weinbaum, R. Y. Tsay, and F. E. Curry. A junction-orifice-fiber entrance layer model for capillary permeability: application to frog mesenteric capillaries. *J Biomech Eng*, 116:502–513, Nov 1994.

Y. C. Fung. *Biomechanics Circulation (2nd ed.)*. Springer, New York, 1997.

M. Gouverneur, B. Berg, M. Nieuwdorp, E. Stroes, and H. Vink. Vasculoprotective properties of the endothelial glycocalyx: effects of fluid shear stress. *J. Intern. Med.*, 259:393–400, Apr 2006a.

M. Gouverneur, J. A. Spaan, H. Pannekoek, R. D. Fontijn, and H. Vink. Fluid shear stress stimulates incorporation of hyaluronan into endothelial cell glycocalyx. *Am. J. Physiol. Heart Circ. Physiol.*, 290:H458–452, Jan 2006b.

A. C. Guyton. A concept of negative interstitial pressure based on pressures in implanted perforated capsules. *Circ. Res.*, 12:399–414, Apr 1963.

A. C. Guyton, H. J. Granger, and A. E. Taylor. Interstitial fluid pressure. *Physiol. Rev.*, 51:527–563, Jul 1971.

H. Hashizume, P. Baluk, S. Morikawa, J. W. McLean, G. Thurston, S. Roberge, R. K. Jain, and D. M. McDonald. Openings between defective endothelial cells explain tumor vessel leakiness. *Am. J. Pathol.*, 156:1363–1380, Apr 2000.

C. B. Henry and B. R. Duling. TNF-alpha increases entry of macromolecules into luminal endothelial cell glycocalyx. *Am. J. Physiol. Heart Circ. Physiol.*, 279: H2815–2823, Dec 2000.

C. B. Henry and B. R. Duling. Permeation of the luminal capillary glycocalyx is determined by hyaluronan. *Am. J. Physiol.*, 277:H508–514, Aug 1999.

S. K. Hobbs, W. L. Monsky, F. Yuan, W. G. Roberts, L. Griffith, V. P. Torchilin, and R. K. Jain. Regulation of transport pathways in tumor vessels: role of tumor type and microenvironment. *Proc. Natl. Acad. Sci. U.S.A.*, 95:4607–4612, Apr 1998.

X. Hu and S. Weinbaum. A new view of Starling's hypothesis at the microstructural level. *Microvasc. Res.*, 58:281–304, Nov 1999.

X. Hu, R. H. Adamson, B. Liu, F. E. Curry, and S. Weinbaum. Starling forces that oppose filtration after tissue oncotic pressure is increased. *Am. J. Physiol. Heart Circ. Physiol.*, 279:H1724–1736, Oct 2000.

R. K. Jain. Normalizing tumor vasculature with anti-angiogenic therapy: a new paradigm for combination therapy. *Nat. Med.*, 7:987–989, Sep 2001.

R. K. Jain. Transport of molecules in the tumor interstitium: a review. *Cancer Res.*, 47:3039–3051, Jun 1987.

A. Katchalsky and P. F. Curran. *Nonequilibrium Thermodynamics in Biophysics.* Harvard University Press, Cambridge, Massachusetts, 1965.

D. E. Kenyon. Transient filtration in a porous elastic cylinder. *ASME J. Appl. Mech.*, 43:594–598, 1976a.

D. E. Kenyon. The theory of an incompressible solid-fluid mixture. *Arch. Ration. Mech. Anal.*, 62:131–147, 1976b.

D. E. Kenyon. A mathematical model of water flux through aortic tissue. *Bull. Math. Biol.*, 41:79–90, 1979.

A. Krogh. *Anatomy and Physiology of the Capillaries.* Yale University Press, New Haven, Connecticut, 1922.

E. M. Landis. Micro-injection studies of capillary permeability II. The relation between capillary pressure and the rate at which fluid passes through the walls of single capillaries. *Am. J. Physiol.*, 82:217–238, October 1927.

E. M. Landis. Micro-injection studies of capillary permeability III. The effect of lack of oxygen on the permeability of the capillary wall to fluid and to plasma proteins. *Am. J. Physiol.*, 83:528–542, 1928.

E. M. Landis. Micro-injection studies of capillary blood pressure in human skin. *Heart*, 15:209–228, 1930.

N. N. Lebedev. *Special Functions and their Applications.* Dover, New York, 1972.

J. R. Levick. Revision of the Starling principle: new views of tissue fluid balance. *J. Physiol. (Lond.)*, 557:704, Jun 2004.

J. R. Levick. Capillary filtration-absorption balance reconsidered in light of dynamic extravascular factors. *Exp. Physiol.*, 76:825–857, Nov 1991.

J. R. Levick. An analysis of the interaction between interstitial plasma protein, interstitial flow, and fenestral filtration and its application to synovium. *Microvasc. Res.*, 47:90–125, Jan 1994.

J. R. Levick. *An Introduction to Cardiovascular Physiology.* Arnold, London, 2003.

J. R. Levick and L. H. Smaje. An analysis of the permeability of a fenestra. *Microvasc. Res.*, 33:233–256, Mar 1987.

J. H. Luft. Fine structures of capillary and endocapillary layer as revealed by ruthenium red. *Fed. Proc.*, 25:1773–1783, 1966.

J. C. Mason, F. E. Curry, and C. C. Michel. The effects of proteins upon the filtration coefficient of individually perfused frog mesenteric capillaries. *Microvasc. Res.*, 13:185–202, Mar 1977.

J. N. McDonald and J. R. Levick. Effect of extravascular plasma protein on pressure-flow relations across synovium in anaesthetized rabbits. *J. Physiol. (Lond.)*, 465:539–559, Jun 1993.

M. C. Meuwese, H. L. Mooij, M. Nieuwdorp, B. van Lith, R. Marck, H. Vink, J. J. Kastelein, and E. S. Stroes. Partial recovery of the endothelial glycocalyx upon rosuvastatin therapy in patients with heterozygous familial hypercholesterolemia. *J. Lipid Res.*, 50:148–153, Jan 2009.

C. C. Michel. *Fluid Movements through Capillary Walls*, chapter 9, pages 375–410. Handbook of Physiology. Waverly Press, Inc., Bethesda, Maryland, 1984.

C. C. Michel. Fluid exchange in the microcirculation. *J. Physiol. (Lond.)*, 557: 701–702, Jun 2004.

C. C. Michel. The measurement of permeability in single capillaries. *Arch. Int. Physiol. Biochim.*, 86:657–667, Aug 1978.

C. C. Michel. Filtration coefficients and osmotic reflexion coefficients of the walls of single frog mesenteric capillaries. *J. Physiol. (Lond.)*, 309:341–355, Dec 1980.

C. C. Michel. Starling: the formulation of his hypothesis of microvascular fluid exchange and its significance after 100 years. *Exp. Physiol.*, 82:1–30, Jan 1997.

C. C. Michel and F. R. Curry. Glycocalyx volume: a critical review of tracer dilution methods for its measurement. *Microcirculation*, 16:213–219, Apr 2009.

C. C. Michel and M. E. Phillips. The effects of bovine serum albumin and a form of cationised ferritin upon the molecular selectivity of the walls of single frog capillaries. *Microvasc. Res.*, 29:190–203, Mar 1985.

C. C. Michel and M. E. Phillips. Steady-state fluid filtration at different capillary pressures in perfused frog mesenteric capillaries. *J. Physiol. (Lond.)*, 388:421–435, Jul 1987.

C. C. Michel, J. C. Mason, F. E. Curry, J. E. Tooke, and P. J. Hunter. A development of the Landis technique for measuring the filtration coefficient of individual capillaries in the frog mesentery. *Q J Exp Physiol Cogn Med Sci*, 59:283–309, Oct 1974.

S. Mochizuki, H. Vink, O. Hiramatsu, T. Kajita, F. Shigeto, J. A. Spaan, and F. Kajiya. Role of hyaluronic acid glycosaminoglycans in shear-induced endothelium-derived nitric oxide release. *Am. J. Physiol. Heart Circ. Physiol.*, 285:H722–726, Aug 2003.

V. C. Mow, S. C. Kuei, W. M. Lai, and C. G. Armstrong. Biphasic creep and stress relaxation of articular cartilage in compression? Theory and experiments. *J Biomech Eng*, 102:73–84, Feb 1980.

A. W. Mulivor and H. H. Lipowsky. Inflammation- and ischemia-induced shedding of venular glycocalyx. *Am. J. Physiol. Heart Circ. Physiol.*, 286:H1672–1680, May 2004.

T. Nagashima, N. Tamaki, S. Matsumoto, B. Horwitz, and Y. Seguchi. Biomechanics of hydrocephalus: a new theoretical model. *Neurosurgery*, 21:898–904, Dec 1987.

M. Nieuwdorp, T. W. van Haeften, M. C. Gouverneur, H. L. Mooij, M. H. van Lieshout, M. Levi, J. C. Meijers, F. Holleman, J. B. Hoekstra, H. Vink, J. J. Kastelein, and E. S. Stroes. Loss of endothelial glycocalyx during acute hyperglycemia coincides with endothelial dysfunction and coagulation activation in vivo. *Diabetes*, 55:480–486, Feb 2006.

M. Nieuwdorp, F. Holleman, E. de Groot, H. Vink, J. Gort, A. Kontush, M. J. Chapman, B. A. Hutten, C. B. Brouwer, J. B. Hoekstra, J. J. Kastelein, and E. S. Stroes. Perturbation of hyaluronan metabolism predisposes patients with type 1 diabetes mellitus to atherosclerosis. *Diabetologia*, 50:1288–1293, Jun 2007.

M. Nieuwdorp, M. C. Meuwese, H. L. Mooij, C. Ince, L. N. Broekhuizen, J. J. Kastelein, E. S. Stroes, and H. Vink. Measuring endothelial glycocalyx dimensions in humans: a potential novel tool to monitor vascular vulnerability. *J. Appl. Physiol.*, 104:845–852, Mar 2008.

M. I. Noble, A. J. Drake-Holland, and H. Vink. Hypothesis: arterial glycocalyx dysfunction is the first step in the atherothrombotic process. *QJM*, 101:513–518, Jul 2008.

L. Onsager. Reciprocal relations in irreversible processes. i. *Phys. Rev.*, 37(4): 405–426, Feb 1931.

J. R. Pappenheimer and A. Soto-Rivera. Effective osmotic pressure of the plasma proteins and other quantities associated with the capillary circulation in the hindlimbs of cats and dogs. *Am. J. Physiol.*, 152:471–491, Mar 1948.

J. R. Pappenheimer, E. M. Renkin, and L. M. Borrero. Filtration, diffusion and molecular sieving through peripheral capillary membranes; a contribution to the pore theory of capillary permeability. *Am. J. Physiol.*, 167:13–46, Oct 1951.

C. S. Patlak, D. A. Goldstein, and J. F. Hoffman. The flow of solute and solvent across a two-membrane system. *J. Theor. Biol.*, 5:426–442, Nov 1963.

A. R. Pries and T. W. Secomb. Modeling structural adaptation of microcirculation. *Microcirculation*, 15:753–764, Nov 2008.

A. R. Pries, T. W. Secomb, and P. Gaehtgens. The endothelial surface layer. *Pflugers Arch.*, 440:653–666, Sep 2000.

A. R. Pries, B. Reglin, and T. W. Secomb. Remodeling of blood vessels: responses of diameter and wall thickness to hemodynamic and metabolic stimuli. *Hypertension*, 46:725–731, Oct 2005.

S. Reitsma, D. W. Slaaf, H. Vink, M. A. van Zandvoort, and M. G. oude Egbrink. The endothelial glycocalyx: composition, functions, and visualization. *Pflugers Arch.*, 454:345–359, Jun 2007.

E. M. Renkin. Multiple pathways of capillary permeability. *Circ. Res.*, 41:735–743, Dec 1977.

H. Sarin, A. S. Kanevsky, H. Wu, A. A. Sousa, C. M. Wilson, M. A. Aronova, G. L. Griffiths, R. D. Leapman, and H. Q. Vo. Physiologic upper limit of pore size in the blood-tumor barrier of malignant solid tumors. *J Transl Med*, 7:51, 2009.

C. Schulze and J. A. Firth. The interendothelial junction in myocardial capillaries: evidence for the existence of regularly spaced, cleft-spanning structures. *J. Cell. Sci.*, 101 (Pt 3):647–655, Mar 1992.

T. W. Secomb, R. Hsu, and A. R. Pries. A model for red blood cell motion in glycocalyx-lined capillaries. *Am. J. Physiol.*, 274:H1016–1022, Mar 1998.

T. W. Secomb, R. Hsu, and A. R. Pries. Motion of red blood cells in a capillary with an endothelial surface layer: effect of flow velocity. *Am. J. Physiol. Heart Circ. Physiol.*, 281:H629–636, Aug 2001.

M. Simionescu and N. Simionescu. *Ultrastructure of the Microvascular Wall: Functional Correlations*, chapter 3, pages 41–102. Handbook of Physiology. Waverly Press, Inc., Bethesda, Maryland, 1984.

L. Smaje, B. W. Zweifach, and M. Intaglietta. Micropressures and capillary filtration coefficients in single vessels of the cremaster muscle of the rat. *Microvasc. Res.*, 2:96–110, Jan 1970.

M. L. Smith, D. S. Long, E. R. Damiano, and K. Ley. Near-wall micro-PIV reveals a hydrodynamically relevant endothelial surface layer in venules in vivo. *Biophys. J.*, 85:637–645, Jul 2003.

S. Speziale and S. Sivaloganathan. Poroelastic theory of transcapillary flow: effects of endothelial glycocalyx deterioration. *Microvasc. Res.*, 78:432–441, Dec 2009.

S. Speziale, G. Tenti, and S. Sivaloganathan. A poroelastic model of transcapillary flow in normal tissue. *Microvasc. Res.*, 75:285–295, Mar 2008.

J. M. Squire, M. Chew, G. Nneji, C. Neal, J. Barry, and C. Michel. Quasi-periodic substructure in the microvessel endothelial glycocalyx: a possible explanation for molecular filtering? *J. Struct. Biol.*, 136:239–255, Dec 2001.

E. H. Starling. On the Absorption of Fluids from the Connective Tissue Spaces. *J. Physiol. (Lond.)*, 19:312–326, May 1896.

A. J. Staverman. The theory of measurement of osmotic pressure. *Rec. Trav. Chim. Pays - Bas Belg.*, 70:344–352, 1951.

M. Sugihara-Seki, T. Akinaga, and T. Itano. Flow across microvessel walls through the endothelial surface glycocalyx and the interendothelial cleft. *J. Fluid Mech.*, 601:229–252, 2008.

J. M. Tarbell and M. Y. Pahakis. Mechanotransduction and the glycocalyx. *J. Intern. Med.*, 259:339–350, Apr 2006.

J. M. Tarbell, S. Weinbaum, and R. D. Kamm. Cellular fluid mechanics and mechanotransduction. *Ann Biomed Eng*, 33:1719–1723, Dec 2005.

G. Tenti, S. Sivaloganathan, and J. M. Drake. Brain biomechanics: steady-state consolidation theory of hydrocephalus. *Can. Appl. Math Q.*, pages 93–110, 1999.

G. Tenti, J. M. Drake, and S. Sivaloganathan. Brain biomechanics: mathematical modeling of hydrocephalus. *Neurol. Res.*, 22:19–24, Jan 2000.

M. M. Thi, J. M. Tarbell, S. Weinbaum, and D. C. Spray. The role of the glycocalyx in reorganization of the actin cytoskeleton under fluid shear stress: a "bumper-car" model. *Proc. Natl. Acad. Sci. U.S.A.*, 101:16483–16488, Nov 2004.

R. Tsay and S. Weinbaum. Viscous flow in a channel with periodic cross-bridging fibres: exact solutions and Brinkman approximation. *J. Fluid Mech.*, 226:125–148, 1991.

R. Tsay, S. Weinbaum, and R. Pfeffer. A new model for capillary filtration based on recent electron microscopic studies of endothelial junctions. *Chem Eng Commun*, 82:67–102, 1989.

B. M. van den Berg, H. Vink, and J. A. Spaan. The endothelial glycocalyx protects against myocardial edema. *Circ. Res.*, 92:592–594, Apr 2003.

B. M. van den Berg, J. A. Spaan, T. M. Rolf, and H. Vink. Atherogenic region and diet diminish glycocalyx dimension and increase intima-to-media ratios at murine carotid artery bifurcation. *Am. J. Physiol. Heart Circ. Physiol.*, 290: H915–920, Feb 2006.

B. M. van den Berg, J. A. Spaan, and H. Vink. Impaired glycocalyx barrier properties contribute to enhanced intimal low-density lipoprotein accumulation at the carotid artery bifurcation in mice. *Pflugers Arch.*, 457:1199–1206, Apr 2009.

J. W. VanTeeffelen, J. Brands, C. Jansen, J. A. Spaan, and H. Vink. Heparin impairs glycocalyx barrier properties and attenuates shear dependent vasodilation in mice. *Hypertension*, 50:261–267, Jul 2007.

J. W. VanTeeffelen, A. A. Constantinescu, J. Brands, J. A. Spaan, and H. Vink. Bradykinin- and sodium nitroprusside-induced increases in capillary tube haematocrit in mouse cremaster muscle are associated with impaired glycocalyx barrier properties. *J. Physiol. (Lond.)*, 586:3207–3218, Jul 2008.

H. Vink and B. R. Duling. Identification of distinct luminal domains for macromolecules, erythrocytes, and leukocytes within mammalian capillaries. *Circ. Res.*, 79:581–589, Sep 1996.

W. Wang. Change in properties of the glycocalyx affects the shear rate and stress distribution on endothelial cells. *J Biomech Eng*, 129:324–329, Jun 2007.

S. Weinbaum. 1997 Whitaker Distinguished Lecture: Models to solve mysteries in biomechanics at the cellular level; a new view of fiber matrix layers. *Ann Biomed Eng*, 26:627–643, 1998.

S. Weinbaum, R. Tsay, and F. E. Curry. A three-dimensional junction-pore-matrix model for capillary permeability. *Microvasc. Res.*, 44:85–111, Jul 1992.

S. Weinbaum, X. Zhang, Y. Han, H. Vink, and S. C. Cowin. Mechanotransduction and flow across the endothelial glycocalyx. *Proc. Natl. Acad. Sci. U.S.A.*, 100: 7988–7995, Jun 2003.

S. Weinbaum, J. M. Tarbell, and E. R. Damiano. The structure and function of the endothelial glycocalyx layer. *Annu Rev Biomed Eng*, 9:121–167, 2007.

Y. Yao, A. Rabodzey, and C. F. Dewey. Glycocalyx modulates the motility and proliferative response of vascular endothelium to fluid shear stress. *Am. J. Physiol. Heart Circ. Physiol.*, 293:H1023–1030, Aug 2007.

Y. Zeng and S. Weinbaum. Stokes flow through periodic orifices in a channel. *J. Fluid Mech.*, 263:207–226, 1994.

X. Zhang, R. H. Adamson, F. R. Curry, and S. Weinbaum. A 1-D model to explore the effects of tissue loading and tissue concentration gradients in the revised Starling principle. *Am. J. Physiol. Heart Circ. Physiol.*, 291:H2950–2964, Dec 2006a.

X. Zhang, F. R. Curry, and S. Weinbaum. Mechanism of osmotic flow in a periodic fiber array. *Am. J. Physiol. Heart Circ. Physiol.*, 290:H844–852, Feb 2006b.

X. Zhang, R. H. Adamson, F. E. Curry, and S. Weinbaum. Transient regulation of transport by pericytes in venular microvessels via trapped microdomains. *Proc. Natl. Acad. Sci. U.S.A.*, 105:1374–1379, Jan 2008.